Laser in der Materialbearbeitung
Forschungsberichte des IFSW

M. Vogel
Specialty Fibers for High Brightness
Laser Beam Delivery

Laser in der Materialbearbeitung
Forschungsberichte des IFSW

Herausgegeben von
Prof. Dr. phil. nat. habil. Thomas Graf, Universität Stuttgart
Institut für Strahlwerkzeuge (IFSW)

Das Strahlwerkzeug Laser gewinnt zunehmende Bedeutung für die industrielle Fertigung. Einhergehend mit seiner Akzeptanz und Verbreitung wachsen die Anforderungen bezüglich Effizienz und Qualität an die Geräte selbst wie auch an die Bearbeitungsprozesse. Gleichzeitig werden immer neue Anwendungsfelder erschlossen. In diesem Zusammenhang auftretende wissenschaftliche und technische Problemstellungen können nur in partnerschaftlicher Zusammenarbeit zwischen Industrie und Forschungsinstituten bewältigt werden.

Das 1986 gegründete Institut für Strahlwerkzeuge der Universität Stuttgart (IFSW) beschäftigt sich unter verschiedenen Aspekten und in vielfältiger Form mit dem Laser als einem Werkzeug. Wesentliche Schwerpunkte bilden die Weiterentwicklung von Strahlquellen, optischen Elementen zur Strahlführung und Strahlformung, Komponenten zur Prozessdurchführung und die Optimierung der Bearbeitungsverfahren. Die Arbeiten umfassen den Bereich von physikalischen Grundlagen über anwendungsorientierte Aufgabenstellungen bis hin zu praxisnaher Auftragsforschung.

Die Buchreihe „Laser in der Materialbearbeitung – Forschungsberichte des IFSW“ soll einen in der Industrie wie in Forschungsinstituten tätigen Interessentenkreis über abgeschlossene Forschungsarbeiten, Themenschwerpunkte und Dissertationen informieren. Studenten soll die Möglichkeit der Wissensvertiefung gegeben werden.

Speciality Fibers for High Brightness Laser Beam Delivery

von Dr.-Ing. Moritz Vogel
Universität Stuttgart

Herbert Utz Verlag · Wissenschaft
München

Als Dissertation genehmigt
von der Fakultät für Konstruktions-, Produktions- und Fahrzeugtechnik
der Universität Stuttgart

Hauptberichter: Prof. Dr. phil. nat. habil. Thomas Graf
Mitberichter: Prof. Dr. rer. nat. Alois Herkommer

Bibliografische Information der Deutschen Nationalbibliothek
Die Deutsche Nationalbibliothek verzeichnet diese Publikation
in der Deutschen Nationalbibliografie; detaillierte bibliografische
Daten sind im Internet über http://dnb.ddb.de abrufbar.

Zugleich: Dissertation, Stuttgart, Univ., 2014

D 93

ISBN 978-3-8316-4382-0

Printed in Germany

Herbert Utz Verlag GmbH, München
Tel.: 089-277791-00 · www.utzverlag.de

Contents

List of Figures

List of Tables

List of Symbols

Symbol	Description	Unit/Value
$\vec{H}$	magnetic field	A/m
$\vec{E}$	electric field	V/m
$\vec{B}$	magnetic flux density	$\mathrm{Vs/m^2}$=T
$\vec{D}$	electric flux density	$\mathrm{As/m^2}$
$\vec{J}$	electric current density	$\mathrm{A/m^2}$
ρ	electric charge density	$\mathrm{As/m^3}$
$\vec{P}$	electric polarization density	$\mathrm{As/m^2}$
$\vec{M}$	magnetization	A/m
I	optical intensity	$\mathrm{W/m^2}$
P	optical power	W
ϵ_0	vacuum permittivity	$8.854187817...\times10^{-12}$ As/(Vm)
μ_0	vacuum permeability	$1.2566370614...\times10^{-6}$ Vs/(Am)
c	speed of light	299792458 m/s
λ	wavelength	m
k	(angular) wavenumber	1/m
$\vec{k}$	wave vector	1/m
ω	angular frequency	rad/s
ν	frequency	1/s
t	time	s
L	propagation length	m
L_b	beat length	m
n	refractive index	dimensionless

ϕ	phase	dimensionless
ξ	nonlinear coefficient	dimensionless
NA	numerical aperture	dimensionless
Δ_n	normalized refractive index difference	dimensionless
P_{in}	incident power	W
P_{out}	transmitted power	W
α	fiber attenuation	dB/km
α_{diff}	differential losses / loss ratio	dimensionless
A_{eff}	effective mode area	m^2
L_{eff}	effective length	m
P_B	stimulated Brillouin threshold	W
ν_B	Brillouin frequency shift	1/s
$g_B(\nu)$	Brillouin gain	$\text{W}^{-1}\text{m}^{-1}$
P_R	stimulated Raman threshold	W
ν_R	Raman frequency shift	1/s
$g_R(\nu)$	Raman gain	$\text{W}^{-1}\text{m}^{-1}$
ω	beam waist	m
θ	divergence angle (half-angle)	rad
M^2	beam propagation factor	dimensionless
R	bending radius	m
r_{co}	fiber core radius	m
r_{cl}	fiber cladding radius	m
l	(fiber) length	m
a	thickness of high index layer	m
b	thickness of low index layer	m
Λ	pitch	m
d	hole size	m
w_b	bridge width	m
l_b	bridge length	m

Kurzfassung in deutscher Sprache

Der Erfolg von Festkörperlasersystemen basiert in hohem Maße auf der Tatsache, dass deren Strahlung bei einer Wellenlänge im Bereich um 1 µm kostengünstig, effizient und vor allem hoch flexibel mit optischen Glasfasern transportiert werden kann. Diese lassen sich in Robotersysteme integrieren und die Laserstrahlung gelangt ohne störende Fokusverschiebungen, wie sie in Freistrahl-Strahlführungssystemen auftreten, zum Werkstück.

Die rasche Zunahme der Strahlqualität und der Ausgangsleistung von Scheiben- und Faserlasersystemen sind die treibenden Kräfte bei der Entwicklung von neuen optischen Fasern. Die Leistungsskalierbarkeit von passiven faserbasierten Strahlführungssystemen sowie von aktiven Fasern wird durch das Einsetzen von mehreren nichtlinearen Effekte innerhalb des Wellenleitermaterials, hauptsächlich der stimulierten Brillouin-Streuung und der stimulierten Raman-Streuung, begrenzt. Die Leistungsschwelle für diese Effekte nimmt mit zunehmender Faserlänge ab, so dass selbst die in aktiven Fasern erzeugte Laserstrahlung nicht über beliebige Strecken mit passiven Fasern transportiert werden.

Daher wurden im Rahmen dieser Arbeit unterschiedliche Spezialfaserkonzepte mit dem Ziel untersucht die effektive Modenfeldfläche zu maximieren ohne dabei die Strahlqualität zu mindern. Dafür wurden Finite-Elemente-Rechnungen zur Simulation und Optimierung der Faserstrukturen verwendet. Mit Hilfe von Eigenwertberechnungen wurde die Modenstruktur der Fasern simuliert und unter Verwendung von sogenannten „Perfectly-Matched Layers“ sowie komplexwertiger Berechnung konnten die Verluste dieser Eigenmoden bestimmt werden. Mit Hilfe der Methode des „Äquivalenten Brechungsindexes“ wurde der Einfluss von Biegungen der Faser auf die Moden simuliert. Darüber hinaus wurde die Herstellung der Spezialfasern unterstützt und eigens produzierte sowie zugekaufte Fasern wurden experimentell untersucht. Zur Charakterisierung der Fasern wurden Messplätze aufgebaut. Hierbei stand die

Untersuchung der Dämpfung, der Strahlqualität und der Biegeempfindlichkeit der Fasern im Vordergrund. Zur Verbesserung der experimentellen Abläufe und zur Erhöhung der Reproduzierbarkeit wurde die Justage der Freistrahl-zu-Faserkopplung mit Hilfe von computergesteuerten, hochpräzisen Achsen automatisiert.

Ein Ansatz um die Modenfeldfläche A_{eff} zu erhöhen besteht darin, mehrere kohärent gekoppelte Kerne in einem gemeinsamen Mantel anzuordnen um dadurch die Leistung zu verteilen und die Belastbarkeit der Faser zu erhöhen. Dieser Ansatz ist als Mehrkernfaser (Multicore Fiber MCF) bekannt. Im Rahmen dieser Arbeit wurde erstmals eine einmodige MCF demonstriert. Die Faser besteht aus 19 Germanium dotierten Kernen, welche in einem Mantel aus Quarzglas eingebettet sind. Die Kopplung der Kerne resultiert in einem Modenfeld von $A_{\text{eff}} = 465\,\mu\text{m}^2$ bei einer Wellenlänge von 1 µm. Die Fasermode besitzt eine nahezu gaußförmige Feldverteilung und kann wie eine (einmodige) Standard-Stufenindexfaser eingesetzt und mit Stufenindexfasern verspleißt werden. Die Biegeempfindlichkeit der 19-Kernfaser ist jedoch grenzwertig, so dass die Faser vorsichtig gehandhabt werden muss um scharfe Biegungen zu vermeiden. Durch das Spleißen dieser Faser an einen Faserlaser sowie das Vermeiden von Biegeradien kleiner als 0,2 m konnte erfolgreich ein Hochleistungstest mit 356 W (begrenzt durch die verfügbare Grundmode-Laserleistung) durchgeführt werden.

Eine Möglichkeit große Modenfelder bei verhältnismäßig niedriger Biegeempfindlichkeit zu realisieren sind Fasern welche eine photonische Bandlücke verwenden, um die Laserstrahlung zu führen. Diese Arbeit konzentriert sich dabei auf sogenannte Bragg-Fasern (BF). Diese bestehen aus einem (großen) Kern welcher von konzentrischen Ringen mit alternierend hoher und niedriger Brechzahl umgeben ist, ähnlich einem dielektrischen Spiegel. Diese Vielschichtstrukturen wurden mit einem innerhalb dieser Arbeit entwickeltem Verfahren optimiert. Darauf basierend wurden Bragg-Fasern beschafft und experimentell untersucht. Die optimierten BF sind nahezu frei von Biegeverlusten und zeigen im Vergleich mit Stufenindexfasern eine deutlich geringere Biege-induzierte Verformung des Modenfeldes.

Eine weitere Art von Spezialfaser nutzt ein Verlustmanagement um eine hohe Strahlqualität bei großem Kerndurchmesser und dementsprechend hohen Modenfeldflächen zu erreichen. Diese „Leakage Channel“ Fasern (LCF) bestehen aus einem Faserkern, welcher von einzelnen niedrigbrechenden Elementen, zum Beispiel Luftlöchern, umgeben ist. Zwischen diesen Löchern kann das Licht jedoch entweichen.

Unter Berücksichtigung der Abhängigkeit der Kopplung zweier Moden von Real - und Imaginärteilen der effektiven Brechungsindizes dieser Moden kann eine Modenkopplung über das Verlustmanagement minimiert werden.
Zunächst wurde eine einfache LCF mit 5 Löchern untersucht. Die Messungen ergaben eine effektive Modenfeldfläche von $A_{\text{eff}} = 383\,\mu\text{m}^2$ und eine Beugungsmaßzahl von $M_x^2 = M_y^2 = 1,1$ nach der Faser. Daraufhin wurde der Einfluss von zusätzlichen mikrostrukturierten Schichten, also weiteren Schichten mit Löchern, untersucht. Wie sich herausstellte ist eine Erhöhung der Anzahl der Schichten nicht ausreichend, um die Biegeverluste wesentlich zu reduzieren. Jedoch können die Verlustunterschiede zwischen der Grundmode und den Moden höherer Ordnung dadurch vergrößert werden. Eine Optimierung im Hinblick auf die Biegeempfindlichkeit konnte durch die Änderung der Lochdurchmesser von kleineren Löchern in der inneren mikrostrukturierten Schicht zu größeren Löchern in einer zweiten Schicht erreicht werden.
Zusätzlich wurde die Verwendung von Resonanzen mit Mantelmoden der LCF betrachtet. Durch eine sorgfältige Anpassung des Faserdurchmessers können im Kern geführte Moden höherer Ordnung durch Angleichung der effektiven Brechungsindizes resonant mit Mantelmoden gekoppelt werden. Dies führt zu einer Erhöhung der Verluste dieser Moden und kann somit zu einer Verbesserung des Verlustmanagements genutzt werden.
Das optimierte LCF Design besitzt eine Grundmode mit einem Modenfeldfläche von $708\,\mu\text{m}^2$ und kann wie eine Standard Einmodenfaser verwendet werden um beugungsbegrenzte Hochleistungslaserstrahlung flexibel zu transportieren und dies bei einer gemessenen Dämpfung der Grundmode von weniger als 6 dB/km. Noch größere Modenflächen können erreicht werden, wenn mehr als eine Mode effektiv geführt werden darf. Für den Einsatz mit aktuellen Hochleistungsfaserlasern, welche neben der Fundamentalmode oft einen kleinen Leistungsanteil in der LP_{11} Mode zeigen, wurde daher eine spezielle LCF entwickelt. Diese führt beide Moden effizient, die Modenfeldfläche der Fundamentalmode beträgt in diesem Fall $A_{\text{eff}} = 1187^{\,2}$.
Neben den umfassenden Studien (asymptotisch) einmodiger Fasern wurde auch der Transport von Grundmodelaserstrahlung in vielmodigen Fasern analysiert. Basierend auf der Annahme, dass eine hohe Differenz der effektiven Brechungsindizes Δn_{eff} (z.B. $\geq 10^{-4}$) eine Modenkopplung verhindert, wurden mehrere Stufenindexfasern und eine Multikernfaser mit 7 Kernen charakterisiert. Eine Stufenindexfaser mit $30\,\mu\text{m}$ Kerndurchmesser und einer numerischen Apertur (NA) von 0,06 wurde be-

sonders intensiv untersucht. Ein mit geeigneten Optiken sorgfältig in diese Faser eingekoppelter Gaußstrahl konnte unter Beibehaltung einer hohen Strahlqualität in der Faser transportiert werden. Eine Beugungsmaßzahl von $M^2 = 1,12$ wurde nach der Faser (mit 10 m Länge) gemessen. Die Beugungsmaßzahl verschlechterte sich selbst bei starker Biegung oder Bewegung der Faser nicht merklich. Rückschneide-Messungen zeigten, dass sich die Beugungsmaßzahl auch nicht mit der Faserlänge ändert. Die NA der Faser ist mit 0,06 noch hoch genug, um Biegeverluste bei Biegungen mit $R > 0,1$ m zu unterdrücken. Die Aufgrund der Biegung hervorgerufene Verringerung und Verformung des Modenfelds wurde jedoch mit Hilfe eines speziell dafür ausgelegten Experiments gemessen und mit Simulationsergebnissen verglichen. Ein Hochleistungstest einer ähnlichen Faser resultierte in einer Beugungsmaßzahl von $M^2 = 1,35$ nach einer 100 m langen Faser bei einer Leistung von 800 W.

Im Vergleich mit einer Multikernfaser hat sich in Bezug auf Vielmodenfasern kein Vorteil des Multikernkonzepts gezeigt. Bei einmodigen Fasern können mit Hilfe des Multikernkonzeptes jedoch geringere effektive NAs reproduzierbar hergestellt und daher größere Modenfelder erzeugt werden als mit Standard-Stufenindexfasern. Bragg-Fasern sind insbesondere bei Anwendungen, bei denen eine sehr hohe Robustheit gegenüber scharfen Biegungen gefordert wird, z.B. bei chirurgischen Eingriffen in der Medizin, von Vorteil. Wie sich zeigte, können qualitativ hochwertige Vielmodenfasern in gewissen Grenzen auch zum Transport von Grundmodelaserstrahlung verwendet werden. Weiteres Potential besteht insbesondere bei den „Leakage Channel“ Fasern. Sowohl bei aktiven als auch passiven Fasern können durch dieses Konzept größere Modenfeldflächen erreicht werden.

Extended Abstract

The tremendous impact of solid-state lasers on material processing and the rapid increase of the beam quality as well as the output power are driving forces in the development of new optical fibers and high-power suitable beam delivery systems. The power scalability of such systems over significant distances is limited by the onset of several nonlinear effects inside the waveguide material, mainly stimulated Brillouin scattering and stimulated Raman scattering.

Within this work, finite element calculations are used to simulate and optimize different fiber structures. Moreover, the production of some of the optimized fibers is considered and experiments to measure their attenuation, mode-structure and bending losses are introduced.

One approach to increase the mode field area and therefore the power handling capabilities is to assemble several coherently coupled cores in a common cladding to distribute the power and to increase the power handling capabilities. This approach is known as multicore fiber (MCF). A single-mode MCF consisting of 19 coupled cores with a large mode field area of $A_{\mathrm{eff}} = 465\,\mu\mathrm{m}^2$ was investigated. The fiber has a close to Gaussian field distribution and can be used as, and be spliced to, a (single mode) step index fiber. The bending sensitivity of the 19-core fiber is close to a manageable limit so that the fiber has to be handled carefully to avoid sharp bends. However, by avoiding bending radii smaller than 0.2 m and splicing the fiber to a fiber laser, a high-power test with 356 W (limited by the available laser source) was demonstrated.

Bragg-type photonic bandgap fibers offer the possibilities to reduce the bending sensitivity of large mode area fibers. Therefore, Bragg fibers (BF) were investigated as well and a method of optimizing their multilayer cladding was developed. Based on an optimized structure several fibers were produced and characterized in the laboratory. The optimized BFs were virtually free of bending losses and they showed

a much lower bend-induced mode field deformation when compared to step index fibers.

Another type of fiber which uses loss management to achieve and maintain a high beam quality, the leakage channel fiber (LCF), was also examined. At first, a simple LCF with 5 holes was investigated. The measurements revealed an effective mode area of $A_{\text{eff}} = 383\,\mu\text{m}^2$ and a beam propagation factor of $M_x^2 = M_y^2 = 1.1$. Then the influence of additional microstructured layers was examined. It was found that if the design is limited by high bending losses, increasing the number of layers is not sufficient to substantially reduce these losses but the differential losses between the fundamental mode and higher-order modes can be increased. Furthermore, the bending sensitivity could be reduced by changing the hole sizes from smaller holes in the inner microstructured layer to larger holes in a second layer to further optimize the fiber.

Additionally, the use of cladding resonances in LCFs is considered. By carefully designing the fiber diameter, core-guided higher-order modes can be resonantly coupled to cladding modes substantially improving the differential losses. The final design with a fundamental mode area of $708\,\mu\text{m}^2$ can be used as a standard single-mode fiber, efficiently guiding diffraction-limited high-power beams.

Larger mode field areas can be achieved if more modes are allowed to propagate with low losses. A LCF for the use with present high-power fiber lasers and amplifiers which usually show a minor LP_{11} mode content was designed. The fiber guides LP_{01} and LP_{11} modes and exhibits a fundamental mode area of $A_{\text{eff}} = 1187\,\mu\text{m}^2$.

Besides the comprehensive studies of (asymptotically) SM fibers, the possibility to transport a fundamental mode beam in multimode fibers was also investigated. Based on the assumption that a large difference of the effective refractive index Δn_{eff} (e.g., $\geq 10^{-4}$) prevents mode coupling, several step index fibers and a 7-core multicore fiber were tested. In particular, a fiber with a core diameter of $30\,\mu\text{m}$ and an NA of 0.06 was intensively studied. When a Gaussian beam is carefully injected into this fiber using suitable coupling optics, a high beam quality can be maintained within the fiber. A beam propagation factor of $M^2 \approx 1.12$ was measured after 10 m of fiber even when the fiber was strongly bent or moved. Cutback measurements showed that the beam propagation factor does not change noticeably with the fiber length. The NA of the fiber is high enough to prevent bending losses for bends with $R > 0.1\,\text{m}$. The bend-induced mode field reduction and deformation was measured

using a special experimental setup and compared to simulation results. A high power test resulted in a M^2 of 1.35 after a 100 m long fiber measured at a output power of 800 W.

Finally, in accordance with the fundamental mode transport in multimode fibers requirements for the transport of radially and azimuthally polarized modes are proposed. Based on this conditions three different fiber concepts for maintaining radially and azimuthally polarized modes are suggested. The results of simulations demonstrate the potential of these fibers for the delivery of such special modes. Parametric studies are used to maximize the mode field areas of the different fiber concepts. As a result, specialty fibers with higher mode field areas as published so far are proposed. For instance, a fiber with a ring-shaped core around a central air hole maintaining the TE_{01} mode with a mode field area of 280 µm^2 at 1 µm wavelength.

Chapter 1

Introduction

1.1 Motivation

In 1960 when T. H. Maiman demonstrated the first laser [1] no one could have foreseen the versatile fields of applications lasers cover today. Maiman himself claimed: "A laser is a solution seeking a problem.", (e.g., interview with New York Times 1964 [2]). However, soon after he realized the first laser in the visible wavelength range scientists intensified the work on a new concept of communication system termed "optical communication" which could transport a tremendous amount of information. But atmospheric influences would render free space optical communication useless and a suitable beam guiding system was missing. Evacuated straight or highly reflecting tubes would be bulky and expensive and losses of optical waveguides at that time such as multimode fiber bundles were much too high.
In 1966 K. C. Kao and G. A. Hockham suggested the use of glass fibers with a small core and only a very small refractive index difference between core and cladding (of about 1%). Such a fiber works as a single-mode waveguide without the problem of multimode dispersion [3]. Furthermore, they compared the absorption, scattering and other losses of different materials including crystals, inorganic glasses, and organic polymers. They identified glasses as the most promising materials, estimated a Rayleigh scattering loss on the order of a few decibels per kilometer at 1 µm wavelength, and stated that with the reduction of impurities the absorption can be further decreased. The first measurements were performed with fiber bundles and showed losses of several thousand dB/km. In the late 60s commercially available rods and tubes were used to draw multimode fibers with a transmission

loss of 140 dB/m and even 40 dB/m from preforms produced from a double layered melt at the University of Southampton (GB) [4].

In 1970 Kapron *et al.* reported on a single-mode fiber with a transmission loss of 20 dB/km produced at Corning Glass Works (USA) [5]. Kapron and his co-workers added a suitable oxide dopant to adjust the refractive index of the glass. Instead of using different glasses with similar melting temperatures to form core and cladding of the fiber, both were based on silica. This work triggered further research in laboratories worldwide. At that time the water content of the preform glass was the main cause for transmission losses in optical fibers especially in the infrared. Later the researchers at the Bell Telephone Laboratories developed the "modified chemical vapor deposition" (MCVD) process which reduced the water content in the glass and therefore significantly reduced the losses [6]. With further variations of this technique and the development of suitable polymer coatings to prevent fiber fractures and to protect the fiber from water and dust, a robust, flexible, and low loss beam guiding system was achieved. The development of such fibers together with the invention of the erbium amplifier in 1987 [7] led to the breakthrough of optical communications which has revolutionized the way of communication.

At the same time various laser systems at different wavelength were developed, out of which only a few made their way to industrial applications. The first high-power laser system was the CO_2 gas laser [8] which has been the dominating tool in the field of high-power material processing for many decades and is still widely-used for cutting and welding applications.

With the appearance of diode lasers as highly efficient pump sources for solid-state lasers, the latter became more powerful and their running costs were reduced. Together with new laser designs for improved heat management such as thin-disc [9] and fiber [10] lasers, the output power as well as the beam quality of solid-state lasers has increased tremendously over the past years [11, 12].

However, the successful commercialization of high-power solid-state lasers is partly attributed to the fact that they usually operate at a wavelength of about 1 µm which enables efficient and flexible beam transport with silica optical fibers. The beam transport of CO_2-lasers at about 10 µm instead is realized by the free space beam and "flying optics" which is much more expensive and has the drawback of focal shifts at the workpiece.

On the other hand, the tremendous impact of solid-state lasers on material pro-

cessing and the rapid increase of beam quality and output power are driving forces in the development of high-power capable beam delivery systems. But the power scalability of such systems over significant distances is limited by the onset of several nonlinear effects inside the waveguide material [13], mainly stimulated Brillouin scattering and stimulated Raman scattering. Since the threshold of most nonlinear effects is proportional to the intensity, increasing the effective mode area is the key to increase the power handling capabilities. Starting from a standard single-mode fiber used for optical communication systems with an effective mode area of about $30\,\mu m^2$, the core size must be increased significantly to meet this goal.
To keep the waveguide single-mode, the numerical aperture (NA) of the fiber has to be decreased at the same time. Besides the difficulties of producing low NA fibers, a very low NA results in an excessive bending sensitivity which does not allow the use of such fibers for flexible beam delivery applications with reasonable bending radii. Similar problems are faced by the task of a further power scaling of fiber lasers and amplifiers. In order to overcome these problems, several specialty fiber concepts are investigated with the help of simulations and experiments within this work.
Besides the power and the beam quality of laser sources, other properties of laser beams have recently attracted a lot of attention due to applications in material processing. For example, special field distributions and polarization states such as radially and azimuthally polarized ring-shaped modes may improve the quality and the speed of sheet metal cutting or drilling [14, 15]. Therefore, the conditions for fiber-based beam delivery of such modes are also studied within this work.
The topics and structure of this work are explained in the following paragraph.

1.2 Structure of this Work

The fundamentals of fiber optics are briefly reviewed in chapter 2. First, step index fibers are introduced and analyzed by means of geometrical optics. Then, wave optics is used to obtain the wave equation and the mode structure of optical fibers. The discussion includes the most important nonlinear effects such as stimulated Raman and Brillouin scattering. General fiber properties such as attenuation and bending losses are described as well as the conditions for mode mixing. The quality of the transmitted laser beam which is related to the mode mixing is also discussed. Chapter 2 concludes with an overview of different types of specialty fiber concepts,

for instance, multicore fibers, photonic bandgap fibers, and leakage channel fibers. Chapter 3 focuses on the methods used for the simulation of these fibers. Finite element calculations with COMSOL Multiphysics are discussed and it is shown how the eigenmodes of straight and bent fibers are calculated and how losses are computed by means of perfectly matched layers.
Chapter 4 begins with a description of the fiber handling and then explains all experiments used for the characterizations of the fibers. Especially, the procedures for obtaining the overall fiber attenuation and for examining the influence of fiber bends on light traveling inside the fiber are described as well as measuring the beam propagation factor to estimate the beam quality.
The results of the theoretical and experimental investigations are compared and discussed simultaneously because the simulations and experiments have been carried out in parallel and inspired each other. Chapter 5 is subdivided according to the different kinds of specialty fibers described in chapter 2. Furthermore, the use of large core multimode fibers for the transport of fundamental mode beams is investigated in chapter 6 and the results of a high-power test with more than 800 W are shown. An outlook concerning the beam delivery of radially and azimuthally polarized beams is given in chapter 7 and some preliminary considerations, experiments, and simulations are presented. Finally, the most important results are summarized in chapter 8.

Chapter 2

Fundamentals of Fiber Optics

This chapter gives a short summary of the basic physics of optical waveguides. First, geometrical optics is applied to step index fibers. Then, wave optics is used to derive the governing equations for the calculation of the eigenmodes of the fibers. Limitations of the power handling capabilities of optical fibers due to nonlinear effects are also described. Different loss mechanisms reducing the power during beam delivery are considered and specialty fiber concepts are introduced. Finally, the production of optical fibers in general and, in particular, at the production facility of the IFSW is briefly described.

2.1 Geometrical Optics Applied to Step Index Optical Fibers

A step index fiber (SIF) guides light due to the mechanism of total internal reflection (TIR). As described in the following, light is confined within the fiber core because the refractive index n_{co} of the fiber core is higher than the refractive index n_{cl} of the cladding surrounding the core. Usually a protective layer (e.g., a polymer coating) is used to give mechanical support to the fiber which is not important for this optical considerations. The fiber can be considered as surrounded by air with the refractive index n_{air}. The refractive indices follow the relation

$$n_{co} > n_{cl} > n_{air} \ . \tag{2.1}$$

Here, Snell´s law and trigonometry are used to derive the maximum angle at which incident light is guided by the fiber. The angles α and β describe the refraction at the

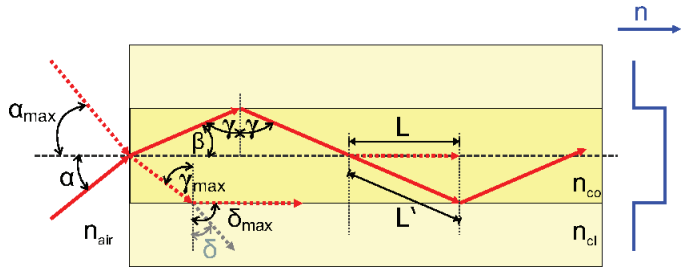

Figure 2.1: Schematic description of rays in a step index fiber. In the picture of geometrical optics different rays propagate with different bouncing angles within the fiber core with higher refractive index n_{co}.

fiber end face which is perpendicular to the fiber axis. The angles γ and δ describe the refraction at the core-cladding interface. Considering the rays shown in figure 2.1 leads to $\beta + \gamma = \pi/2$ and $\sin\beta = \cos\gamma$ and accordingly $\sin\beta = \sqrt{1-\sin^2\gamma}$. Using Snell´s law one obtains

$$n_{air}\sin\alpha = n_{co}\sin\beta\,, \tag{2.2}$$

$$n_{co}\sin\gamma = n_{cl}\sin\delta\,. \tag{2.3}$$

The critical angle of total reflection is defined by $\sin\delta_{max} = 1$ which makes $\sin\gamma_{max} = n_{cl}/n_{co}$. Bringing these considerations together leads to

$$n_{air}\sin\alpha_{max} = n_{co}\sqrt{1-\frac{n_{cl}^2}{n_{co}^2}} = \sqrt{n_{co}^2 - n_{cl}^2}\,. \tag{2.4}$$

With $n_{air} = 1$, the critical angle α_{max}, specifying the highest angle at which incident light is guided by TIR within the fiber core, is given by

$$\alpha_{max} = \arcsin\sqrt{n_{co}^2 - n_{cl}^2} = \arcsin \mathrm{NA} \tag{2.5}$$

which defines the *numerical aperture* NA

$$\mathrm{NA} = \sqrt{\mathrm{n_{co}^2 - n_{cl}^2}}\,. \tag{2.6}$$

The NA is a dimensionless quantity describing the divergence of a light cone which can be accepted by the fiber core. The maximum acceptance angle at the fiber

entrance is defined by $\sin\alpha_{max} = \mathrm{NA}$ and $\sin\beta_{max} = \mathrm{NA}/\mathrm{n_{co}}$ inside the fiber. Since linear optics is time invariant, the maximum angle at which light leaves the fiber is the same as the acceptance angle. Another useful dimensionless quantity is the *normalized refractive index difference* Δ_n [16]

$$\Delta_n = \frac{n_{co}^2 - n_{cl}^2}{2n_{co}^2} , \tag{2.7}$$

which can be used to rewrite the NA as

$$\mathrm{NA} = \mathrm{n_{co}}\sqrt{2\Delta_\mathrm{n}} . \tag{2.8}$$

The ray optics picture gives a basic explanation of how the light is guided inside a fiber. It can also be used for a basic understanding of (*modal*) *dispersion*. A light ray traveling parallel to the axis of the fiber will have a shorter path L and therefore be faster than a light ray with a certain angle to the axis, bouncing back and forth at the interface between core and cladding, with the path length L'.
From figure 2.1 it can be seen that the relation between L and L' is simply $L' = L/\cos\beta$. Since $\beta << 1\mathrm{rad}$ one can use the approximations $\sin\beta \approx \beta$ and $\cos\beta \approx 1 - \beta^2/2$. Together with the previous result $\sin\beta_{max} = \mathrm{NA}/\mathrm{n_{co}}$ for the ray with the highest possible angle β it follows that

$$L = L'\left(1 - \frac{\beta^2}{2}\right) = L'\left(1 - \frac{NA^2}{2n_{co}^2}\right) = L'(1 - \Delta_n) . \tag{2.9}$$

The delay time between these light rays is therefore

$$t_{max} - t_{min} = \frac{n_{co}L'}{c} - \frac{n_{co}L}{c} = \frac{n_{co}L'}{c}(1 - (1 - \Delta_n)) = t_{max}\Delta_n \tag{2.10}$$

which is proportional to Δ_n. However, the ray optical description has its limitations. In reality, the light is not reflected sharply at the interface of core and cladding. It penetrates the cladding to a distance governed by the wavelength and the NA. Not only is there a maximum angle for light bouncing inside the fiber, but also only some discrete intensity patterns are possible. This can all be described adequately by taking into account the wave properties of light.

2.2 Wave Optics

In this section the wave equation is derived from Maxwell's equations and the solutions, called modes, are briefly described [16].

2.2.1 Wave Equation

With the magnetic field $\vec{H}$, the electric field $\vec{E}$, the magnetic flux density $\vec{B}$, and the electric flux density $\vec{D}$ as well as the free charge density ρ and the free current density $\vec{J}$ the Maxwell's equations in SI units can be written as

$$\nabla \cdot \vec{D} = \rho \tag{2.11}$$

$$\nabla \cdot \vec{B} = 0 \tag{2.12}$$

$$\nabla \times \vec{H} = \vec{J} + \frac{\partial \vec{D}}{\partial t} \tag{2.13}$$

$$\nabla \times \vec{E} = -\frac{\partial \vec{B}}{\partial t} \,. \tag{2.14}$$

The response of bound charges and currents to applied electric or magnetic fields can be expressed by the electric polarization density $\vec{P}$ and the magnetization $\vec{M}$ as

$$\vec{D} = \epsilon_0 \vec{E} + \vec{P} \tag{2.15}$$

$$\vec{B} = \mu_0 (\vec{H} + \vec{M}) \tag{2.16}$$

$$\vec{J} = \sigma \vec{E} \,. \tag{2.17}$$

These definitions are called constitutive relations because they describe the relations between $\vec{E}$ and $\vec{D}$ as well as $\vec{H}$ and $\vec{B}$. With the constitutive relations and the Maxwell's equations light propagation in matter can be described. Dielectric media such as air or glass satisfy:

- $\rho = 0$: there are no free charges
- $\vec{J} = 0$: there are no currents
- $\vec{M} = 0$: there is no magnetization .

With this simplifications, the Maxwell's equations in dielectric materials can be written as

$$\nabla \cdot \vec{D} = 0 \tag{2.18}$$

$$\nabla \cdot \vec{B} = 0 \tag{2.19}$$

$$\nabla \times \vec{B} = \mu_0 \frac{\partial \vec{D}}{\partial t} \tag{2.20}$$

$$\nabla \times \vec{E} = -\mu_0 \frac{\partial \vec{H}}{\partial t} \,. \tag{2.21}$$

By applying $\nabla\times$ to 2.21 and using the identity $\nabla \times \nabla \times \vec{E} = \nabla(\nabla \cdot \vec{E}) - \nabla^2 \vec{E}$ as well as 2.13 and $\vec{J} = 0$ the wave equation

$$\nabla(\nabla \cdot \vec{E}) - \nabla^2 \vec{E} = -\mu_0 \frac{\partial^2 \vec{D}}{\partial t^2} \tag{2.22}$$

for the electric field is obtained. The equation for the magnetic field can be found in an analogous way.

At this point only isotropic media such as glass without birefringence are considered. Therefore, $\vec{E} \,||\, \vec{P}$ and $\vec{D} \,||\, \vec{E}$ as in the case of propagation in free space. As a consequence, 2.18 implies $\nabla \cdot \vec{D} = \nabla \cdot \vec{E} = 0$ which reduces the wave equation 2.22 to

$$\nabla^2 \vec{E} = \mu_0 \frac{\partial^2 \vec{D}}{\partial t^2} \,. \tag{2.23}$$

With the relation 2.15 this expression can be written as

$$\nabla^2 \vec{E} = \mu_0 \epsilon_0 \frac{\partial^2 \vec{E}}{\partial t^2} + \mu_0 \frac{\partial^2 \vec{P}}{\partial t^2} \,. \tag{2.24}$$

In order to solve the wave equation it is necessary to make assumptions about the relation between the polarization density $\vec{P}$ and the electric field $\vec{E}$. Assuming that a change of the electric field changes the polarization density instantaneously, one can expand the polarization density into a series [16]

$$\vec{P} = \epsilon_0 \left(\chi^{(1)} \vec{E} + \chi^{(2)} \vec{E}^2 + \chi^{(3)} \vec{E}^3 + ... \right) \,. \tag{2.25}$$

Because isotropic media are considered $\vec{P}$ and $\vec{E}$ are parallel which requires the even terms in the expansion to be zero because the tensors $\chi^{(i)}$ with $i = 2, 4, 6, ..$ may not have the same direction as $\vec{E}$. A linear approximation can be made for low intensities and the series 2.25 is reduced to the first term

$$\vec{P} = \epsilon_0 \chi^{(1)} \vec{E} \,. \tag{2.26}$$

Inserting the linear approximation 2.26 in the wave equation 2.24 leads to a linear 2nd order partial differential equation

$$\nabla^2\vec{E} = \mu_0\epsilon_0\frac{\partial^2}{\partial t^2}\vec{E} + \mu_0\frac{\partial^2}{\partial t^2}\epsilon_0\chi^{(1)}\vec{E} \tag{2.27}$$

$$= \mu_0\epsilon_0(1+\chi^{(1)})\frac{\partial^2}{\partial t^2}\vec{E}\,. \tag{2.28}$$

With $\mu_0\epsilon_0 = 1/c^2$ and the relative permittivity $\epsilon = 1+\chi^{(1)}$, the linear wave equation can be simplified to

$$\nabla^2\vec{E} = \frac{\epsilon}{c^2}\frac{\partial^2}{\partial t^2}\vec{E}\,,\ \text{with}\ \epsilon = \mathrm{n}^2 \tag{2.29}$$

$$\nabla^2\vec{E} = \frac{n^2}{c^2}\frac{\partial^2}{\partial t^2}\vec{E}\,. \tag{2.30}$$

Analogously, for the magnetic part

$$\nabla^2\vec{H} = \frac{n^2}{c^2}\frac{\partial^2}{\partial t^2}\vec{H}\,. \tag{2.31}$$

The eigenvalue equations 2.30 and 2.31 for the $\vec{E}$ and $\vec{H}$ field are decoupled, but the two fields are related by boundary conditions. If an interface between two dielectric media with a vector $\vec{e}_n$ normal to this interface is considered, the fields on both side of the interface (denoted with the subscripts 1 and 2) are related by [17]

$$\vec{e}_n\left(\vec{B}_2 - \vec{B}_1\right) = 0 \tag{2.32}$$

$$\vec{e}_n\left(\vec{D}_2 - \vec{D}_1\right) = 0 \tag{2.33}$$

$$\vec{e}_n \times \left(\vec{E}_2 - \vec{E}_1\right) = 0 \tag{2.34}$$

$$\vec{e}_n \times \left(\vec{H}_2 - \vec{H}_1\right) = 0\,. \tag{2.35}$$

Which means that the normal components of $\vec{B}$ and $\vec{D}$ as well as the tangential components of $\vec{E}$ and $\vec{H}$ are continuous at the interface between media 1 and 2.
Choosing suitable cylindrical coordinates an ansatz-function

$$E = E^0\Psi ZT \tag{2.36}$$

can be made with

$$\Psi = \Psi_{(r,\phi)};\ Z = Z_{(z)} = e^{i\beta z};\ T = T_{(t)} = e^{i\omega t}\,. \tag{2.37}$$

To solve 2.31 the field amplitude E^0 can be separated because of the claimed linearity. Because of the isotropy the term $\nabla(\nabla\cdot\vec{E})$ in 2.22 vanished and transversal

and longitudinal coordinates can be separated. Ψ which is sometimes referred to as *phasor* represents the field distribution in the plane normal to the axis of the fiber (z-axis). The field E is harmonically oscillating in time with a single angular frequency ω and therefore called time-harmonic expressed by the term T. With the help of Fourier analysis any time-varying field can be expressed in terms of time-harmonic components. Z describes a propagating wave with a *propagation constant* β which is the z-component of the wave vector $\vec{k}$ inside the fiber. β determines how the phase and amplitude varies along the propagation direction z. β may be complex. Its real part describes the number of wavelengths per 2π units of propagation distance, whereas the imaginary part describes optical gain or loss.
By inserting 2.36, the linear wave equation 2.30 can be solved for a step index fiber. Since for specialty fibers, which are the main topic of this work, no closed-form solution can be found the further discussion is limited to some general remarks before continuing with the description of more general numerical solutions.

2.2.2 Modes of Optical Fibers

The procedure of solving the linear wave equation 2.30, with the help of the ansatz-function 2.36, for step index fibers can be found in textbooks [16, 18]. The solutions called (optical) modes are described by their transverse field distribution Ψ and their propagation constant β. Instead of β the *effective refractive index* n_{eff} (sometimes referred to as modal index) defined as

$$n_{\text{eff}} = \beta\frac{\lambda}{2\pi} = \frac{\beta}{k_0} \tag{2.38}$$

can be used to specify the modes. Both may be complex; the imaginary part describes optical gain (if negative) or loss (if positive). The value of the effective refractive index of a core mode guided by TIR has to be in between the refractive indices of core and cladding

$$n_{co} > n_{\text{eff}} > n_{cl}\ . \tag{2.39}$$

The modes can be sorted by their n_{eff}. The mode with the lowest n_{eff} is the 1st or *fundamental mode*. Subsequent modes have increasing effective refractive indices and are referred to as higher-order modes (HOMs). If a mode has a n_{eff} close to the refractive index of the cladding, the mode is only weakly guided and easily gets attenuated by bending the fiber.

In the following, a classification scheme of the modes is given and examples are shown by plots of their field distribution $\Psi_{(r,\phi)}$. If the electric and the magnetic field of a mode are orthogonal to the direction of propagation ($E_z = 0$, $H_z = 0$), as for plane waves in free space, the mode is transversal electromagnetic (TEM). Modes in an optical fiber can be classified accordingly [19]:

- TE (transverse electric) modes: vanishing electric field in the direction of propagation ($E_z = 0$, $H_z \neq 0$)
- TM (transverse magnetic) modes: vanishing magnetic field in the direction of propagation ($E_z \neq 0$, $H_z = 0$)
- EH, HE (hybrid) modes: nonzero electric and magnetic fields ($E_z \neq 0$, $H_z \neq 0$), referred to as HE or EH depending on which field has a larger component in the direction of propagation

The solutions to the wave equation 2.30 in optical fibers are TE, TM, EH, and HE modes as represented by the electric field distributions in figure 2.2.
Usually for silica step index fibers (SIF) the difference of the refractive index between the fiber core and the fiber cladding is small and the so-called *weakly guiding approximation* [18]

$$\Delta_n = \frac{n_{co}^2 - n_{cl}^2}{2n_{co}^2} << 1 \tag{2.40}$$

can be used which again leads to TEM modes which are linearly polarized (LP).
Since the weakly guiding approximation is extensively used, modes of optical waveguides are often described as LP modes. Except for the fundamental (lowest-order) mode these LP modes are not the exact modes of the fiber.
However, for weakly guiding fibers (2.40) the exact solutions are sets of modes with (nearly) identical propagation constants and therefore called (near) degenerate. Linear combinations of these sets of degenerate modes correspond to particular LP modes as described by table 2.1.

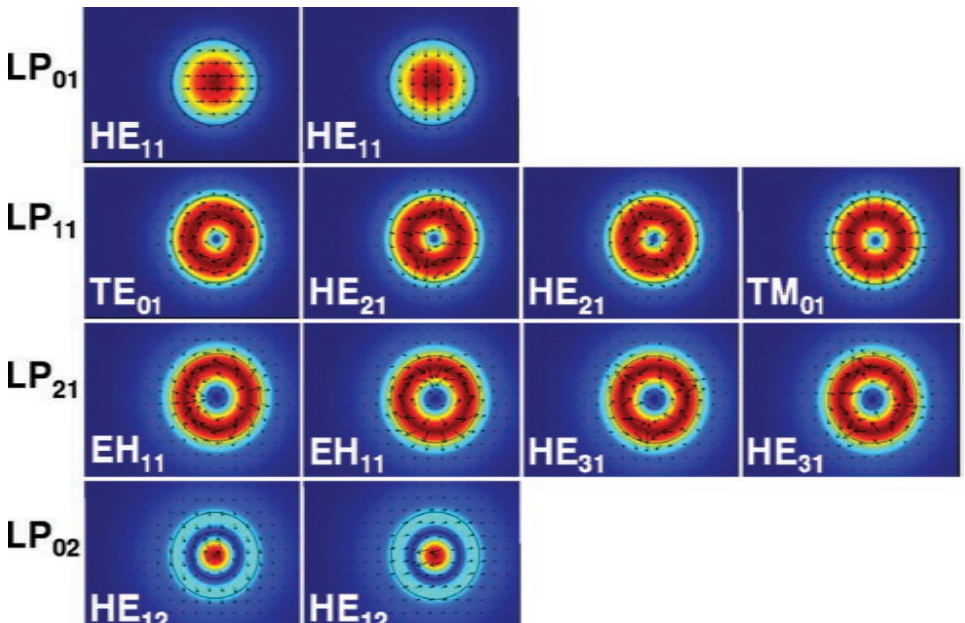

Figure 2.2: Calculated mode structure of a step index fiber (r_{co} = 30µm, NA = 0.06). The color distribution corresponds to the intensity of the electric field and the arrows correspond to the polarization of the electrical field. The linearly polarized LP modes can be generated from superpositions of the exact solutions (TE, TM, HE, EH).

Linearly polarized	Exact
LP_{01}	HE_{11}
LP_{11}	HE_{21}, TE_{01}, TM_{01}
LP_{21}	HE_{31}, EH_{11}
LP_{02}	HE_{12}
LP_{1m}	HE_{2m}, TE_{0m}, TM_{0m}
LP_{lm} $l \neq 0$ or 1	HE_{l+1m}, EH_{l-1m}

Table 2.1: Correspondence between LP modes and the exact modes from which they can be formed [19].

In view of the power handling capabilities of a fiber, an important property of the modes is the *mode field area* (MFA) or *effective mode area* A_{eff} which is defined as [16]

$$A_{\text{eff}} = \frac{\left(\int\int \vec{E}\vec{E}^* dxdy\right)^2}{\int\int (\vec{E}\vec{E}^*)^2 dxdy} \tag{2.41}$$

where $\vec{E}^*$ is the complex conjugate of $\vec{E}$ for a mode with arbitrary shape. To estimate the number of core-guided modes, without calculating the whole mode structure, the *normalized frequency* or V-number which is defined as [16]

$$V = \frac{2\pi}{\lambda} r_{co} \sqrt{n_{co}^2 - n_{cl}^2} = \frac{2\pi}{\lambda} r_{co} \text{NA} \tag{2.42}$$

can be used. The V-number is dimensionless and connects all structural parameters (NA, core radius) with the wavelength. Thus, it gives a complete description of the experimental situation. For large V-numbers, the number of modes within a step index fiber is approximately $V^2/2$. For a V-number of less than 2.405 only one mode is supported. Hence, the fiber is called *single-mode* (SM).

2.2.3 Nonlinear Effects in Optical Fibers

If the electric field strength $\vec{E}$ is not small enough to neglect the higher-order terms in 2.25, the linear approximation 2.26 is invalid and the effects of *nonlinear optics* become important. Because glass is an isotropic material the discussion may be restricted to the isotropic case for the following. The parallelism $\vec{E} \,||\, \vec{P}$ requires all even terms in the expansion 2.25 to be zero (particularly $\chi^{(2)} = 0$). The next non-zero term is therefore $\chi^{(3)}$. Higher-order terms ($\chi^{(5)}$, $\chi^{(7)}$,..) are small and will only contribute at extremely high intensities. As a result, in the nonlinear case the polarization series 2.25 can be approximated by

$$\vec{P} = \epsilon_0 \left(\chi^{(1)} + \chi^{(3)} \vec{E}^2 \right) \vec{E} \; . \tag{2.43}$$

Without absorption the relative permittivity ϵ becomes

$$\epsilon = 1 + \chi^{(1)} + \chi^{(3)} \vec{E}^2 = \epsilon_{linear} + \chi^{(3)} \vec{E}^2 \tag{2.44}$$

$$\epsilon = \epsilon_{linear} \left(1 + \frac{\chi^{(3)}}{\epsilon_{linear}} \vec{E}^2 \right) \; . \tag{2.45}$$

Because the nonlinear contribution is comparatively small, with $\epsilon = n^2$ it follows that

$$n = n_0 \sqrt{\left(1 + \frac{\chi^{(3)}}{1 + \chi^{(1)}} \vec{E}^2 \right)} \approx n_0 \left(1 + \frac{\chi^{(3)}}{2 n_0^2} \vec{E}^2 \right) = n_0 + \bar{n}_2 \vec{E}^2 \tag{2.46}$$

where $\bar{n}_2 = \chi^{(3)} / 2 n_0$. For fused silica $\bar{n}_{2,silica} \approx 10^{-22} m^2/V^2$ (slightly dependent on frequency and doping) [16].
With the intensity $I = (c/n_0) \epsilon_0 \epsilon \mu E^2 = n_0 \epsilon_0 c E^2$ expression 2.46 can be rewritten as

$$n = n_0 + \bar{n}_2 \frac{I}{n_0 \epsilon_0 c} = n_0 + n_2 I = n_0 + n_2 P / A_{\text{eff}} \; . \tag{2.47}$$

The nonlinear refractive index of fused silica is $n_{2,silica} = 3 \cdot 10^{-20} m^2/W$. Hence, as a result of the $\chi^{(3)}$-term a modified refractive index is obtained which depends on the intensity or the optical power P (in watts) and the effective mode area A_{eff} (in square meters). Taking 1 kW of power and a (minimal) mode field area of about $300\,\mu m^2$ as typical values relevant for this work, the nonlinear contribution to the refractive index becomes

$$n_2 I = \frac{3 * 10^{-20} m^2/W \cdot 10^3 W}{300 \cdot 10^{-12} m^2} = 1 \cdot 10^{-7} \; . \tag{2.48}$$

A comparison of this value to the difference of the refractive indices of the core and the cladding of a state-of-the-art low-NA fiber with $n_{cl} = 1.45$ and NA $= 0.07$

$$n_{co} - n_{cl} = \sqrt{n_{cl}^2 + NA^2} = 1.69 \cdot 10^{-3} \tag{2.49}$$

shows that, even at this high power level, the nonlinear part of the refractive index is negligible ($n_2 I << n_{co} - n_{cl}$).
This is a very important result because it means that it is possible to calculate the modes including mode shapes and propagation constants in the linear approximation. The previous results maintain their validity and commercial software can be used to calculate the mode structure for all situations considered in this work.
However, it should be mentioned that the nonlinear part of the refractive index changes the phase of the propagating wave which is described in the following. Other nonlinear effects limit the power handling capabilities of fibers as described in the sections 2.2.3.2 and 2.2.3.3.

2.2.3.1 Optical Kerr Effect

The *optical Kerr effect* or *self phase modulation* [16] is caused by the intensity dependence of the refractive index (2.47). After a certain distance $z = L$ the phase ϕ of a propagating wave can be described by

$$\phi = kL = k_0 nL = k_0(n_0 + n_2 I)L = \frac{2\pi}{\lambda}(n_0 + n_2 \frac{P}{A_{\text{eff}}})L \tag{2.50}$$

which can be separated into a linear term

$$\phi_{lin} = \frac{2\pi}{\lambda} n_0 L \tag{2.51}$$

and a nonlinear term

$$\phi_{nonlin} = \frac{2\pi}{\lambda} n_2 \frac{P}{A_{\text{eff}}} L = \frac{\omega_0 n_2}{c A_{\text{eff}}} PL = \xi PL \tag{2.52}$$

where $\xi = \omega_0 n_2 / c$ is called *nonlinear coefficient*. For the values stated above ($P = 1\,\text{kW}$, $A_{\text{eff}} = 300\,\mu\text{m}^2$) and a wavelength of $1\,\mu\text{m}$ a π-phase shift, corresponding to half a wavelength, is obtained for $L = 5\,\text{m}$ of the fiber length. This can be tested with an interference experiment using a reference beam.
The phase delay caused by the Kerr effect can especially be problematic for intense laser pulses. Usually, the largest phase delay occurs at the symmetry axis of the fiber

and gets smaller with increasing distance from the center because of the intensity distribution inside the fiber. This leads to a deformation of the wavefronts which can lead to a self-focusing of laser pulses.
Other effects caused by the $\chi^{(3)}$-term are frequency tripling, four wave mixing, and cross phase modulation [16]. To consider all relevant effects a nonlinear wave equation has to be formulated which is often called nonlinear Schrödinger equation. However, mode calculations can be done with the linear wave equation, as stated above, and the transport of continuous wave laser radiation is the main focus of this work the nonlinear wave equation will not be further discussed.
For high-power continuous-wave laser beam delivery other nonlinear effects are important, for example, the *inelastic scattering processes* [13]. The energy of the laser light is absorbed or lost due to inelastic scattering and its frequency is changed. Since the atoms of the glass are usually in their ground state (due to Maxwell Boltzmann distribution), energy of the guided beam, called pump, is lost. The frequency is lowered which results in *Stokes lines* in the spectrum. If the pump wave gains energy due to inelastic scattering, the higher energy photons will result in anti-Stokes lines. The photons may scatter with acoustical (Brillouin scattering) or optical (Raman scattering) phonons. For spontaneous scattering the rate is very low, but at a certain threshold power stimulated scattering occurs.

2.2.3.2 Stimulated Brillouin Scattering

Brillouin scattering describes the interaction of light with time dependent optical density variations and hence the variations of the refractive index [13]. A periodic variation of the refractive index, as caused by acoustical phonons, acts as a three-dimensional diffraction grating. Because the sound wave is traveling, the laser light is subject to a Doppler shift which causes a frequency change. An incident photon is converted into a scattered photon of slightly lower energy and a phonon.
Intense optical fields, such as high-power laser beams in optical fibers, may themselves produce acoustic vibrations in the medium via electrostriction which may then cause Brillouin scattering. This situation is termed *stimulated Brillouin scattering* (SBS) of the laser beam. The refractive index variation caused by the SBS has the effect of a Bragg mirror which usually causes the scattered photon to propagate in the opposite direction of the incident photon. This stimulated effect can easily reflect most of the incident power which may damage the laser source.

The frequency shift ν_B of the (back-)scattered photon, called Brillouin shift, can be calculated using conservation of energy and momentum which results in [16]

$$\nu_B = \frac{2v_a|\vec{k}|}{2\pi} = \frac{2v_a n}{\lambda} \,. \tag{2.53}$$

Inserting a value of $v_a = 5960\,\mathrm{m/s}$ for the speed of sound in fused silica and a refractive index of $n = 1.45$ at a wavelength of $\lambda = 1\,\mu\mathrm{m}$ leads to a Brillouin shift of $\nu_B \approx 17.3\,\mathrm{GHz}$ (or $\Delta\lambda \approx 5.77 \cdot 10^{-11}\,\mathrm{m} = 5.77\,\mathrm{pm}$). The power threshold P_B for the onset of stimulated Brillouin scattering can be approximated by [13]

$$P_B \approx \frac{21 \cdot A_{\mathrm{eff}}}{g_B(\nu) \cdot L_{\mathrm{eff}}} \tag{2.54}$$

with the frequency dependent Brillouin gain coefficient $g_B(\nu)$. The effective length $L_{\mathrm{eff}} = 1/\alpha \cdot (1 - e^{-\alpha L})L$ accounts for the power decrease during propagation due to the *attenuation* α of the fiber with length L. The SBS threshold is increased if the linewidth of the pump signal $\Delta\nu_P$ is larger than the SBS linewidth $\Delta\nu_B$ which is related to the damping of the phonons. This increase can be described by a modified Brillouin gain coefficient $\tilde{g}_B(\nu)$ [16]

$$\tilde{g}_B(\nu) = g_B(\nu)\frac{\Delta\nu_B}{\Delta\nu_B + \Delta\nu_P} \,. \tag{2.55}$$

Therefore, narrow linewidth sources have considerably lower thresholds. Present high-power fiber lasers have a rather broad linewidth. As a result, Raman scattering is usually the most dominating effect.

2.2.3.3 Stimulated Raman Scattering

While Brillouin scattering describes the interaction of light with large-scale acoustical phonons, Raman scattering describes the scattering due to interactions with vibrational (or rotational) transitions in single molecules (optical phonons).
Figure 2.3 shows the possible interactions. Usually, power is transfered to longer wavelengths (Stokes-lines) because the incident photon (i) looses energy to a vibrational state (v) which results in a scattered photon (s) with lower energy. The frequency shift or Raman shift ν_R can be calculated using conservation of energy

$$\hbar\nu_R = |\hbar\nu_i - \hbar\nu_R| \,. \tag{2.56}$$

Typical Raman shifts in silica are in the order of 10 THz [16] (or $\Delta\lambda \approx 3.45 \cdot 10^{-8}$ m $= 34.5\,\mathrm{nm}$). The more Stokes photons are present, the faster incident photons are

converted to Stokes photons. Therefore, depending on the population of the states, the Raman scattering can be stimulated.

The power threshold P_R for the onset of the *stimulated Raman scattering* (SRS) can be approximated by [13]

$$P_R \approx \frac{16 \cdot A_{\text{eff}}}{g_R(\nu) \cdot L_{\text{eff}}} \tag{2.57}$$

with the frequency dependent Raman gain coefficient indicated by $g_R(\nu)$.

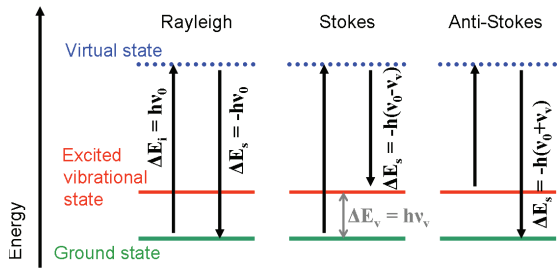

Figure 2.3: Photon scattering energy scheme. If the incident (i) and the scattered photon (s) have the same energy, the photon is Rayleigh scattered. If the scattering leads to an excited vibrational state (v), the resulting Stokes-scattered photon has a lower energy. The scattered photon may receive energy from an already excited state which leads to anti-Stokes scattering.

2.3 Attenuation and Losses

In theory, the TIR mechanism used to guide light in step index optical fibers is lossless, but in practice, some light is lost due to absorption and scattering by the material of the fiber. In the absence of localized defects, the launched power P_{in} is reduced by the fiber attenuation α (usually given in dB/km) and the transmitted power P_{out} depends on the length of the fiber L

$$P_{out} = P_{in} 10^{-\alpha L} \,. \tag{2.58}$$

State of the art telecommunication fibers achieve attenuations as low as 0.2 dB/km in the lowest loss regime at $\lambda = 1.55\,\mu\text{m}$ and still slightly less than 1 dB/km at $\lambda = 1\,\mu\text{m}$. In this regime, the main contribution to the losses is Rayleigh scattering caused by unavoidable density fluctuations in the glass. Impurities (H_2O, Fe, Cu, Co,..) may cause additional losses. Further losses arise due to non-uniformities of the doping concentration and variations of the core diameter as well as of the symmetry along the fiber. Because many interfaces can be present in specialty fibers, surface roughness becomes an important cause for losses resulting in higher attenuations compared to step index fibers.
Besides the intrinsic attenuation of the fiber, additional losses may occur due to stress or fiber bends. Pressure may change the refractive index profile and the geometry. Either deteriorate the propagating mode and cause losses.
More important are losses due to fiber bends which are usually divided into *macro bending losses* and *micro bending losses*.

2.3.1 Macro Bending Losses

The great advantage of optical fibers is their flexibility. However, bending the fiber (usually with a radius of a few cm) causes additional losses which are referred to as macro bending losses. It is known from the wave-optical description, that the light is not completely restricted to the core. Some part of the power is transported inside the cladding which can be described by evanescent waves.
Considering the different path lengths indicated by figure 2.4, it becomes obvious that(due to the finite speed of light) the phase front is deformed by the bend which results in a radial component of the Poynting vector ($\vec{S} = \vec{E} \times \vec{H}$) implying a loss of the energy guided by the fiber.

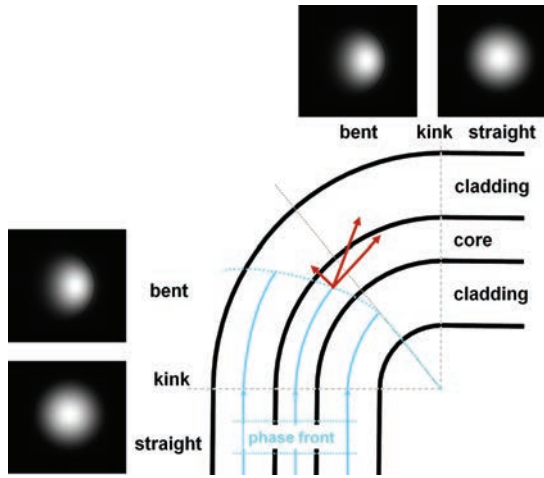

Figure 2.4: Scheme of a bent fiber. The phase front of a mode is indicated by the dotted blue lines. The bent-induced mode field deformation is shown by the intensity distributions.

This shows as well that, if the light is strongly confined in the core as in case of high-NA fibers, the bending losses should be lower compared to a low-NA fiber with the same core size because a larger part of the power is propagating in the fiber cladding of the low-NA fiber resulting in a stronger radial component of the pointing vector.

A high value of Δ_n (2.7) ensures a good confinement in the core. For SM telecommunication fibers with NA$= 0.14$ (e.g., Corning SMF-28), which are used close to the cutoff (V between 2.1 and 2.4), the macro bending losses are negligible. However, in case of low-NA fibers (NA$= 0.05 - 0.07$), this effect becomes important and is typically exploited in fiber oscillators to ensure a (close to) SM output even with MM active fibers [20, 12].

In addition to this geometrical effect, compression of the inner and extension of the outer side of the fiber bend causes stress which increases the refractive index of the glass material at the inner side and lowers it at the outer side. This *elasto-optical*

effect is counteracting the geometrical effect but it is not strong enough to compensate for it [16]. Further losses occur because the modes in bent fiber sections are different from the eigenmodes of the straight fiber which causes mode matching losses. This is illustrated by the intensity distributions in figure 2.4 at the kinks with an abrupt change of the curvature between the straight and the bent fiber. With a smooth transition of the bending radius form straight to $R = R_{min}$, these losses can be strongly reduced. Usually, the fiber coating and jacketing are used to restrict the bending radius to values above a certain critical radius ($R > R_{crit}$) to keep the macro bending losses manageable.

2.3.2 Micro Bending Losses

Micro bending losses arise due to very short bends with very small radii (µm to mm) often caused by the surface on which the fiber is laid or spooled even when the fiber is kept macroscopically straight. Therefore, the losses depend on the spooling of the fiber and on the quality of the surface it is in contact with.
Another influence which can add to the micro bending losses is directly related to the coating. During the drawing, the bare fiber is fed through a coating bath. The liquid coating is cured on the fiber by UV-lamps or heat which usually results in a contraction of the coating leading to a pressure applied to the fiber. Especially, if the coating is not deposited symmetrically on the bare fiber, the micro bending losses can be significantly enhanced. Using a large cladding diameter reduces this influence.
In MM fibers the coupling between different modes may contribute to additional power losses of an initially excited fundamental mode.

2.4 Mode Coupling

The eigenmodes of an ideal MM fiber are orthogonal, which means, that they do not interact and power is not exchanged between these modes.
But disturbances, such as small index variations, geometrical variations, or fiber bends, alter the mode structure of real fibers. The eigenmodes of the ideal fiber differ from those of the disturbed fiber. For the sake of analytical considerations it is usually easier to use the known eigenmodes of the ideal fiber to describe the modes in the perturbed fiber by decomposing the propagating fields into the known eigenmodes $E_\nu = E_\nu^0 \Psi_\nu(r,\phi) e^{i\beta_\nu z} e^{i\omega t}$ (for mode number ν) with the help of expansion coefficients which are no longer constants of propagation ($E_\nu^0 \rightarrow E_\nu^0(z)$) [21]. Without considering the time-harmonic oscillation the electric field of the perturbed fiber E^{pert} can be expressed as

$$E^{\mathrm{pert}} = \sum_\nu E_\nu^0(z) \Psi_\nu(r,\phi) e^{i\beta_\nu z} \,. \tag{2.59}$$

The change of the field amplitudes $E_\nu^0(z)$ (expansion coefficients) with the propagation along the z-axis can then be described by coupled differential equations with the help of *coupling coefficients* $\kappa_{\nu\mu}$. To keep this description concise, only the coupling between two modes is discussed below, but the concept is applicable to an arbitrary number of modes. In general, the coupled mode equations for two modes can be written as [22]

$$\frac{dE_1}{dz} = i\beta_1 E_1 + \kappa_{12} E_2 \tag{2.60}$$

$$\frac{dE_2}{dz} = i\beta_2 E_2 + \kappa_{21} E_1 \tag{2.61}$$

where the complex propagation constants $\beta_1 = \beta_{1r} + i\beta_{1i}$ and $\beta_2 = \beta_{2r} + i\beta_{2i}$ contain the loss coefficients of each mode in the absence of coupling. The coupling coefficients obey a symmetry relation [22]

$$\kappa_{12} = -\kappa_{21}^* \,. \tag{2.62}$$

It is convenient to express the z-dependence of the coupling coefficients explicitly, for example,

$$\kappa_{12} = iK f^{\mathrm{pert}}(z) \tag{2.63}$$

with K being real and a function f^{pert} which depends on the nature of the perturbation (usually containing a changed refractive index distribution).

If the distortion can be described by a refractive index variation of the waveguide material at the position $z = \tilde{z}$, the coupling constants can be calculated with the help of overlap integrals [21] over the area of the cross section of the fiber

$$\kappa_{12} \propto \int_A \Psi_1^*(x,y)\,|n(x,y,z<\tilde{z}) - n(x,y,z=\tilde{z})|\,\Psi_2(x,y)dA \tag{2.64}$$

where $\Psi_1^*(r,\phi)$ is the complex conjugate of the transverse field distribution $\Psi_1(r,\phi)$ of mode 1.
An arbitrary perturbation f^{pert} can be written as a Fourier series

$$f^{\text{pert}} = \sum_{N=1}^{\infty} 2b_N(\cos(\Theta_N z) + i\sin(\Theta_N z)) = \sum_{N=1}^{\infty} 2b_N e^{i(\Theta_N z)} \tag{2.65}$$

with real values of b_N and the spatial frequency

$$\Theta_N = 2\pi/L^{\text{pert}} N\,, N = 0,1,2,.. \tag{2.66}$$

where L^{pert} has the unit of a length. According to Marcuse [22, 23] only the Fourier component of f^{pert} at the spatial frequency $\Theta = \beta_{1r} - \beta_{2r}$ contributes to the coupling between the two modes in first-order perturbation theory. This allows to rewrite 2.60 and 2.61 with the help of 2.62 as

$$\frac{dE_1}{dz} = i\beta_1 E_1 + iKbE_2 e^{-i(\beta_{1r}-\beta_{2r})z} \tag{2.67}$$

$$\frac{dE_2}{dz} = i\beta_2 E_2 + iKbE_1 e^{i(\beta_{1r}-\beta_{2r})z} \tag{2.68}$$

using only the term f^{pert} which contributes to the mode coupling and therefore dropping the index N of b_N. Following the derivation of Marcuse [22] new variables $\tilde{E}_1$ and $\tilde{E}_2$ are defined as

$$E_1(z) = \tilde{E}_1(z) e^{-\frac{1}{2}i(\beta_{1r}-\beta_{2r})z} \tag{2.69}$$

$$E_2(z) = \tilde{E}_2(z) e^{\frac{1}{2}i(\beta_{1r}-\beta_{2r})z} \tag{2.70}$$

and substituted into 2.67 and 2.68. This leads to new coupled mode equations which, in contrast to the initial equations 2.67 and 2.68, are coupled by a constant coupling coefficient $\kappa = Kb$.

$$\frac{d\tilde{E}_1}{dz} = i\beta_1 \tilde{E}_1 + i\kappa \tilde{E}_2 \tag{2.71}$$

$$\frac{d\tilde{E}_2}{dz} = i\beta_2 \tilde{E}_2 + i\kappa \tilde{E}_1 \tag{2.72}$$

According to [22], these new equations derived by using only the spatial Fourier component of 2.65 with $\Theta = \beta_{1r} - \beta_{2r}$ are good approximations of 2.60 and 2.61.
If the perturbation function f^{pert} represented by 2.65 has no spatial Fourier component (2.66) which matches the two modes, the difference of the propagation constants $\Delta\beta_{12} = |\beta_1 - \beta_2|$ referred to as phase difference of the co-propagating modes will prevent the coupling unless $\beta_1 \cong \beta_2$.
Which means if the *phase matching condition* [22]

$$|\beta_1 - \beta_2| = \Theta_N = 2\pi/L^{\text{pert}}N \,, \text{with} \,, \text{N} = 0, 1, 2, .. \tag{2.73}$$

is not satisfied for any integer N, the modes remain efficiently uncoupled. Since Θ_N is real, only the real parts of the propagation constants are considered in 2.73.
The effect of the imaginary parts, thus the losses of the two modes, on the coupling was investigated by Zhang *et al.* [24]. Before continuing with the derivation of a condition for the imaginary parts of the modes it is helpful to consider the illustrative results of a numerical simulation.
Zhang *et al.* were working with FEM-simulations similar to those used within this work (which are described in chapter 3). They investigated the wavelength-dependent coupling of a core mode and a cladding mode in a special microstructured fiber. At a certain wavelength, the phase matching condition (2.73) is fulfilled and the two modes couple. Figure 2.5 [24] shows the real (a) and the imaginary parts (b) of the effective refractive indices of the core and the cladding mode which is denoted as defect mode. At the anti-crossing point indicated in (a) the imaginary parts of both modes are equal as shown in (b). During the variation of the wavelength, the power from the core mode is completely coupled to the defect mode and vice versa as indicated by the insets.
To investigate the influence of the losses on the coupling, Zhang *et al.* increased the loss difference between the two modes by changing the special cladding of the microstructured fiber. The losses of the cladding mode were increased without affecting the core-guided mode and the simulations were repeated.
The phase matching condition (2.73) is fulfilled again, but in this case there is no anti-crossing of the real parts as shown in figure 2.6(a) and the loss curves shown in figure 2.6(b) do not intersect. The losses of the fundamental core mode are increased at the phase matching point, but the complete coupling (or complete energy transfer) was prevented by the increased difference of the losses of the two modes.

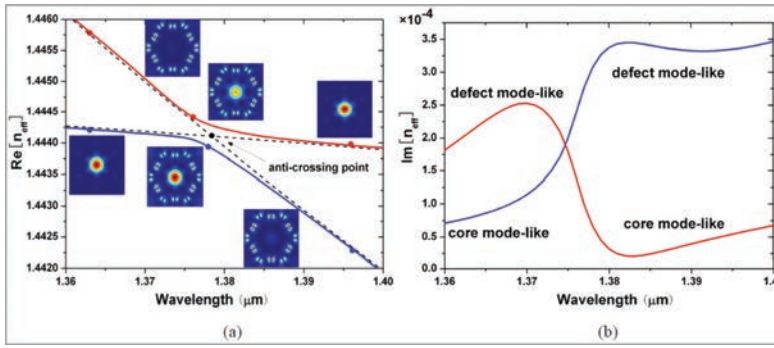

Figure 2.5: Analyses of real parts (a) and imaginary parts (b) of the effective mode indices n_{eff} of two modes as a function of the wavelength taken from [24] in case a complete coupling occurs. The insets show the intensity distributions of the coupled modes at selected wavelengths.

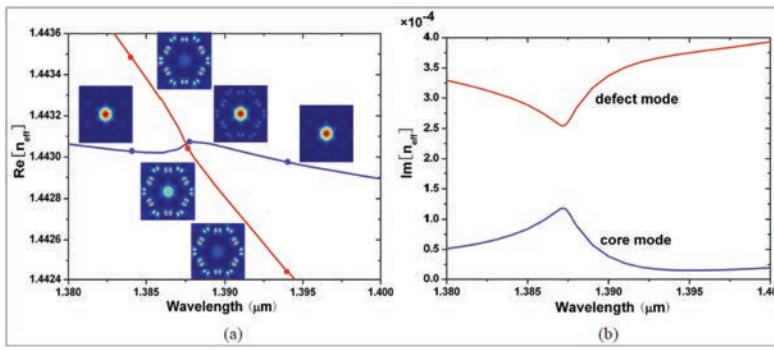

Figure 2.6: Analyses of real parts (a) and imaginary parts (b) of the effective mode indices n_{eff} of two modes as a function of the wavelength taken from [24] in case an incomplete coupling occurs. The insets show the intensity distributions of the coupled modes at selected wavelengths.

The crossing is a signature of both modes following their "natural" dispersion curves. The anti-crossing instead shows an influence of one mode on the other indicating the influence of the coupling of the two modes.

As a next step, a condition which has to be fulfilled in order to allow mode coupling depending on the imaginary parts is derived from equations 2.71 and 2.72. Following the argumentation of Zhang *et al.* [24], solutions of the form $\tilde{E}_1 = \tilde{E}_1^0 e^{i\beta z}$ and $\tilde{E}_2 = \tilde{E}_2^0 e^{i\beta z}$ are assumed with β as the propagation constant of the coupled modes. Substituting these fields into 2.71 and 2.72 leads to

$$\beta\tilde{E}_1^0 = \beta_1\tilde{E}_1^0 + \kappa\tilde{E}_2^0 \tag{2.74}$$

$$\beta\tilde{E}_2^0 = \beta_2\tilde{E}_2^0 + \kappa\tilde{E}_1^0\,. \tag{2.75}$$

These coupled equations can be rewritten into a matrix form

$$\begin{pmatrix} \beta-\beta_1 & -\kappa \\ -\kappa & \beta-\beta_2 \end{pmatrix} \begin{pmatrix} \tilde{E}_1^0 \\ \tilde{E}_2^0 \end{pmatrix} = 0\,. \tag{2.76}$$

By using

$$\det \begin{pmatrix} \beta-\beta_1 & -\kappa \\ -\kappa & \beta-\beta_2 \end{pmatrix} = 0\,, \tag{2.77}$$

the propagation constant of the coupled modes β can be expressed as

$$\beta_\pm = \beta_{\text{ave}} \pm \sqrt{\delta^2+\kappa^2} \tag{2.78}$$

with $\beta_{\text{ave}} = (\beta_1+\beta_2)/2$ and $\delta = (\beta_1-\beta_2)/2)$ ($\beta_1 = \beta_{\text{ave}}+\delta$, $\beta_2 = \beta_{\text{ave}}-\delta$). To check the consistency of this equation one can see what happens if the coupling vanishes ($\kappa \to 0$). Equation 2.78 then gives the initial modes with β_1 and β_2 ($\beta_\pm = \beta_{\text{ave}} \pm \sqrt{\delta^2+0} = \beta_{\text{ave}} \pm \delta = (\beta_1+\beta_2)/2 \pm (\beta_1-\beta_2)/2) = \beta_{1/2}$).
Now the coupling with $\kappa \neq 0$ is considered. For bound modes, the propagation constants β_1 and β_2 are both real. Hence, δ is also real and $\sqrt{\delta^2+\kappa^2}$ is larger than zero. β_+ cannot be equal to β_-, even at the "crossing" point where δ goes through zero, and a regular anti-crossing is taking place. This corresponds to the situation displayed in figure 2.5(a) even though the modes considered there are lossy. This is because the loss difference is small as explained in the following.
For leaky modes, β_1 and β_2 are both complex, hence δ may be complex and can be

written as $\delta = \delta_r + i\delta_i$. At the phase matching point, the real parts of the propagation constants of the two leaky modes are equal which means $\delta_r = 0$. Hence,

$$\delta^2 + \kappa^2 = -\delta_i^2 + \kappa^2 \,. \tag{2.79}$$

By inserting 2.79 into 2.78 one can easily see that if $\delta_i < \kappa$, then β_+ and β_- have different real parts but equal imaginary parts, and a complete coupling (regular anti-crossing) between the two leaky modes occurs. If $\delta_i > \kappa$, then β_+ and β_- have equal real parts but different imaginary parts and an incomplete coupling appears. The two modes actually cross.
A regular anti-crossing can therefore only happen if $\kappa > \delta_i$. From $\delta = (\beta_1 - \beta_2)/2$ and $\delta = \delta_r + i\delta_i$ follows $\delta_i = (\beta_{1i} - \beta_{2i})/2$. Hence the *loss matching condition* can be written as

$$\kappa > 1/2 \left| \mathrm{Im}(\beta_1) - \mathrm{Im}(\beta_2) \right| \,. \tag{2.80}$$

Only if this conditions is fulfilled a complete coupling can happen. Otherwise, it is possible for the two perturbed modes to have equal real parts and a crossing of the two modes takes place [24].
As a result, mode coupling does not happen easily in leaky optical fibers because it requires phase matching (2.73) and loss matching (2.80) at the same time. A similar result was obtained by Marcuse using coupled power equations instead of coupled field equations [25]. In the case of incomplete coupling the losses of a propagating fundamental mode can be increased at the phase matching point where the real parts of the propagation constants (or effective refractive indices) are equal as can be seen in figure 2.6 (b) but a complete energy transfer or oscillation between these modes is not happening. This offers the possibility to prevent the losses of a fundamental mode due to mode coupling by tailoring the losses of the fiber modes. Usually, the phase matching condition is not fulfilled in unperturbed fibers, but if the core radius is large, the real part of the effective refractive index of subsequent modes is similar and the loss matching condition could be used to avoid mode coupling.

2.4.1 Loss Management and Confinement Loss

Some specialty fibers such as photonic bandgap fibers and leakage channel fibers (which will be described in sections 2.6.3 and 2.6.4) use intentionally introduced losses to increase the quality of the delivered beam. So far, this has mainly been

investigated in the context of active fibers in which these losses prevent the lasing of HOMs. However, with the knowledge of the previous chapter, showing that mode coupling only occurs if both phase and loss matching is fulfilled; loss management can also be used to maintain the beam quality in passive fibers as is investigated within this work.

Fibers which are used for loss management have a special cladding which prevents a complete TIR. As a result, all modes are lossy but it is possible to make fibers for which the losses of the fundamental mode α_{FM} are acceptable or even negligible. For instance, if the losses are much smaller than the material absorption of the waveguide $\alpha_{\mathrm{FM}} << \alpha_{\mathrm{material}}$.

At the same time, the losses of HOMs may be very high because their fields penetrate further into the cladding. Such a fiber is mode filtering and for a sufficient length only the fundamental mode can be observed at the fiber output even when the beam was MM at the beginning. Therefore, such fibers are called *asymptotically single-mode*. The power in the other modes is simply coupled (which means lost) to cladding or radiation modes. This concept is based on *loss management* where the quotient $\alpha_{\mathrm{FM}}/\alpha_{\mathrm{HOM}}$ between the losses of the fundamental mode α_{FM} and the next higher-order mode (or the mode with the second highest losses) α_{HOM}, usually α_{LP11}, is an important parameter referred to as *loss ratio*. This parameter is especially important for active fibers in which high losses prevent HOMs from lasing. Less established is the knowledge that the coupling between a well-guided fundamental mode to HOMs can be avoided by a sufficient loss difference as shown in the previous section.

In theory, the overall losses of a mode are characterized by the imaginary part of its effective refractive index. Hence, the losses can be calculated using the complex effective refractive index n_{eff}.

Since absorption and scattering losses depend on the quality of the material and the fiber production, such losses are usually neglected within the simulations and characterized later by empirical values. The calculation of a complex n_{eff} is necessary to design fibers which are making use of loss management.

If the power of the fundamental mode is lost due to coupling to HOMs, not only the efficiency of the beam transport may be reduced, but also the beam quality changes.

2.5 Beam Quality and Beam Propagation Factor

If a fiber guides more than just one mode, a SM free space beam which is focused into a fiber can excite several fiber modes in case of imperfect mode matching. Even if only the fundamental mode is excited at the fiber input, defects in the fiber or distortions, such as fiber bends, may couple different modes which results in a MM beam at the fiber end.

Within the laser community, the product of the divergence half-angle θ and the radius of the waist ω (the narrowest point) of a laser beam called *beam parameter product* (BPP) is commonly used to quantify the focusability of a laser beam [26]. The BPP of a fiber, defined by the core radius and the NA,

$$r_{co}\mathrm{NA} \geq \theta\omega \tag{2.81}$$

has to be larger than the BPP of the laser in order to accept the beam. The smaller the BPP, the better the focusability of the laser beam. The lowest possible BPP

$$\theta_0\omega_0 = \frac{\lambda}{\pi} \tag{2.82}$$

is given by the diffraction limit and fulfilled by the Gaussian beam. The ratio of the BPP of an actual beam over that of an ideal Gaussian beam at the same wavelength λ is referred to as *beam propagation factor* M^2 (commonly called "M squared")

$$M^2 = \theta\omega \cdot \frac{\pi}{\lambda}\,. \tag{2.83}$$

Hence, the M^2-value of a diffraction-limited Gaussian beam is 1. Smaller values are not possible. The M^2-factor is a simple method to quantify a beam quality with a single number (or one for each plane of symmetry if the beam is not circularly symmetric). Furthermore, it can be used to predict the evolution of the beam radius by simply replacing the wavelength with M^2 times the wavelength in all equations of the Gaussian beam analysis [26].

However, it has the drawback that the M^2-value does not give information about the power distribution in different modes. The M^2-value is ambiguous. The same values might be obtained for beams with different mode compositions. Even worse, a single higher-order mode, which could be transformed to an almost diffraction-limited beam by means of diffractive optics, may have a higher M^2-value than a multimode beam which cannot be converted to a (close to) diffraction-limited beam. Therefore,

it is questionable to use the M^2-value to quantify the beam quality. However, if the M^2-value is close to 1.0, HOMs cannot be significant and the beam quality is said to be good.

To determine the beam propagation factor M^2 the beam waist and the divergence of the beam have to be known. Both can be obtain by measuring the caustic or by measuring the size of the near- and the far-field as well as the distance between them. Different definitions to determine the beam size exist. For example, a decrease of the intensity to $1/e^2$ of the maximum intensity, a full width at half-maximum (FWHM), or a radius including 86% of the beam energy can be used as a definition. Such criteria are suitable for laser beams with a high beam quality, but to predict the evolution of an arbitrary intensity distribution correctly the definition according to ISO Standard 11146 [27], based on the second moments of the intensity distribution I(x,y), should be used. It can be written as

$$\omega_x = 2\sqrt{\frac{\int x^2 I(x,y)dxdy}{\int I(x,y)dxdy}}, \tag{2.84}$$

if the coordinates are defined relative to the center of gravity of the intensity distribution (first moments vanish) and accordingly for the radius in y-direction ω_y. For Gaussian beams, the second moment method gives the same result as the $1/e^2$ method, whereas for other intensity distributions there can be significant deviations. The M^2 factor of Hermite-Gaussian modes H_{nm} (rectangular coordinate system) with indices n and m is $M^2_{HG,mn,x} = (2m+1)$ in x-direction and $M^2_{HG,mn,y} = (2n+1)$ in y-direction [26], whereas for Laguerre-Gaussian modes L_{pl} (cylindrical coordinate system) it can be obtained by $M^2_{LG} = 2 * p + l + 1$ [28].

In the case of optical fibers, the near-field (NF) intensity distribution is given by the eigenmodes. Each mode of the fiber has a certain divergence when leaving the fiber. The divergence of the highest guided mode defines the acceptance angle of the fiber. The NF of a fiber mode is obtained by an eigenmode calculation (as will be described in chapter 3.1), but the far-field (FF) has to be calculated as well in order to obtain the beam propagation factor M^2 of a certain fiber mode.

The *Kirchhoff integral* [26], which describes the propagation of electromagnetic waves in homogeneous media, can be used within the paraxial approximation. It describes the field E at the position $\vec{x}_2$ as an integral over the plane (x_1, y_1) at z_1

$$E(\vec{x}_2) = E(x_2, y_2, z_2) = \int\int \frac{i}{\lambda} E(x_1, y_1, z_1) \frac{e^{ik\rho(x_1,y_1,z_1,x_2,y_2,z_2)}}{\rho(x_1, y_1, z_1, x_2, y_2, z_2)} dx_1 dy_1 \tag{2.85}$$

with the distance between $\vec{x}_2$ and $\vec{x}_1$

$$\rho(\vec{x}_1, \vec{x}_2) = \sqrt{L^2 + (x_2 - x_1)^2 + (y_2 - y_1)^2} \tag{2.86}$$

and the propagation distance $L = z_2 - z_1$.
In case of the fibers, the refraction at the glass-air-interface has to be considered when calculating the FF form the eigenmode.

2.6 Specialty Fibers

The goal of laser beam transport in the kW regime is not achievable with SM telecommunication fibers. Even if the fiber would not be burned directly by the high powers, nonlinear effects such as SBS (section 2.2.3.2) or SRS (section 2.2.3.3) would render the delivery of the laser beam impossible. On the other hand, multi-kW multimode beam delivery for material processing with solid-state lasers is state-of-the-art.
The problems arise with increasing beam quality of the laser sources especially fiber and thin-disc lasers. If a high-power SM (or close to SM) laser beam is delivered with state-of-the-art MM (step index) fibers for high-power lasers with core sizes of about 100-1000 µm, the beam quality usually deteriorates during propagation due to the large number of modes and the low mode spacing (small Δn_{eff}) which favors mode mixing because the phase matching condition 2.73 is more likely fulfilled and the loss matching condition 2.80 is fulfilled anyways (the modes are guided by TIR). Since standard SM fibers do not have the necessary power handling capabilities, alternatives were investigated during the last years.

2.6.1 Low-NA Fibers

The most direct approach to increase the power handling capabilities and the threshold of nonlinear effects, in particular SBS and SRS, is to increase the mode field area (2.41) of standard SM fibers. This implies to increase the core size and to compensate for it by reducing the NA of the step index fiber to keep the V-number (2.41) low in order to prevent the appearance of HOMs (see section 2.2.2). Usually, this approach is limited to core diameters of less than 15 µm because lower NAs cannot be manufactured reliably.
A special class of such *low-NA fibers*, produced to match with the active fibers of present fiber lasers, is slightly multimode and therefore called *few-mode*. Such fibers with core sizes between 20-30 µm and NAs between $0.05 - 0.08$ are often referred to as *large mode area* (LMA) fibers. However, their cores and mode field areas are small in comparison to the fibers usually used for MM multi-kW beam transport.

2.6.2 Multicore Fibers

Another approach to increase the mode field area is to assemble several cores in a common cladding to distribute the power in order to increase the power handling

capabilities. The cores have to be coherently coupled in order to to maintain a high beam quality. Hence, such a fiber is called *multicore fiber* (MCF).
Usually, identical cores are coupled. In most cases coupled mode theory is applied to model and understand such structures [29] which leads to 2N-modes if N single-mode cores are coupled. The eigenmodes of the coupled cores are called supermodes. The core size, the core-to-core distance, and the NA of the single core defines the coupling strength between the modes of the different cores. Therefore, the NA of the fiber can be tailored very well and fibers with extremely low effective NA, not reliably accomplishable as single core step index fibers, are possible to produce.
One approach within this work was to design a MCF in such a way that a laser beam can be coupled to a single Gaussian-like fundamental supermode by means of simple optics without shaping the beam beforehand.

2.6.3 Photonic Bandgap Fibers

Another possibility to guide light is to trap the light inside the fiber core by creating a forbidden region in which no propagation of light of a given wavelength is allowed. Such a region is formed by a microstructured fiber cladding consisting of periodic variations of refractive index forming a *photonic crystal* which creates a *photonic bandgap* (PBG). Since index guiding is not needed in such structures, the refractive index of the core may be lower than the refractive index of the cladding. Even hollow cores are possible.
The earliest idea of such fibers was based on a cladding of concentric rings with different refractive indices, similar to a Bragg mirror, but in a cylindrical configuration [30]. A fiber based on this concept is called *Bragg fiber* (BF).
Another concept, which had a higher impact, is based on tiny air holes arranged to form a two dimensional (2D) crystal lattice running all along the whole fiber. Such fibers are called *photonic crystal fibers* (PCF) [31, 32]. However, the expression is widely used to term all kinds of microstructured fibers, even if a photonic bandgap is not present, as in the case of leakage channel fibers which are presented in section 2.6.4. Without total internal reflection (TIR), photonic bandgap fibers do not exhibit any truly guided modes. They always have a finite cladding and light can tunnel trough the region creating the photonic bandgap. Therefore, all modes are lossy. The concept is based on loss management (see section 2.4.1) of the different modes. Such a fiber may be mode filtering and for sufficient length only the funda-

mental mode will be observed at the fiber output, even if the beam was MM at the beginning. Therefore, these fibers are asymptotically SM but PCFs which exhibit only one core-guided mode are also possible.

2.6.3.1 Bragg Fibers

The photonic bandgap of BFs is achieved by a microstructured region consisting of several alternating concentric high and low refractive index layers as shown in figure 2.7. Solid-core BFs can be fabricated by standard modified chemical vapor deposition (MCVD) processes [33, 34].
The guiding mechanism in BF can be understood with an antiresonant reflecting optical waveguide (ARROW) model in which each layer of the multilayer cladding can be considered as a Fabry-Perot resonator [35, 36]. The light is trapped inside the core for wavelengths at which these resonators are antiresonant as sketched in figure 2.7. Depending on the refractive indices n_a and n_b as well as the core radius r_{co}, the layer thicknesses a and b can be optimized to reduce the losses for a certain wavelength λ. In case of $\lambda/R_{core} << 1$, simple considerations lead to the conditions for the optimum high-index layer thickness a

$$a = \frac{(2l+1)\lambda}{4\sqrt{n_a^2 - n_b^2 + \frac{\lambda^2}{(2r_{co})^2}}} \ , \ l = 0, 1, 2, ... \tag{2.87}$$

and the optimum low-index layer thickness b

$$b = (2m+1)r_{co} \ , \ m = 0, 1, 2, ... \ , \tag{2.88}$$

to achieve the lowest propagation losses in straight Bragg fibers [35, 36]. By using a semi-analytical iterative approach new and improved conditions for the layer thicknesses, which significantly reduce the losses especially for bent fibers, are presented in chapter 5.2.2.

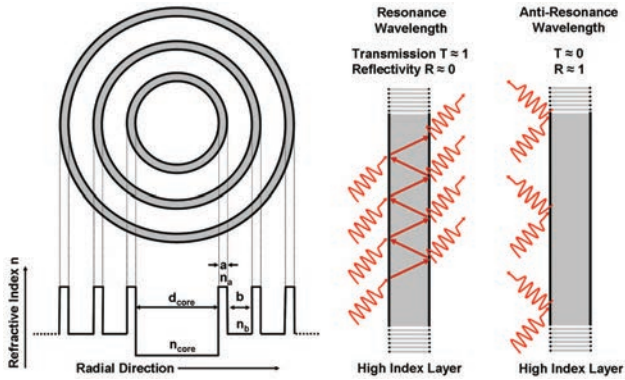

Figure 2.7: Scheme of the refractive index profile of a Bragg fiber (left) and guiding mechanism in the ARROW picture (right).

2.6.3.2 Photonic Crystal Fibers

A very active field of research concentrates on photonic crystal fibers (PCFs) which are formed by a periodic crystal lattice of air holes [31, 37]. Some fiber end faces of such PCFs are exemplarily shown in figure 2.8. The core region is simply formed by removing one or several holes. In other words, as a defect of the crystal, which forms a region where light can propagate. The crystal lattice is described by the hole size d and the pitch (hole center to hole center distance) Λ. Most of these structures are based on TIR because the air holes effectively reduce the refractive index of the cladding, thus the core has a higher refractive index. However, a special class of such microstructured fibers use a photonic bandgap. Within these fibers, light of certain wavelengths is not allowed (by Maxwell equations) to propagate which traps the light in the defect region forming the core. The refractive index of the core in such fibers is usually reduced to compensate for the reduction of the refractive index by the air holes in the cladding.

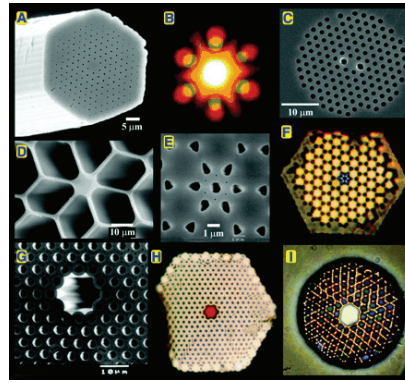

Figure 2.8: Cross-sections of various types of photonic crystal fibers taken from a review article of P. Russell [31].

2.6.3.3 Hollow-Core Fibers

Because of the low nonlinearity of air, hollow-core optical fibers are particularly interesting for high-power applications even for the delivery of ultra short laser pulses. Due to the negligible dispersion of air, the total dispersion is dominated by the dispersion of the waveguide and can therefore be tailored within a large regime. Hollow PCFs offer the possibility to transport laser beams in the near infrared. More than 95% of the power are transported in air and a low bending sensitivity can be achieved at small mode field areas [38]. A very high air fraction in the fiber cladding, which leaves only very small silica support bridges, is necessary to obtain such properties. However, the attenuation of these fibers is very high compared to their solid-core counterparts. The losses of commercially available fibers are in the range of 0.1 dB/m (e.g., NKT Photonics HC-1060-02). The high losses and the extremely fragile structure, which makes the production difficult and the handling problematic, has prevented industrial applications of such fibers until now.

Hollow-core BFs require a high-index contrast in the microstructured region. Therefore, special material combinations have to be used. In addition to their optical properties (high refractive index contrast, low absorption, and high purity), these materials have to fulfill certain thermo-mechanical constraints in order to be drawn

together to an optical fiber. Hollow-core BFs have only been demonstrated in the 10 µm wavelength regime using As_2Se_3 ($n \approx 2.8$) and a low-index polymer "PES" ($n \approx 1.55$) [39]; and around $\lambda = 1\,\mu m$ with an air-silica BF [40]. In this fiber, the low-index layers were formed by air which results in a structure similar to the hollow-core PCF.

2.6.4 Leakage Channel Fibers

Another type of microstructured fiber, looking like a simplified version of a solid core PCF, is the *leakage channel fiber* (LCF) [41, 42]. A LCF may be considered as a special version of PCF in which the holes surrounding the core have the function of a sieve. The concept is only based on loss management. The HOMs leaking through the microstructured region may be much lossier than the fundamental mode.
A photonic bandgap is not responsible for guiding the light, but a disturbed index guiding mechanism. Usually, such fibers are made from the same material for cladding and core, but there are some low-index inclusions around the core (figure 2.9). There is a large refractive index step between the core and the low-index inclusions and no index step between the core and the region between these inclusions which causes lossy channels for all modes. Due to the large refractive index step, and ease of fabrication, air holes are considered as low-index inclusions in the following. The same parameters as for the PCFs are used to describe the structure (hole diameter d, pitch Λ). However, it would be more illustrative to use the bridge width $w_b = \Lambda - d$ to describe the structure of the fiber.

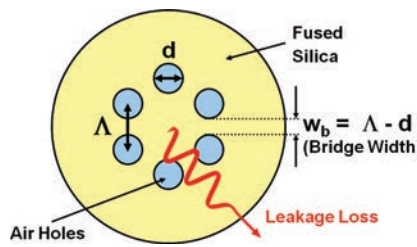

Figure 2.9: Scheme of a leakage channel fiber. A leakage channel fiber consists of a fiber core surrounded by low-index inclusions such as air holes.

2.7 Fiber Production

Optical fibers are produced from a preform with a fiber drawing tower. Basically, the preform is a short and transversally enlarged version of the future fiber. Since the material volume is preserved, the drawing process makes a long piece of thin fiber from a short but thick bulk preform. The preform can be made by deposition of different glasses, for instance, by a *modified chemical vapor deposition* (MCVD) or by assembling different glass rods or tubes. The latter is called *stack-and-draw* method and is commonly used to produce photonic crystal and multicore preforms. The LCF preforms used for this work were manufactured by ultrasonic drilling of pure fused silica rods. The preform, mounted at the upper stage of the drawing tower, is melted with a furnace at a specific drawing temperature (typically between 1800°C -2000°C). After passing through the furnace the liquid glass is rapidly cooled down and wheels are used to pull the solidified glass.

By optimizing the parameters of drawing tension, temperature, and preform velocity (speed with which the preform is introduced into the furnace), a stable drawing process leading to the desired fiber diameter can be achieved. If the preform contains air holes, the geometrical properties of the drawn fiber depend also on the gas pressure applied to the holes. Finally, the fiber is fed trough one or two coating applicators. The coating prevents the otherwise brittle fiber from braking. Finally, the fiber is coiled up with a capstan at the ground level of the drawing-tower.

The IFSW uses a modified Nextrom OFC20 drawing tower. It can handle preforms with diameters from 15 to 50 mm and it can draw fibers to diameters ranging from 90 to 720 µm. It offers the possibility to apply a controlled gas pressure which is, for example, used for the drawing of LCFs. The drawing tower is 9.5 m high and comprises 3 stages. The upper stage shown in figure 2.10a) is used for the preform mount and the furnace. The preform is fed into the furnace and heated. The glowing glass melt inside the furnace illuminates the preform. The bright light visible in the picture is caused by scattering at the interface between the actual preform and a cheaper glass handle used for handling the preform.

A fiber leaving a coating applicator is shown in picture b) and a piece of a LCF preform in picture c). The coating is cured by UV-lamps which results in a green glow. The IFSW drawing-tower includes two coating applicators which makes it possible to use a soft inner coating, to reduce the influence of micro-bending, and

a hard outer coating which gives mechanical strength to the fiber to reduce macrobending losses.

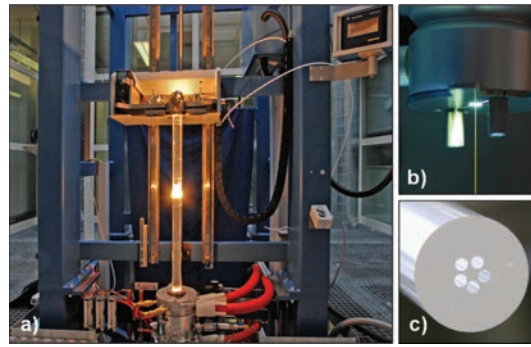

Figure 2.10: Pictures of the upper stage of the IFSW drawing tower a), a fiber during coating application b), and a LCF preform with 2.5 cm diameter c) [43].

Chapter 3

Simulation Methods

Based on the knowledge of the theoretical background presented in chapter 2, simulation tools were adapted and used to evaluate the specialty fiber concepts described in section 2.6 with the focus on transport of high-power laser beams with diffraction-limited or near diffraction-limited beam quality.
The present chapter describes the methods used for the simulation of the fiber properties such as the mode structure, the overall losses, or the bending sensitivity.

3.1 Eigenvalue Problems

The electromagnetic field of radiation propagating in a fiber can be described by wave equations of either the electric or the magnetic field. Since most materials are non-magnetic and the magnetic field is continuous within such materials, it is advantageous to choose the magnetic field to work with. The wave equation for the magnetic field $\vec{H}$ can be derived analogous to the wave equation 2.22 for the electric field $\vec{E}$ as described in section 2.2.1.

By applying $\nabla\times$ to 2.13 and using $\vec{J}=0$ one obtains

$$\nabla\times\left(\nabla\times\vec{H}\right) = \nabla\times\frac{\partial\vec{D}}{\partial t}\,,\ \text{with}\ 2.15 \tag{3.1}$$

$$\nabla\times\left(\nabla\times\vec{H}\right) = \nabla\times\left(\frac{\partial}{\partial t}\left(\epsilon_0\vec{E}+\vec{P}\right)\right)\,,\ \text{with}\ 2.26 \tag{3.2}$$

$$\nabla\times\left(\nabla\times\vec{H}\right) = \nabla\times\left(\epsilon_0\left(1+\chi^{(1)}\right)\frac{\partial}{\partial t}\vec{E}\right)\,,\ \text{with}\ \epsilon=1+\chi^{(1)} \tag{3.3}$$

$$\nabla\times\left(\nabla\times\vec{H}\right) = \nabla\times\left(\epsilon_0\epsilon\frac{\partial}{\partial t}\vec{E}\right)\,,\ \text{with}\ 2.14 \tag{3.4}$$

$$\nabla\times\left(\nabla\times\vec{H}\right) = -\epsilon_0\mu_0\epsilon\frac{\partial^2}{\partial t^2}\vec{H}\,,\ \text{with}\ \mu_0\epsilon_0=1/\mathrm{c}^2\ \text{and}\ \epsilon=\mathrm{n}^2 \tag{3.5}$$

$$\nabla\times\left(\nabla\times\vec{H}\right) = -\frac{n^2}{c^2}\frac{\partial^2}{\partial t^2}\vec{H}\,. \tag{3.6}$$

As calculated in 2.48 and 2.49 the nonlinear part of the refractive index is negligible ($n_2 I << n_{co}-n_{cl}$) for the experimental conditions considered in this work and the linear approximation 2.26 can be used. However, the weakly guiding approximation 2.40 used for step index silica fibers (with only low refractive index differences between core and cladding) is not applied in this case because specialty fibers are investigated. With Cartesian coordinates, as typically used in finite element calculations, and time-harmonic fields, the magnetic field $\vec{H}$ of a wave propagating inside the waveguide can be expressed as

$$\vec{H}(x,y,z,t)=\vec{H}(x,y,z)e^{i\omega t}\,. \tag{3.7}$$

With this ansatz-function and $\omega=ck_0$, equation 3.6 can be written in the form which is implemented in the software used for the simulations [44].

$$\nabla\times\left(n^{-1}\nabla\times\vec{H}\right)-k_0^2\vec{H}=0 \tag{3.8}$$

Equation 3.8 is a vector differential Helmholtz equation. For anisotropic materials the relative electric permittivity ϵ (and possibly the relative magnetic permeability μ which is usually close to 1 for optical materials) and hence the refractive index are tensors. After taking into account the boundary conditions, the software reformulates this equation into a generalized eigenvalue equation of the form of

$$A\phi-\lambda_n B\phi_n=0 \tag{3.9}$$

where A and B are system matrices. The interested reader is referred to [45] for more details. The system is solved for N eigenvalues λ_n (generalized eigenvalues

of A and B) with $n = 1..N$ which make the determinant $A - \lambda_n B$ vanish. The propagation constant β or the effective refractive index $n_{\text{eff}} = \beta\lambda/(2\pi)$ of a mode can be specified as the eigenvalue of the calculation. For the calculation of losses, the eigenvalue equation 3.9 has to be solved for complex values. Once the effective index n_{eff} of the mode is found, the losses α in dB/m are calculated from the imaginary part of n_{eff} by

$$\alpha = 2\pi \cdot \frac{20}{\ln 10} \cdot \frac{\text{Im}(n_{\text{eff}})}{\lambda_0} \text{dB}\,. \tag{3.10}$$

In the following, the described eigenvalue problem is solved using the commercial software COMSOL Multiphysics which is based on the finite-element method.

3.2 Finite Element Calculations with COMSOL Multiphysics

The goal of this section is to introduce the methods used for simulations of optical fibers to the interested reader. An overview on how such simulations are structured is given and experienced reader will notice which parts are especially important for the calculation of fiber modes. Because the focus of this work are the results of the simulations and the experiments, the readers are referred to the handbook of COMSOL Multiphysics [44] for further details to repeat the simulations.

The finite-element method (FEM) is a numerical method used to solve differential equations. A domain is divided into a finite number of small elements on which ansatz-functions are defined. The differential equations can then be solved for each element using a functional Ritz or a residual Galerkin method [46]. The FEM was first proposed in the 1940s and was applied to structural aircraft design in the 1950s. Since then it was increasingly applied to other fields. For the electromagnetic modeling, the invention of so called vector or Nedelec elements [45] was important to overcome problems such as the occurrence of non-physical ("spurious") modes, difficulties with conducting and dielectric edges and corners due to field singularities, and the many boundary conditions to be applied to interfaces and surfaces.

The commercial software COMSOL Multiphysics can be used to define arbitrary geometries and couple different physical problems such as the calculation of electromagnetic eigenmodes and the application of mechanical stress.

The basic steps of simulating with COMSOL Multiphysics are

- Definition of the type of problem (e.g., electromagnetism, hybrid-modes, ...)
- Definition of global parameters (e.g., coordinates, wavelength, ..)
- Implementation/drawing of geometrical objects (domains and subdomains)
- Definition of the type of interface between the domains
- Definition of boundary conditions
- Selection of interpolation functions (first (linear), second (quadratic) or higher-order polynomials)
- Selection of an appropriate solver, definition of solver settings, and starting values
- Discretization or subdivision of the domains (meshing) with a fine mesh of lines/triangles/tetrahedra (node or vector elements), description of a node containing coordinate values, local number (pos. in the element), global number (pos. in entire system)
- Formulation of the system of equations (Ritz-Galerkin method)
- Solving of the system of equations and calculating desired parameters
- Postprocessing

In this work this procedure is applied to optical fibers. Since the fiber modes in an ideal (straight) fiber do not change during propagation along the fiber axis, the modes can be calculated with a single 2-dimensional (2D) fiber cross-section. The simulation of bent fibers will be described in section 3.2.2. The COMSOL "RF-Module" (radio frequency module) is used with space dimension 2D. Because the light within the fiber is traveling perpendicular to this plane, the "Mode Analysis" of "Hybird-Mode Waves" in the "Perpendicular Waves" folder is selected. This tells COMSOL that a wave, of the form of equation 3.7, propagates in the z direction and that the Helmholtz equation 3.8 has to be solved for the eigenvalue.
Then, the global parameters (e.g., wavelength, bending radius,..) are given, the fiber cross-section is drawn, material properties (refractive indices) are defined, and

a "Continuity"$((\vec{n} \times \vec{H})\vec{H} = 0; (\vec{n} \times \vec{E})\vec{E} = 0)$ interface condition is used between the different domains.

The fiber is usually surrounded by a perfectly matched layer, which will be explained in the following section, to calculate the losses. The total domain of the simulation is enclosed with a "Perfect Electric Conductor" (PEC) $(\vec{n} \times \vec{E} = 0)$ boundary condition. Hybrid elements are used to represent the interpolation functions $(shcurl(2,'Hx','Hy')shlag(2,'hz')$ for such an element of order 2 (quadratic) in the COMSOL notation). They consist of conventional node-based interpolation functions for the longitudinal and edge-based vector functions for the transverse components of the field vectors.

Spurious modes were observed when solving such equations with the use of first-order vector elements even with a fine mesh. The use of second-order mesh elements eliminated these unphysical solutions. Most of the time, the "SPOOLES" solver, which takes advantage of symmetric and Hermitian systems was used because it is more memory efficient than the fast default "UMFPACK" solver. COMSOL then formulates the system of equations and solves it according to the settings of the solver. Most of the calculations presented in this thesis were formulated as such an eigenvalue problem.

3.2.1 Using and Optimizing Perfectly Matched Layers

Considering lossy waveguides (e.g., LCFs, BFs, bent fibers,..) leads to the problem that light will be able to escape the fiber core and couple to cladding or radiation modes. The problem is an open boundary problem because there is no natural boundary around the fiber. To treat this open boundary problem within a finite computational domain (the size of the simulated region (e.g., in μm^2) is limited by the random access memory (RAM) of the used hardware), an artificial absorbing layer can be implemented. The aforementioned PEC $(\vec{n} \times \vec{E} = 0)$ boundary condition could be used to truncate the simulated region, but this leads to unwanted artificial reflections at the interface and even total reflection depending on the angle of incidence of the electromagnetic wave.

Introducing a perfectly matched layer (PML) [47] between the fiber and the PEC can strongly reduce this reflection. The easiest way to understand the purpose of an PML is to think about it as an artificial anisotropic absorbing material [48]. An equivalent but more general approach is the so-called stretched coordinate PML

[49]. It is based on a coordinate transformation in which one or more coordinates are mapped into complex numbers. As a result, oscillating (propagating) waves are replaced by exponentially decaying waves.

To take advantage of the cylindrical shape of optical fibers within the framework of the Cartesian basis (x, y, z) of the FEM solver, new coordinate functions defined as

$$r = \sqrt{x^2 + y^2} \text{ and} \tag{3.11}$$

$$\phi = (\text{sign(y)} + 1 - |\text{sign(y)}|) \cdot \arccos \frac{x}{r} \tag{3.12}$$

were implemented for the simulations in this work. To achieve the attenuation of a wave propagating with a non-zero radial component inside the PML, the radial coordinate r is transformed to [45]

$$\tilde{r} = \int_0^{r'} s_r(r) dr \tag{3.13}$$

where s_r is the radial stretching coordinate. For the simulations, a circular PML with the thickness d_{PML} was considered at a distance of r_{PML} from the center of the fiber (usually the center of symmetry). Therefore, the radial stretching variable s_r can be written as [45]

$$s_r = \begin{cases} 1 & : \quad \text{for } r \leq r_{\text{PML}} \\ s_{rr} - i s_{ri} \left(\frac{r - r_{\text{PML}}}{d_{\text{PML}}} \right)^2 & : \quad \text{for } r > r_{\text{PML}} \end{cases} . \tag{3.14}$$

The real part s_{rr} of s_r, which attenuates evanescent waves if $s_{rr} \geq 1$, is set to 1. The damping constant s_{ri} is optimized to attenuate outward propagating waves. The stretching variable s_r has to be defined at the border between the PML and the actual (physical) region of interest, but it does not matter at which part of equation 3.14 the equal sign is introduced ($r \leq r_{\text{PML}}$ or $r \geq r_{\text{PML}}$).

In theory, this leads to a reflectionless damping of outward propagating waves, but the discretization of the FEM leads to "numerical reflections". Using a thicker PML region reduces this numerical reflections but increases the calculation time and memory consumption of the simulation. Various simulations with different thicknesses d_{PML} were carried out. It was found that stable and reliable results are obtained with a PML thickness of $d_{\text{PML}} = 10\,\mu\text{m}$. Therefore, for further calculations d_{PML} was always set to $10\,\mu\text{m}$.

To show the influence of the damping constant s_{ri}, the results of a series of simulations of a straight Bragg fiber are shown in figure 3.1. The obtained losses depend

on the damping constant s_{ri}. For $s_{ri} = 3$ the curve has an absolute maximum because at this value the numerical reflections are minimized (for a PML with 10 µm thickness) which leads to the optimal value of s_{ri} used for further simulations. However, this value should be optimized for every simulation individually. As mentioned

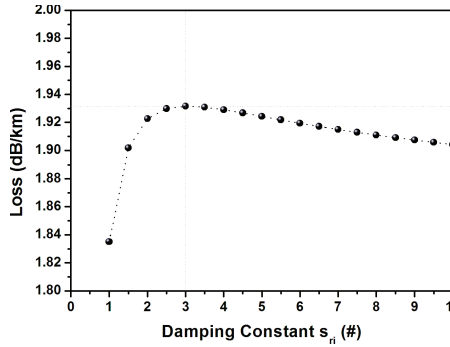

Figure 3.1: Effect of the variation of the damping constant s_{ri} on the calculated losses for a 10 µm thick perfectly matched layer.

earlier, another way of understanding the PML is to think about it as an absorbing material. It is possible to hide the coordinate transformation into material-like properties of the PML region. The permittivity ϵ and the permeability μ of the PML are modified to

$$\mu = \mu_0 \mu_r \hat{T} \tag{3.15}$$

$$\epsilon = \epsilon_0 \epsilon_r \hat{T} \tag{3.16}$$

with a transformation matrix $\hat{T}^{cy}$ [45] given by the radial stretching variable s_r

$$\hat{T}^{cy} = \begin{pmatrix} 1/s_r & 0 & 0 \\ 0 & s_r & 0 \\ 0 & 0 & s_r \end{pmatrix} \tag{3.17}$$

which is expressed in a cylindrical coordinate (r, ϕ, z) system. This tensor has to be transformed to the Cartesian coordinate system of the FEM-simulation by

$$\hat{T} = \hat{R} \hat{T}^{cy} \hat{R}^{-1} \tag{3.18}$$

with the transformation matrix $\hat{R}$

$$\hat{R} = \begin{pmatrix} \cos(\phi) & -r\sin(\phi) & 0 \\ \sin(\phi) & r\cos(\phi) & 0 \\ 0 & 0 & 1 \end{pmatrix} . \tag{3.19}$$

The matrix $\hat{T}$ in the Cartesian basis can be written as

$$\hat{T} = \begin{pmatrix} \frac{1}{s_r}\cos^2\phi + s_r\sin^2\phi & \cos\phi\sin\phi\left(\frac{1}{s_r} - s_r\right) & 0 \\ \cos\phi\sin\phi\left(\frac{1}{s_r} - s_r\right) & \frac{1}{s_r}\sin^2\phi + s_r\cos^2\phi & 0 \\ 0 & 0 & s_r \end{pmatrix} \tag{3.20}$$

which can be implemented in the geometrical subdomains of the simulation.
With these coordinate transformations, the fields and the full vector wave equations can still be written in the form of the equations 3.7 and 3.8. Therefore, the available Maxwell-solvers can be applied without any changes which represents a great advantage.

3.2.1.1 Benchmarking Different Perfectly Matched Layers

To find a suitable PML representation for the simulations performed within this work, several PML concepts were compared. Figure 3.2 shows the examples of a rectangular and a circular PML surrounding a Bragg fiber implemented as an additional domain within the simulation.
The different PML concepts were tested by implementing and replacing one after the other within the same model. A simulation of a BF with four high refractive index layers in the cladding was chosen as a benchmark ($\lambda = 1\,\mu m$, $r_{co} = 12.5\,\mu m$, $a = 1\,\mu m$, $b = 4\,\mu m$, $n_{co} = n_b = 1.45$, $n_a = 1.47$).

Type	$\mathrm{Re}(n_{\mathrm{eff}})$	$\mathrm{Im}(n_{\mathrm{eff}}) \cdot 10^{12}$	Loss $\frac{dB}{km}$
Rectangular PML according to [49]	1.4499069322000	1.025612	0.052311
1. Circular PML according to [50]	1.4499069321385	0.1492794	0.007614
2. Circular PML pre-installed in Comsol 3.3	1.4499069321350	0.6978973	0.035596
3. Circular PML according to [44]	1.4499069322678	1.287712	0.065680
Analytical TMM	1.4499069322960	1.368332	0.069792

Table 3.1: Comparison of the results of different PML implementations to an analytical solution.

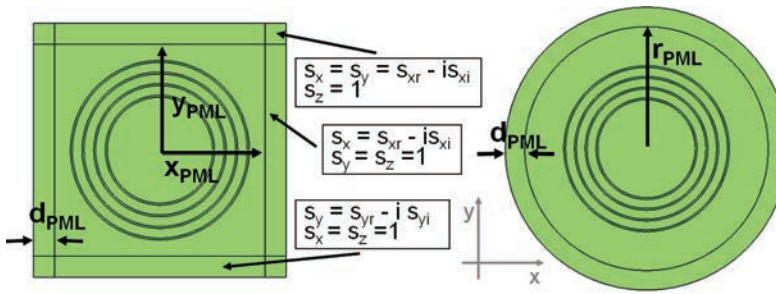

Figure 3.2: Scheme of a rectangular and a circular PML with thickness d_{PML} surrounding a Bragg fiber. Different damping constants (S_{xi},S_{xi}) along the Cartesian coordinates can be implemented in the rectangular PML.

Table 3.1 shows the calculated losses of the fundamental mode using the different PMLs. The FEM results are compared to the result of a calculation with a transfer matrix method (TMM) [30]. The TMM treats layered media by a system matrix which is used to calculate the reflection and transmission of an initial field. Therefore, it is commonly used for the design of plane dielectric multilayer coatings or in this case for the calculation of modes in cylindrically symmetric Bragg fibers.
All PML concepts result in lower confinement losses compared to the TMM result. This can be explained by unwanted reflections in the PML. The three circular PML implementations were all much faster (in this case by more than one order of magnitude) in terms of calculation time than the rectangular PML which was introduced earlier by Chew and Weedon [49]. The PML which is already implemented in Comsol Multiphysics 3.3 was fast, but the possibilities for optimizing this PML are limited. In many calculations this PML gave loss values which were roughly a factor of two lower than the values given by the TMM. The 3. circular PML was defined according to the *COMSOL Multiphysics Electromagnetics Module User's Guide* [44] and should be similar to the one already implemented in the COMSOL 3.3 software, but in contrast to this PML the user defined version can be optimized by a variation of the damping constant s_{ri} as shown in the previous section. Because of that, the values of real and imaginary part (and hence the losses) obtained with the 3. circular PML concept are close to the values obtained with the TMM.

Figure 3.3 shows the calculated bending losses of the same fiber using the three circular PML techniques. The simulations using the Comsol PML (black diamonds) resulted in a peak at a bending radius of $R = 20\,\mathrm{cm}$. The PML used by Viale *et al.* [50] (red circles) exhibited a kink at $R = 10\,\mathrm{cm}$. Such artifacts were observed for other fibers as well even in the simulations of step index fibers.
The best performance was achieved with the 3. circular PML (blue spheres) defined according to [44]. The results obtained with this PML show a smooth and continuous increase of the bending losses with decreasing bending radius R. The mesh used for the simulations was the same for all the calculations.
As a result of this benchmark, the PML already implemented in the software was utilized for basic investigations of the specialty fibers because it is fast and convenient to use. For more accurate results, the 3. circular PML concept was used in further analyses.

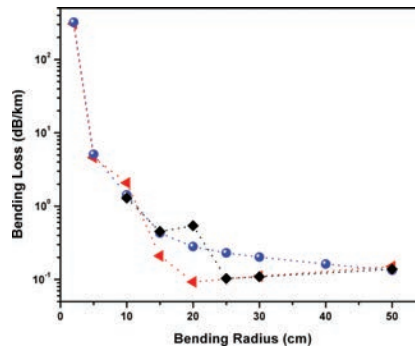

Figure 3.3: Calculation of the bending losses of a BF to compare the performance of different PML techniques. The results obtained with the PML according to [50] are indicated by red rectangles, the Comsol Multiphysics 3.3 PML by black diamonds, and results obtained with the PML defined according to [44] are indicated by blue spheres.

3.2.2 Modeling of Bending Losses

With the help of the PML concept it is possible to efficiently calculate losses. As a next step, fiber bends are taken into account. An eigenmode of a fiber does not change its shape or propagation constant during its propagation along the fiber as long as there are no perturbations as introduced by fiber bends.
However, if the bend has a constant curvature, the eigenmodes of the bent fiber do not change along the propagation of the bent section which means that the eigenmodes can be calculated again with just one 2D slice of the fiber. If the curvature is not constant, the problem can be divided into several parts with piecewise constant curvature.
The bend (or curvature) can be taken into account by the *equivalent index model* [51, 52, 53] which is described in the following.

3.2.2.1 The Equivalent Index Model for Bent Fibers

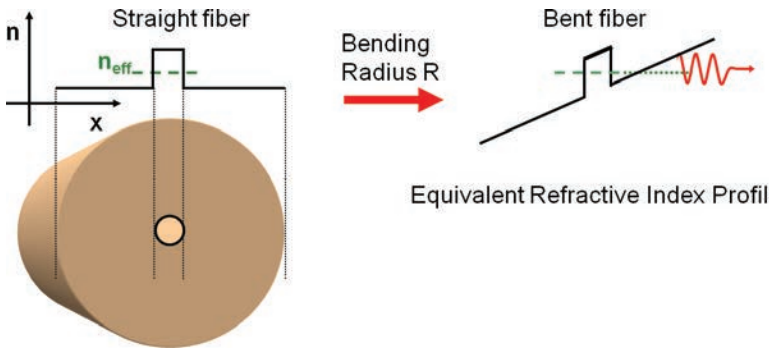

Figure 3.4: Principle of the equivalent index model used to simulate bent waveguides in a 2D-environment. The distribution of the refractive index of a straight waveguide is transformed to take into account the curvature.

From an electromagnetic point of view it is possible to calculate the radiation losses of a bent fiber in a 2D model without any approximations. D. M. Shyroki derived modified expressions for the permittivity ϵ and the permeability μ from first-principles [53] to replace the ones of the straight waveguide. Because the modifica-

tion of the transverse components (μ_{xx}, μ_{yy}, ϵ_{xx}, ϵ_{yy}) and the longitudinal components (μ_{zz}, ϵ_{zz}) are different, the modified permittivity $\hat{\epsilon}_r$ and permeability $\hat{\mu}_r$ have to be written in a tensor form even for isotropic materials.
However, for all structures and bending radii of interest for this work, the influence of the z-components is negligible [53]. Therefore, the tensors can be reduced again which results in the well known Marcuse formula [51, 52]

$$n_R = n \cdot \sqrt{1 + 2\frac{x}{R}} \tag{3.21}$$

where n_R is the new equivalent refractive index of the bent fiber, n is the refractive index of the material, and R denotes the bending radius along the x-coordinate x.
This equation can be modified to take into account the bend-induced change of the refractive index of the material which can be described in terms of an effective bend radius R_{eff} to represent the stress-optical effect [54]. In a first-order approximation, the refractive index change can be written as

$$n_R = n \cdot \sqrt{1 + 2\frac{x}{R_{\text{eff}}}} \approx n\left(\frac{x}{R_{\text{eff}}}\right) , \tag{3.22}$$

with $R_{\text{eff}} = 1.28 \cdot R$ for silica fibers [54]. Within this model the refractive index profile of a bent fiber can be drawn as a tilted version of the refractive index profile of the straight fiber as indicated by figure 3.4.

3.2.2.2 Modes in Bent Fibers

As described above, a bent fiber is equivalent to a straight fiber with a modified refractive index as stated by the equivalent index model. Therefore, 2D-eigenmode simulations can be used even for bent waveguides, but the modified index has an impact on the mode structure of the fiber.
In general, the modes of a straight fiber are deformed by a bend in a way that their fields are shifted towards the higher refractive index which corresponds to the opposite side of the center of the curvature. Figure 3.5 shows the calculated lowest-order modes of an ideal SIF with a NA of 0.06 and a core diameter of 30 µm. If the fiber is kept perfectly straight, 4 core-guided LP-modes (see chapter 2.2.2 for the classification) are supported. The modes can be classified in terms of HE-modes as well, giving more information about the polarization in case of the degenerated modes. However, if the fiber is bent, even slightly, the mode structure changes. If

a curvature of $R = 0.2\,\mathrm{m}$ is simulated with the help of the equivalent index model, only linearly polarized modes are found in the results. Hence, it is less meaningful to use the HE-classification scheme. Azimuthally or radially polarized ring-shaped modes do not appear in bent step index fibers according to the simulation result.
An experimental investigation of this effect is described in chapter 7. In case of $\mathrm{LP_{0X}}$-modes, the bend shifts the center of gravity of the mode and deforms the mode shape. The more the fiber is bent, the larger is the shift and the deformation [55]. In case of the $\mathrm{LP_{X1}}$-modes, the ring-like shape of the field distribution is lost due to the bend.
Another feature already visible in this figure is that less well guided modes can be attenuated by bending the fiber. The $\mathrm{LP_{02}}$-mode, well guided in case of the straight fiber, becomes lossy if the fiber is bent. A large part of the mode field penetrates into the cladding causing high losses. As implied by the different field distributions of the two $\mathrm{LP_{02}}$-modes, the losses may significantly become polarization dependent close to a critical value of the bending radius. In the case discussed here, the fiber is bent in the x-z-plane and the resulting losses of the x-polarized mode are 19 dB/m, whereas the losses of the y-polarized mode are 241 dB/m according to the simulation.

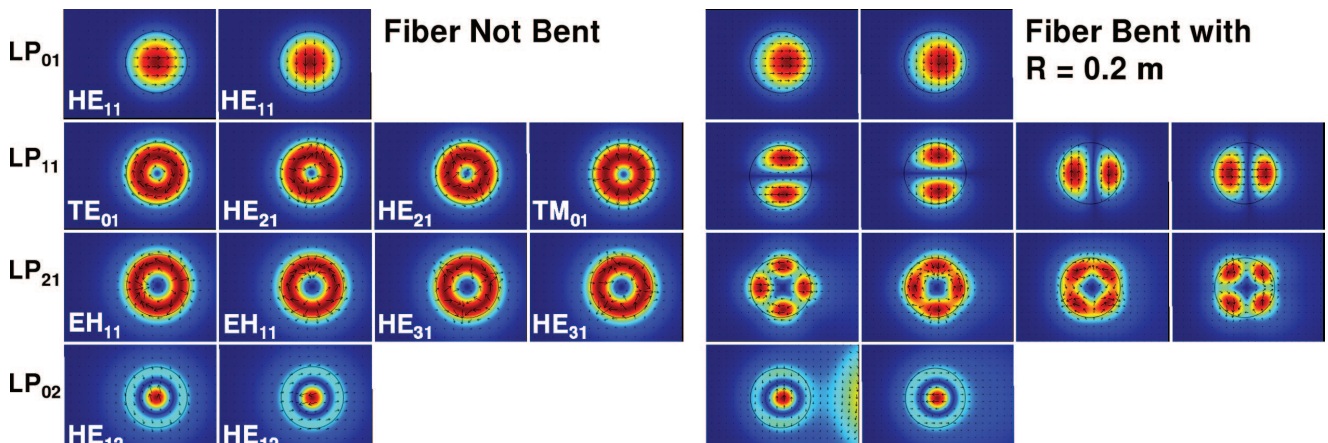

Figure 3.5: Calculated field distributions of the lowest-order modes of a step index fiber with 30 µm core diameter and NA = 0.06. If the fiber is bent ($R = 0.2\,\mathrm{m}$), only linear polarized LP-modes are obtained.

3.2.3 Customizing the Simulation

As discussed above, fiber bends can easily be simulated with the help of the equivalent index model and losses are obtained with the help of perfectly matched layers. Furthermore, complicated fiber cross-sections can be drawn with computer-aided design (CAD) tools. However, for the convenience of numerical modeling,more variables and equations have to be implemented to avoid starting a new calculation each time a parameter (e.g., wavelength, bending radius,..) is changed.
The refractive indices depend on the wavelength at which the modes are calculated and have to be changed as well if the wavelength is changed. Another aspect of improving the simulation is to reduce the effort of the data analysis, for instance, by directly implementing integrals over the resulting mode fields to obtain a value for the effective mode area for each calculated mode. In the following it is described how such features are implemented in the FEM software.
Values for the wavelength, NA, refractive indices, bending radius, PML-parameters, and many other parameters can easily be defined in the "Constants" menu. It is possible to enter equations as a definition for constants depending on other constants and parameters but not on coordinates. For example, a Sellenmeier equation for the wavelength dependence of the refractive index of pure silica [56]

$$\begin{aligned} n_{silica}(\lambda) = (1 + 0.6961663 \cdot (\lambda \cdot 10^6)^2/((\lambda \cdot 10^6)^2 - 0.0684043^2) \\ +0.4079426 \cdot (\lambda \cdot 10^6)^2/((\lambda \cdot 10^6)^2 - 0.1162414^2) \\ +0.8974794 \cdot (\lambda \cdot 10^6)^2/((\lambda \cdot 10^6)^2 - 9.896161^2))^{1/2}\,. \end{aligned} \tag{3.23}$$

Note that in order to make the simulation work with the specified constants some definitions in the program have to be modified accordingly. In particular, the frequency in the "Application Scalar Variables" tab has to be defined as c/λ if the wavelength is defined as λ in the constants menu.
Functions of coordinates or simulation results such as equation 3.10 can be defined in the "Global Expressions" menu. Suitable cylindrical coordinates r (3.11) and ϕ (3.12), to define a cylindrical PML or a radially symmetric stress distribution, are implemented as "Global Expressions". In the "Subdomain Expressions" menu, special expressions or constants can be defined for each geometrical domain individually which can be helpful in many applications.
If integrals should be calculated, as needed for the calculation of the mode field area (2.41), the "Integration Coupling Variables" in the "Subdomain Variables" tab are

the correct place to implement them. The results of the integrals can then be used as an input for the "Global Expressions" to calculate quantities which include these integrals.
It is often desirable to know results for a whole wavelength range or the bending losses for different radii without calculating each value by changing the parameters manually. With the COMSOL Multipyhsics version 3.3a, a submenu "Parametric Sweep" was added to the "Solve" menu, which can easily be used to automatize calculations depending on non-structural parameters. Before the version 3.3 of COMSOL Multiphysics, Matlab had to be utilized. To change structural parameters Matlab is still a practical tool to use with the later versions of COMSOL Multiphysics.

3.2.4 Matlab Interface

The COMSOL Multiphysics software can be connected to Matlab, a commercial programming language, especially to solve mathematical problems. Thus, parametrical sweeps can be programmed. Furthermore, it can be useful to program an interface in which structural parameters like radii and layer thicknesses can be directly entered instead of drawing the fiber structure in the COMSOL interface to performed structural changes faster.
Matlab was used as a standalone program as well. A Matlab based software tool [57] was adapted and used to calculate modes and losses of BFs in addition to the FEM. The tool uses a transfer matrix method (TMM) [30] which allows the calculation of modes for straight and circular symmetric fibers.

Chapter 4

Experimental Methods

In this chapter, the experimental methods used to characterize optical fibers are explained and details of the experimental settings are given. First, the preparation of the fibers for these measurements is described.

4.1 Fiber Handling

A fiber has to be carefully prepared before it can be characterized in order to obtain reliable results. The fiber end faces have to be clean and flat. Therefore, the fiber is stripped, which means the coating is removed from the fiber ends, either by heat (a flame or hot air blower), by a mechanical fiber stripping tool, or by using acetone to dissolve the polymer from the glass. The bare fiber is then cleaned with alcohol and within this work cleaved with a *Vytran LDC-200* automated fiber cleaver.
Figure 4.1 shows the functional part of this machine. In the case of all-solid fibers, mainly the outer diameter determines the cleave parameters. However, the cleave parameters have to be optimized for each fiber individually especially for fibers containing air holes. The prepared fiber ends can then be placed on multi-axis nano-positioning systems to couple light in and out of the fiber.

4.1.1 Mode Stripping

Since the overlap of the free space mode and the fiber mode is never exactly 100% and because of imperfect coupling conditions (imperfect optics, alignment errors) some light will not be transferred to the fundamental mode of the fiber and may excite cladding modes. This light may affect the measurements and has to be removed.

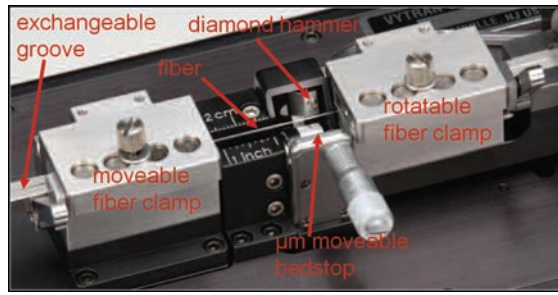

Figure 4.1: Functional part of the Vytran LDC-200 automated fiber cleaver.

If the fiber coating is of higher refractive index than the cladding, the situation is relaxed because light will not be guided in the cladding. For low-power investigations it is enough to use (Scotch) tape to fix the fiber ends onto the experimental setup which at the same time works as a cladding mode stripper. Mode matching liquid (i.e. glycerin) can be used but it has certain drawbacks. Since it is liquid the wetting of the fiber changes with time and because glycerin is hygroscopic it reacts with the humidity of the air which changes the refractive index. Both leads to unstable experimental conditions. For high-power experiments the fiber cladding can be etched with glass etching liquid to generate a rough surface which scatters the light out of the cladding.
Fibers with a low-index coating (e.g., silicon) are more problematic because it leads to TIR in the cladding. In addition to the use of scotch tape and etching to strip the cladding modes, they can be separated from the core-guided light after the fiber by selecting the NA of the core-guided modes. Another possibility is to image the fiber end face and to use a suitable aperture to discard the light coming out of the cladding.

4.1.2 Applying Bends to Optical Fibers

Usually, experimental conditions require straight fiber ends, but the fiber is arranged on an optical table and coiled with a large radius to fit the several tens of meters in the lab. This leads to many different fiber sections with different radii of curvature. Besides the intentionally defined bends to investigate the bending losses, these radii

should be as large and smooth as possible in order to minimize their influence on the measurement result. If such care is taken, the output power can be measured as a reference for a "straight" fiber $P_{out}(R \to \infty)$ and the bending losses α_R caused by a single loop with radius R can be obtained by

$$\alpha_R = \frac{10\log(\frac{P_{out}(R)}{P_{out}(R\to\infty)})}{2\pi R}\text{dB} \tag{4.1}$$

where $P_{out}(R)$ is the measured output power.

If a certain bending radius R is investigated, the transition from the straight (or large radius) part of the fiber to the curvature under examination is crucial because the modes are different in those regions and mode matching losses may arise (see chapter 2.3.1). To avoid these mode matching losses all the transitions have to be smooth, which implies, that a large part of the fiber in the setup has to be slightly moved for each new radius investigated. This is a factor which reduces the reproducibility of the measurement.

Additional problems occur for fibers with small cladding diameters (e.g., 125 µm) especially with silicon coating. The adhesion of the fiber to the table makes it more difficult to achieve smooth transitions of the bending radii. For larger diameters (>250 µm), lifting the fiber slightly is sufficient to avoid kinks because of the stiffness of the fiber.

The bending radius can be controlled by wrapping the fiber on mandrels with specified radii or by using free loops. The results depend on the way the bend is applied. Figure 4.2 shows 3 different methods. If the incoming fiber is oriented tangentially to the mandrel (method 1) higher losses occur compared to the other methods. Due to the abrupt change of the bending radius, method 1 leads to mode matching

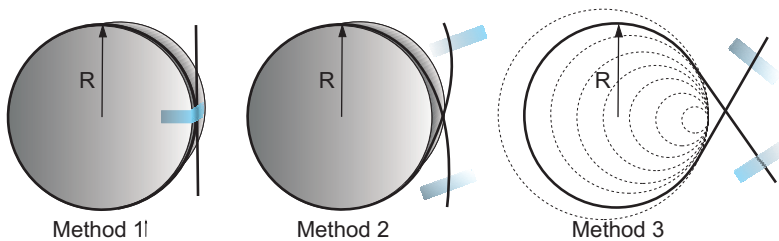

Figure 4.2: Different methods of applying defined bends to a fiber.

losses in addition to the bending losses. With a smoothly varying bending radius from $R = \infty$ to $R = R_{\mathrm{mandrel}}$, the mode can adapt adiabatically (method 2) which prevents mode mismatch.

The third method uses free loops without a mandrel. A printout on paper with distinct circles is used as a template to fit the fiber to a certain radius. In general, this method also prevents mode matching losses, but the shape of the curvature ("roundness" of the free loop) depends on the diameter of the fiber cladding. This makes the comparison of different fibers more difficult, and the reproducibility of the experiments with method 3 turned out to be lower than for the other methods. Method 3 was therefore only used for large radii ($R > 0.2\,\mathrm{m}$) for which no mandrels were available and the deviations in curvature due to the fiber stiffness is less pronounced.

Figure 4.3 compares the results obtained with the methods 1 and 2. The test fiber was a low-NA step index fiber with a core diameter of 30 µm. All displayed points are mean values of three different measurements. As described above, method 1 results in higher losses due to mode mismatch at the critical transitions of straight and bent fiber parts. The two curves in figure 4.3 have the same line shape, but they have a mean offset of about 9%. This offset is different for other fibers, it can be almost zero (as in the case of the 19-core fiber (chapter 5.1.2)), or, as high as 34% (as in case of the BF180 fiber (chapter 5.2.3)). The relative standard deviation (RSD) of N measurements of the bending losses α_R in % is given by

$$RSD = \frac{\sum_{n=1}^{N} \sqrt{(\alpha_{Rn}(R) - m(R))^2}}{m(R)} \cdot 100 \tag{4.2}$$

where $m(R) = 1/N \sum_{n=1}^{N} \alpha_{Rn}(R)$ is the mean value of N measurements.

For the bending losses of the step index fiber described above, the RSD is 6.81% for method 1 and 5.07% for method 2. The RSD is different for other fiber types, but always similar for both methods. Usually, method 3 leads to very large values (e.g., twice as high as for the other methods). Because of the differing influence of the mode mismatch for different fibers and the resulting problems when comparing different fiber types, only the results obtained with method 2 are shown in the following chapters.

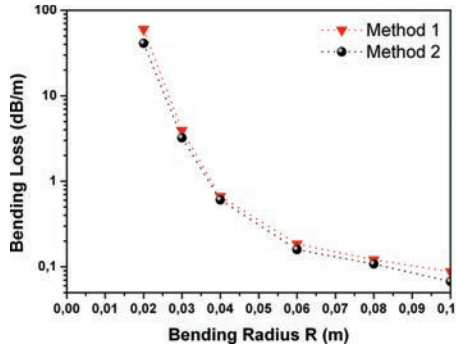

Figure 4.3: Results of the bending loss measurements of a low-NA step index fiber with a core diameter of 30 µm. Bending method 1 (red triangles) results in higher losses than method 2 (black circle) due to a mode mismatch at the points where the straight fiber is abruptly bent with a radius R.

4.2 Experimental Setup

Most of the measurements have been performed with light of low temporal coherence (50 nm FWHM) from an amplified spontaneous emission (ASE) source (Multiwave ASE) with a center wavelength of 1.05 µm and an output power of about 20 mW. This source is supplemented by a single frequency tunable diode laser (Sacher Lasertechnik). Both sources are fiber coupled and can be exchanged by plugging them to a collimation package (Thorlabs).

As shown in figure 4.4, the collimation package is placed on a kinematic mount to control the angle of the collimated beam which can then be shaped with free space optics (polarizers, wavelength selective filters, waveplates, etc.).

A plane-parallel glass plate can be used to offset the beam and lenses suitable to match the mode field diameter of the fiber with the free space beam are used to couple the beam to the fiber under test. The fiber end is adjusted to the beam with a nano-positioning system (Thorlabs Nanomax). A large space is used to arrange the fiber in large circles on the table. The remaining fiber end is then placed to measure the transmitted power. Usually, the beam is again collimated to measure near- and far-field distributions with the help of a measurement setup using CCD-

cameras (as presented in section 4.2.2), or, to measure the beam caustics with a *Spiricon M^2-200* to obtain the beam propagation factor M^2.

4.2.1 Automated Coupling

To conveniently speed up the process of coupling the free space beam to the fiber and to increase the reproducibility, a three-axis nano-positioning system (*Thorlabs Nanomax 300*) with stepper motors was used to automatize the process. The travel of each axis is 4 mm, the accuracy is specified with 1 µm and the reproducibility with 0.5 µm. The programming language Labview was used to control the positioning system with the help of a *BSC103 Three Channel Stepper Motor Controller* and an optimization algorithm to maximize the transmitted power [58].
First, the program scans a certain rectangular area with the fiber end to find a initial signal which can be used for optimization. The signal is detected with a photodiode behind the fiber. The signal of the photodiode is read out with the help of a *Keithley KUSB-3108* data acquisition module which is connected to a USB-port. First this signal is optimized with an improved Hill climbing algorithm in x and y direction then the focusing (z-axis) is improved [58]. After changing the z-position, the x and y direction is optimized again. The fine tuning is achieved by an optimization loop with variable motor step size until a termination condition is reached.

4.2.2 Near- and Far-Field Characterization

Several different experimental setups to measure the near- and far-field images of a beam delivered by a test fiber were used. Here, only the most advanced version [59] is described as schematically drawn in figure 4.4 (NF-FF-setup).
The fiber end face is placed on a 3-axis positioning system and aligned to interchangeable collimation optics. Far-field apertures can be used to restrict the NA of the collimated beam by blocking high NA parts which allows to measure the amount of power transported within a certain NA. A highly reflecting (HR) mirror can be used for high-power applications to redirect most of the power to a water-cooled beam dump. For low-power beams an anti-reflection (AR) coated glass plate with the same thickness is used to ensure the same beam path of the transmitted part of the beam. Two folding mirrors are applied to make the system compact. Two filter wheels can be used to comfortably control the intensity on the CCD-cameras.

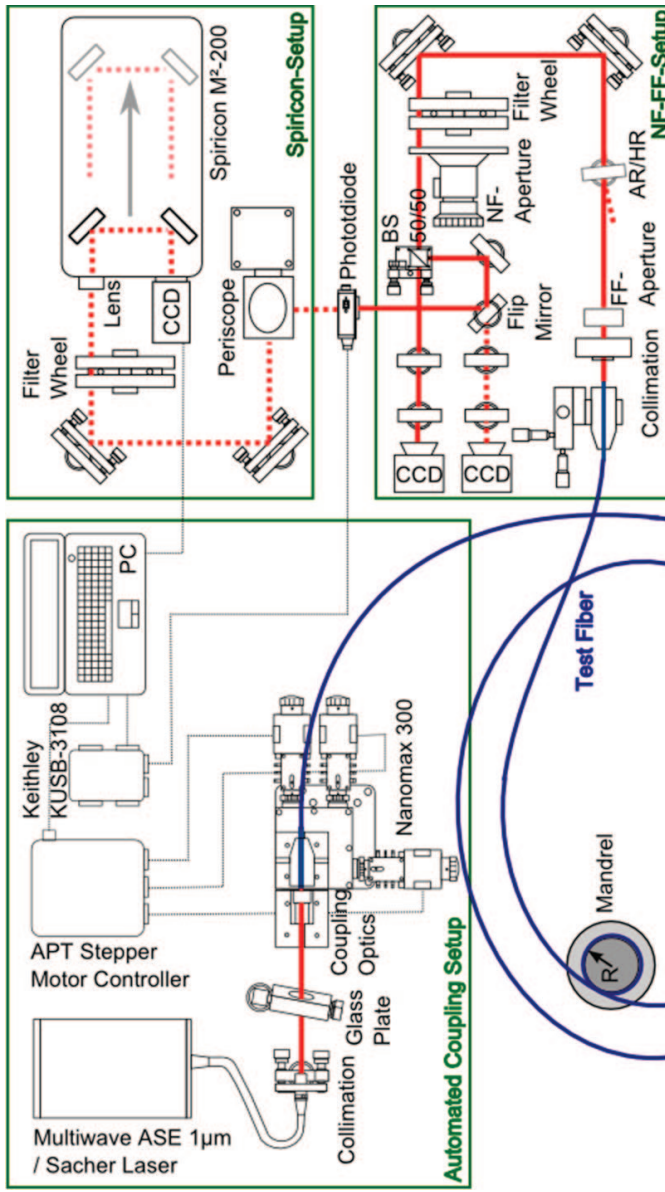

Figure 4.4: Experimental setup used for the characterization of the fibers.

The near-field is imaged to the position of a rotatable plate with holes of different sizes, which can be used to select a certain area (NF aperture),for example, to select only core-guided light while blocking the light propagating in the cladding.
A 50/50 beam splitter divides the beam in a near- and a far-field path. Flip mounts are used to apply different sets of optics to change the magnification in both arms. A higher magnification is used for (close to) diffraction-limited beams and a lower one is used for MM beams with a high NA to image NF and FF onto the two cameras. A Labview program can be used to display the camera images. The integration time and the amplification can be adjusted and an area can be defined in which the image of the beam cross section is analyzed. The diameters of the near- and far-field distributions are determined according to the 2nd moments method (2.84). Both, the beam propagation factor M^2 and the NA can be calculated with these results.
A flip mirror can be used to redirect the collimated beam for additional measurements. For instance, the beam can be redirected to a photodiode or powermeter to measure the transmitted power which allows to measure the ratio of power transmitted in the core and the cladding by using suitable NF-apertures. To determine the amount of power which is transported within a certain NA, the FF apertures can be applied. The beam can also be directed to other measurement tools such as the *Spiricon M^2-200* which performs very precise measurements of the beam caustic.

4.2.3 Measurement of the Beam Caustic with the M^2-200

By measuring the beam diameter at several positions to determine the beam caustic according to ISO Standard 11146 [27], a more precise measurement of the beam propagation factor M^2, than with the help of the NF and FF, can be achieved. At least 10 measurements have to be taken; half of them within the range of one Rayleigh length ($z_R = \pi\omega^2/\lambda$) on both sides of the beam waist ω and the other half at least two Rayleigh lengths away from the waist.
A commercial beam analyzer (*Spiricon M^2-200*) is used for this purpose. A curve fit ensures an accurate determination of the beam waist ω and the divergence angle Θ to calculate the beam propagation factor M^2. A periscope is used to align the beam to the *M^2-200*. Further ND-filters and prisms can be applied to decrease the power on the highly sensitive camera. A suitable lens (usually about $f = 500\,\mathrm{mm}$) is used to ensure a beam waist inside the device. Two movable mirrors are utilized to image different locations of the beam on a 12 bit camera as sketched in figure 4.4.

4.2.4 Cutback Method

The bending losses of a fiber can be measured by comparing the power transmitted through the bent fiber to the power transmitted through the straight fiber (or kept with a sufficiently large radius). It has to be ensured that the coupling efficiency does not change between these measurements. To measure the attenuation of the fiber itself, the power transmitted through a long piece of fiber is measured. Subsequently, this fiber is cut in such a way, that just a short piece is left without disturbing the fiber entrance face where the free space measurement laser is coupled in. By comparing the power transmitted through the short part P_{out}^{short} to the power transmitted through the complete fiber P_{out}^{long} and measuring the length of the cut part $(L^{long} - L^{short})$ the attenuation in dB/km can calculated by

$$\alpha = \frac{10 \log(\frac{P_{out}^{short} - P_{out}^{long}}{P_{in}})}{L^{long} - L^{short}} \text{dB} \tag{4.3}$$

where the length is given in km.

Chapter 5

Investigation of Specialty Fibers

Several specialty fibers were designed and optimized using the simulation tools described in chapter 3. Some of the fibers were produced at the IFSW others were obtained from specialty fiber suppliers or collaboration partners. The fibers were characterized with the experiments described in the previous chapter.
Within the present chapter the results of simulations and experiments are compared and discussed. Different wavelengths are stated in this chapter since some fibers were optimized for thin-disc lasers (with 1030 nm wavelength) and others for fiber lasers (with a wavelength of about 1080 nm). Mainly a broadband ASE source with a center wavelength of 1050 nm was used for the characterization of the fibers.

5.1 Multicore Fibers

The idea behind the multicore approach is to arrange several cores in a way that they will couple with each other. The modes of such a multicore fiber will be distributed over the whole core array which increases the mode field area compared to the eigenmodes of the individual cores. The eigenmodes of the coupled cores are so-called supermodes.

5.1.1 Principle of Coupled Waveguides: 2 Coupled Cores

The coupled-mode theory [29] suggests that the fields within different cores can evanescently couple either in phase (symmetric) or with a π-phase shift referred to as antiphase (antisymmetric). In general, this leads to $2N$ supermodes for a number

of N single-mode cores. To understand the concept, it is helpful to consider the simple case of only two cores.

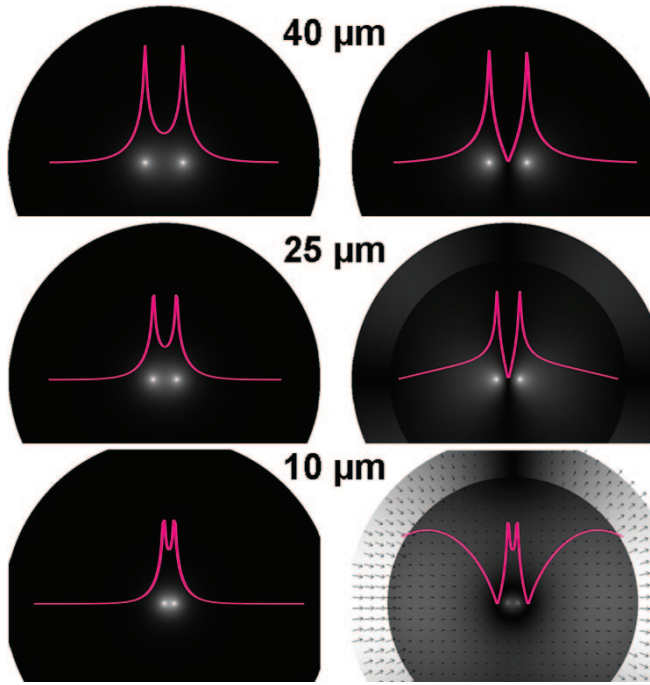

Figure 5.1: Symmetric (left) and antisymmetric (right) coupling of 2 SM waveguides (fiber cores) at core-to-core distances of 40, 25 and 10 µm. The optical intensity is displayed in a gray scale picture together with a curve along the cross-section which intersects both cores.

Figure 5.1 shows the calculated optical intensity ($\propto \left|\vec{E}\right|^2$) of the eigenmodes of two identical cores with $r_{co} = 0.5\,\mu\text{m}$, which are coupled within a common cladding of pure silica, for different core separations. The cores have a NA of about 0.24 and a wavelength of 1 µm was assumed for the calculation.

As expected, the fields can couple symmetrically, as shown on the left side, or antisymmetrically, as shown on the right side. The curves plotted on top of the

gray-scale intensity distributions illustrate the intensity distribution along the axis through the center of the two cores. In the case of symmetric coupling, the optical intensity between the two cores is increased, whereas, due to the symmetry, there has to be position of vanishing intensity in the case of antisymmetric coupling (unless the distance of the cores becomes too small as in the case of 10 µm separation). At large separations, the symmetric as well as the antisymmetric supermodes are well confined in the region of the cores. The supermodes can then be expressed as superpositions of the fields of the single cores as expected from the perturbation theory briefly described in chapter 2.4. This theory can be used to describe weakly coupled waveguides. However, if the core separation is reduced, in the example shown here from 40 to 25 µm, the situation changes. The symmetric case is still well confined, but in the case of antisymmetric coupling the field is decaying much slower into the cladding. This mode can no longer be described as a simple superposition of the fields of the single cores as described by equation 2.59. Perturbation theory cannot be applied, and numerical methods have to be used.
The simulations showed, that in general the in-phase supermode has a higher effective refractive index than the anti-phase mode and is therefore better confined and less sensitive to distortions such as bends. On the other hand, the confinement of the anti-phase supermode is reduced compared to the eigenmode of a single uncoupled core. Reducing the distance between the cores further eventually results in a situation where only the in-phase supermode is confined, whereas the anti-phase mode cannot be considered as a core-guided mode anymore. The strong coupling of the two SM waveguides resulted in only one supermode with a much larger mode field area.

5.1.2 19-Core Fiber

The results described above suggest that it is possible to make a multicore fiber which guides only the fundamental in-phase supermode. Therefore, a design with 19 identical SM cores was developed in order to achieve a large mode field area while keeping the fiber SM [60].
Figure 5.2 shows a picture of the fiber end face taken by a microscope (LHS) while the other end of the fiber was illuminated with white light. Additionally, the cores can directly be observed with the help of a scanning electron microscope (SEM). Each single core has a diameter of 2 µm and a NA of 0.108. The center-to-center distance is 5.5 µm and the cladding diameter of the fiber is 250 µm.

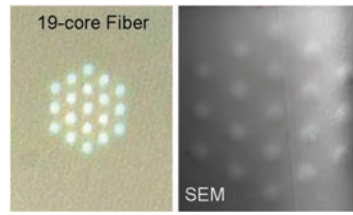

Figure 5.2: Microscope photograph (LHS) of the fiber end face and a scanning electron microscope (SEM) picture (RHS) of the core region of a SM fiber consisting of 19 coupled cores.

Increasing the number of cores and reducing their cross sections allows to extend the mode field area A_{eff} and to improve the coupling to free space Gaussian beams. The calculated and measured NF intensity distributions of the transmitted beam are shown in figure 5.3. The measurements are in good agreement with the calculations. Curves of the intensity distributions along the dashed axes are shown as solid lines. Their Gaussian fits are superimposed as dotted lines to demonstrate that the in-phase supermode exhibits a good overlap with a Gaussian beam.
As a result, the fiber can be used like a standard SM fiber without the need for mode conversion or lens arrays. Simulations of butt-coupled fibers with the same A_{eff} showed, that the overlap of the fundamental mode of a step index fiber and the supermode of the 19-core fiber can be higher than 99%. If the 19-core fiber is spliced to a SM fiber laser, this will be an essential requirement to achieve efficient coupling. For the 19-core fiber a resulting NA of 0.028 and an A_{eff} of 465 µm^2 were determined

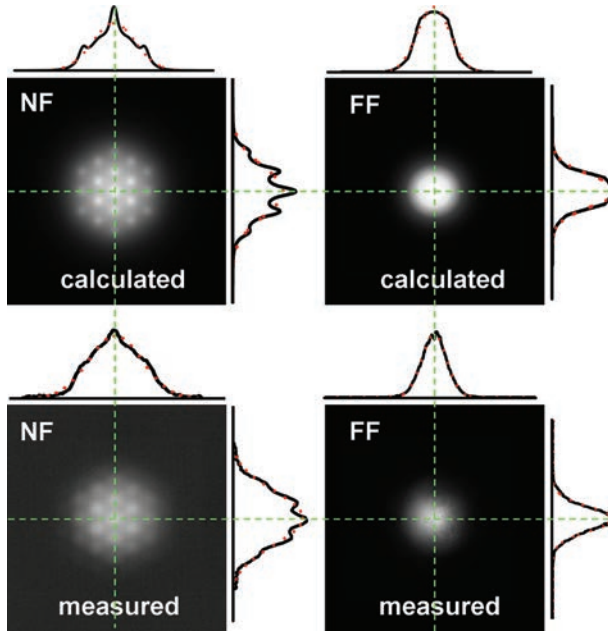

Figure 5.3: Calculated and measured intensity distributions of the NF and the FF of the 19-core fiber. Line scans along the two dashed axes are plotted as solid lines and Gaussian fits as dotted lines.

from the measured near- and far-field pictures. These values are very close to the expected values of NA = 0.03 and $A_{\text{eff}} = 470\,\mu\text{m}^2$ given by the simulations. The FF distribution (figure 5.3) is essentially Gaussian.

The 19-core fiber was first produced by the *Institut für Photonische Technologien e.V.* (IPHT) in Jena. In a second production run the fiber was produced by the company Fiberware and the IFSW as well.

The measured as well as the simulated losses versus the varying bending radius are shown in figure 5.4. Again, the measurements (filled symbols) are in good agreement with the theoretical predictions (open circles). The fiber produced by Fiberware showed the highest bending losses. For small bending radii, the measured losses are lower than predicted by the calculations. This may be attributed to the elasto-optical effect (chapter 2.3.1) which was not taken into account in this simulation.

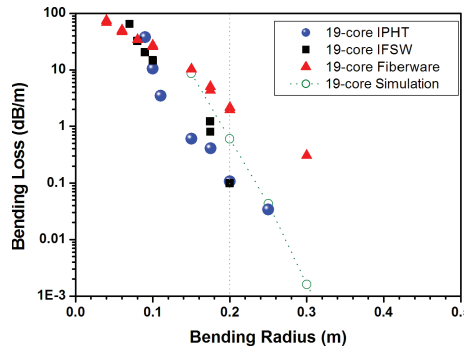

Figure 5.4: Measured (filled symbols) and calculated (open circles) bend-induced losses of 19-core fibers produced by different suppliers.

5.1.2.1 Beam Quality of the 19-Core Fiber

To verify that the fabricated 19-core fibers transport laser light with a high beam quality, the beam propagation factor M^2 was measured for different lengths and bending radii using the broadband ASE source. All measurements were performed according to the ISO 11146 standard [27] using the beam propagation analyzer Spiricon M^2-200 (chapter 4.2.3). The M^2-factors of all measurements were lower than 1.1. A typical result of the measurement of a beam caustic obtained after a 19-core fiber is shown in figure 5.5. In this case, the resulting beam propagation factor is $M_x^2 \approx M_y^2 \leq 1.03$.

To further prove that the fiber is really SM and does not only preserve the beam quality of the used laser, the beam of the single frequency laser (Sacher Lasertechnik) with a wavelength of 1030 nm was coupled into a coiled MM fiber (NA = 0.22, 200 µm core diameter) to produce a highly MM laser beam at the fiber exit.
The fiber end was then butt-coupled to a short piece (1.6 m) of the 19-core fiber, thus massively overfilling the core diameter as well as the NA of the multicore fiber. Even in this case the measured M^2 after the 19-core fiber was less than 1.1. This clearly shows that the fiber works as an efficient SM filter which does not guide any HOMs.

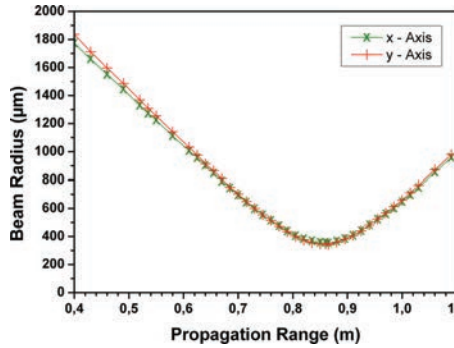

Figure 5.5: Measured beam caustic after the 19-core fiber. The measurement in two orthogonal directions (green/red) reveals M^2-factors of $M_x^2 \approx M_y^2 \leq 1.03$ and an excentricity of the beam of 1.03.

Because of the microstructured core and the resulting modulated NF intensity distribution these low M^2-factors are somehow surprising. Several calculations were performed to derive a M^2 value theoretically. For that purpose, the NF distribution obtained from the COMSOL simulation was used to calculated the FF with the help of the Kirchhoff integral (2.85).

A diffraction pattern is visible in the FF as shown by figure 5.6. However, according to the calculation, the diffraction rings only contribute to about 0.4% to the total optical intensity. Only because a logarithmic scale is used to show the intensity curves along the main axes the diffraction pattern is clearly visible.

To further investigate the influence of the diffraction pattern on the beam propagation factor, the M^2 was calculated from the NF and FF distributions. The high-NA parts of the intensity distribution can be cut by changing the size of the area in which the FF is calculated to investigate the influence of the diffraction pattern.

The results of the calculations are shown in figure 5.7. For both main axes, the calculated M^2-factor does not change much in a calculated range of 6 times the $1/e^2$ beam radius. In this region the M^2-factor is close to 1.03 which agrees extremely well to the measurement shown in figure 5.5. If a larger area is considered in the calculations, corresponding to 6 to 9 times of the $1/e^2$ beam radius, the M^2-value increases due to the diffraction pattern.

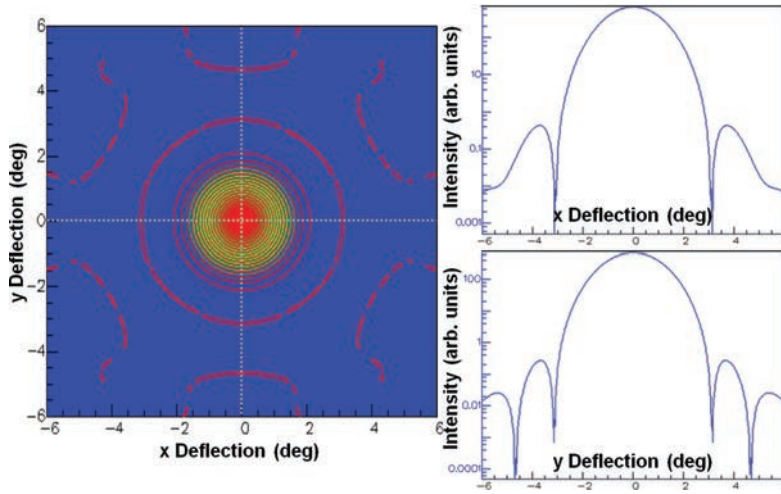

Figure 5.6: Intensity distribution of the FF calculated for the supermode of the 19-core fiber showing the diffraction pattern. The red contour lines correspond to equal intensity levels. The two curves on the right show the intensity along the two dotted lines on a logarithmic scale.

But even if larger domains are calculated, using a FF area which contains about 100% of the power, the corresponding beam propagation factor M^2 is approxematly 1.25. This is a reasonable value considering the modulated NF pattern. Since the experimental measurements are usually done using a region of interest on the camera image of about 2 beam diameters, the influence of the high diffraction angles is often not examined. Even if a region of several beam diameters is imaged on the camera, the diffration pattern cannot be observed directly because of the limited dynamic range of the CCD-cameras.

Cutting the diffraction pattern to increase the beam quality can be accepted form a practical point of view because the diffraction pattern contains only a very minor part (0.4%) of the power. It will not cause a problem for the efficiency of possible applications. However, depending on the application, the diffraction pattern should be blocked using an aperture.

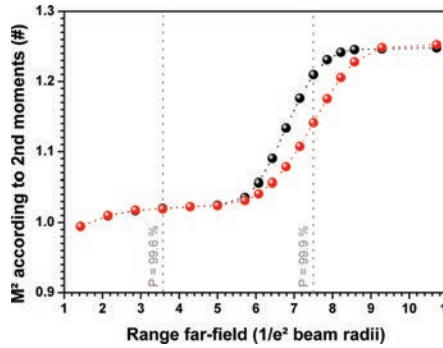

Figure 5.7: M^2-factor calculated for the two main axes. The obtained M^2-factor depends on the size of the area on which the far-field is calculated and therefore on the power which is cut. Two power levels contained within a certain far-field range are indicated by gray dotted lines.

5.1.2.2 Comparison of the Attenuation of 19-Core Fibers from Different Production Facilities

Because of the good results obtained with the first 19-core fiber produced by the research institution IPHT in Jena, more fibers were fabricated. The IPHT produced a 2nd fiber and the company *Fiberware* was interested in the topic as well and produced another 19-core fiber. A 4th 19-core fiber was produced in house at the IFSW by using a stack-and-draw technique. The nominal parameters were the same for all fibers, but the different production runs led to different results.

All fibers were characterized with the same experimental setup presented in chapter 4.2. By using a collimation package with a focal length of $f = 11\,\mathrm{mm}$ and a focusing lens with $f = 45\,\mathrm{mm}$, a coupling to a free space Gaussian beam with an high efficiency of about 86% was achieved.

Table 5.1 shows the results of the characterization of several 19-core fibers produced at different facilities and in different production runs. The first version, IPHT-1, already showed an excellent beam quality but the usable fiber length l was limited due to defects (air) enclosed in the core region. The large number of interfaces resulting from the stack-and draw preform assembling (chapter 2.7) causes inclusions of small air bubbles. These air bubbles in the preform resulted in long and thin air channels

19-Core Fiber	α [dB/km]	dx / dy [µm]	M_x^2 / M_y^2	l [m]
IPHT-1	–	24.7 / 25.7	1.02 / 1.03	5
IPHT-2	12	25.4 / 26.3	1.07 / 1.14	10
Fiberware	10.75	25.3 / 25.9	1.05 / 1.11	180
IFSW-1	33	24.3 / 25.25	1.01 / 1.07	34

Table 5.1: Experimental results of the characterization of 19-core fibers from different manufacturing facilities and production runs.

within the fiber which disturbs the propagation of the beam. Another difficulty is to keep all the surfaces clean during the stack-and-draw process. Impurities lead to a higher attenuation of the fiber. This might be the reason why the measured attenuation α shows the largest difference between the 19-core fibers from the different manufacturers. By using the cutback method the attenuation was obtained by means of equation 4.3. The fiber from *Fiberware* showed the lowest losses of about 10.75 dB/km, the one from the IFSW exhibited the highest attenuation of $\alpha = 33\,\mathrm{dB/km}$ (table 5.1).

5.1.2.3 High-Power Test of the 19-Core Fiber

After it was confirmed that the beam quality delivered by the 19-core fiber is excellent and the bending losses are acceptable, the 19-core fiber was tested in a high-power application. A fully fiber integrated system was set-up to avoid problems related to the coupling of high-power free space beams to fibers. Dust particles might cause the fiber ends to burn and thermally induced focus shifts would require active stabilization for compensation.

To achieve a monolithic system a tapered piece of fiber had to be used to match the mode field of the fiber laser with the larger mode field of the 19-core transport fiber. To estimate the effect of tapering the 19-core fiber, several simulations containing a geometrical stretching factor F were performed. The stretching factor is defined as $F = d'/d$ where d and d' are the original and the new diameter of the fiber respectively. Figure 5.8 shows the results of the simulations. The shrinking of the geometrical dimensions of the 19-core fiber reduces the mode field diameter (MFD) of the corresponding supermode until a stretching factor of $F \approx 0.62$ is reached. For even lower stretching factors the MFD increases again. This behavior can be

attributed to a reduced confinement of the propagating mode. According to this calculations the MFD cannot be decreased below 21 µm which is a problem because the fiber laser contains a Ytterbium-doped fiber (*Nufern LMA-YDF-20/400*) with a MFD of about 18.3 µm as an active medium. Hence, the fiber laser and the 19-core fiber cannot be matched by simply tapering the 19-core fiber.
Further calculations showed that this can be achieved by tapering a suitable step index fiber which is referred to as bridge fiber in the following. Depending on the stretching factor F, the MFD of the bridge fiber is indicated in figure 5.8 by the green rhombs. As can be seen, the mode fields of the 19-core fiber and the fiber laser can easily be matched with the help of the bridge fiber.

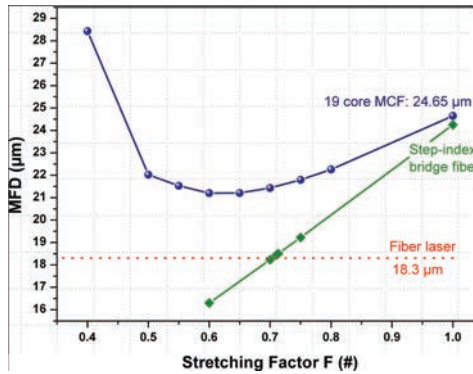

Figure 5.8: Calculated MFD of the 19-core fiber for varying geometrical stretching factors F. A tapered bridge fiber is needed in order to match the MFD of the 19-core fiber to the fiber laser source (red dotted line).

A taper based on this bridge fiber was designed using the software *FIMMWAVE* from *Photon Design*. Figure 5.9 shows a cross section of the intensity distribution in this device. The intensity profile of the fiber laser is slowly transformed due to the changing MFD of the bridge fiber to maximize the overlap with the mode of the 19-core fiber.
According to this simulation about 99% of the power from the fiber laser could be coupled to the 19-core supermode with an ideal taper and perfect fiber splices.

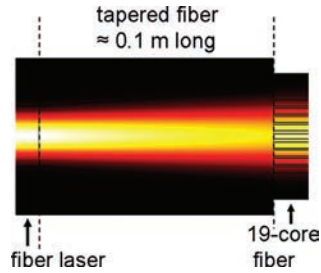

Figure 5.9: Simulation of the intensity distribution inside the taper used to match the mode field of the fiber laser source to the 19-core transport fiber.

Experimentally, a custom made taper from *ITF Labs* (which comprises an unknown step index bridge fiber) was spliced between the fiber laser and the 19-core fiber with a *Vytran GPX-3400* glass processing system. A series of beam quality and transmission efficiency measurements (not shown) were performed to examine test splices between the different fibers to increase the efficiency of the system and help the co-workers to optimize the splice parameters.

The experimental setup including the final splices is shown in figure 5.10. The fiber laser was built using 8 m of active fiber coiled on a water-cooled mandrel with a diameter of 0.1 m which was arranged between two fiber Bragg gratings (FBG). The laser was pumped by a *Laserline* diode module with a nominal wavelength of 976 nm and 1.2 kW of output power. By carefully aligning the coupling of the pump light to the fiber laser, a high slope efficiency of 76% was reached up to an output power of about 350 W [61]. To discriminate possible cladding modes, an aperture, which selects the NA of the supermode, was used between the transport fiber and the power meter.

Up to 356 W in a single transverse mode was delivered through the whole monolithic system comprising the fiber laser, the taper, and 12 m of 19-core fiber. The transmitted power scaled linearly with the pump power. The maximum output power was limited by the available power of the fiber laser source.

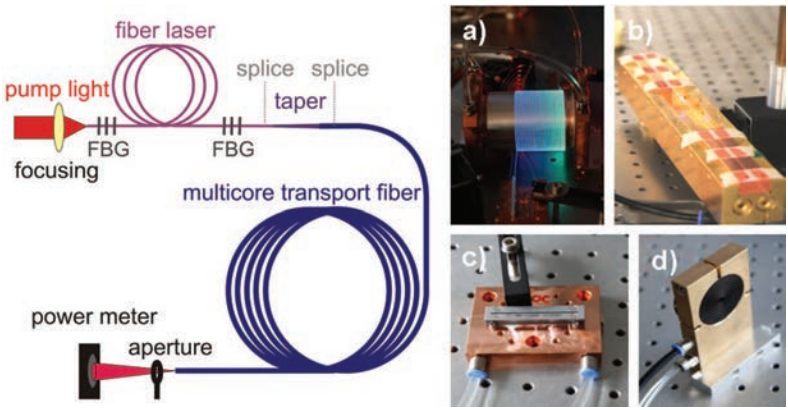

Figure 5.10: Scheme of the experimental setup used for high-power fundamental mode delivery. Photographs of the fiber laser a), the 2nd splice b), the water cooled taper c), and aperture d) are shown.

5.2 Bragg-Type Photonic Bandgap Fibers

Multicore fibers are similar to step index fibers in terms of the underlying physics because both fiber types are based on total internal reflection between a higher refractive index (multi)core region and a lower refractive index cladding region. This situation is different for Bragg-type photonic bandgap fibers.
BFs were described in chapter 2.6.3.1 and the conditions for which the circularly symmetric cladding layers are anti-resonant and light is efficiently trapped inside the core are given by the equations 2.87 and 2.88. To achieve compact and efficient fiber structures, the parameters l and m are chosen to be 0 which results in the smallest possible layer thicknesses according to these equations.
All simulations shown in this section are calculated for a wavelength of $\lambda = 1.070\,\mu\text{m}$. All modeling results were again obtained with 2nd order mesh elements of subwavelength size as described in chapter 3.2. In the case of BFs it is particularly important to resolve the thin high-index layers with a very fine mesh (about $\lambda/10$) for accurate simulation results. The losses obtained by the FEM are compared to the results of an analytical solution given by a transfer matrix method (TMM) [30]. However, the TMM is capable of calculating the modes and losses of rotationally symmetric and straight fibers, but not of bent ones.
Because it is desired to produce the BFs with common MCVD processes, the simulations were limited to an index contrast of $\Delta n = 0.02$ which is achievable by Ge-doping. The straightforward design is therefore a BF consisting of an undoped core and undoped low-index layers with $n_{\text{co}} = n_b = 1.45$ and (Ge-)doped high-index layers with $n_a = 1.47$.

5.2.1 Influence of the Core Radius

A BF with only one high-index layer as cladding is considered first to investigate the influence of the core radius on the propagation losses without any influence of a cladding period. The thickness of the high-index layer is given by equation 2.87 (about $1\,\mu\text{m}$). Figure 5.11 shows the losses of the fundamental mode of this BF with varying core radius on a logarithmic scale. As can be seen, the core radius has a large influence on the losses. Increasing the core radius from $r_{\text{co}} = 10\,\mu\text{m}$ to $r_{\text{co}} = 20\,\mu\text{m}$ decreases the losses by a factor of about 15. The influence is even more pronounced for smaller core sizes.

However, the core size cannot be increased arbitrarily because higher-order modes will appear and the sensitivity to fiber bends increases. This shows that one high-index layer is not enough to ensure that the losses are acceptable for beam delivery applications. The number of high-index layers in the cladding has therefore to be increased, which leads to further degrees of freedom in the optimization process.

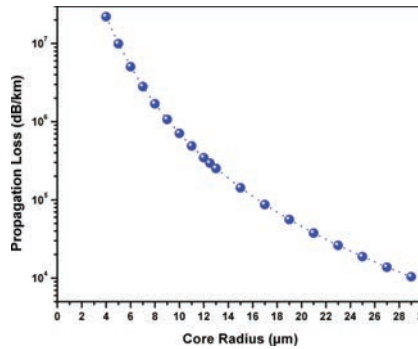

Figure 5.11: Calculated propagation losses of the fundamental mode of a BF with a single high-index layer as a function of the core radius r_{co}.

5.2.2 Optimizing Bragg Fibers

As a next step a straight BF with a core radius of $r_{\mathrm{co}} = 12.5\,\mu\mathrm{m}$ and 4 high-index layers is considered (as described above with $n_a = 1.47$, $n_{\mathrm{co}} = n_b = 1.45$). The thickness a of the high-index layers shall still be defined according to 2.87, but the thickness b of the low refractive index layers is varied. As can be seen in figure 5.12, such a BF can exhibit losses of less than 2 dB/km. Around the lowest loss value at $b \approx 8.25\,\mu\mathrm{m}$ the confinement losses are fairly stable which is convenient in view of the production tolerances. Remarkably, this optimal value does not follow the commonly stated formula (2.88). The qualitative behavior of the curve in figure 5.12 is the same for different core radii and different contrasts of the refractive indices. Increasing the core radius broadens the curve and shifts it to higher values of b.

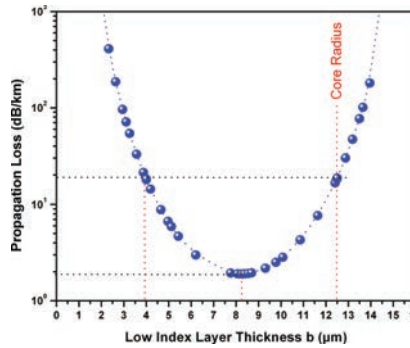

Figure 5.12: Calculated propagation losses of a large mode area (25µm core diameter) BF with 4 high-index layers with varying thickness b of the low-index layers. The red dotted lines indicate the three values of b which are used for the following comparison of the bending sensitivity.

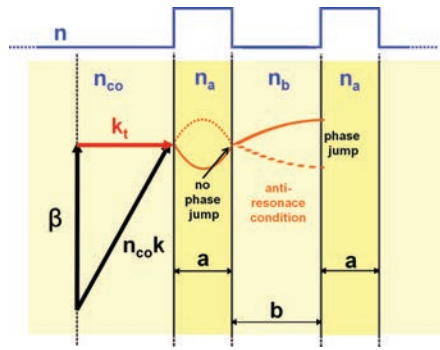

Figure 5.13: Propagation constant β in a vector picture. With the transverse component of the wave vector k_t and an anti-resonance condition the ideal layer thickness b can be derived.

The effort to find an explanation for the optimal value resulted in an analytic expression derived from the transverse wave vector k_t (see figure 5.13)

$$k_t^2 = n_{co}^2 k_0^2 - \beta^2\,, \quad \text{with } 2.38 \tag{5.1}$$

$$k_t^2 = n_{co}^2 k_0^2 - n_{\text{eff}}^2 k_0^2\,, \quad \text{with } \mathrm{k}_0 = \frac{2\pi}{\lambda} \tag{5.2}$$

$$k_t^2 = \left(\frac{2\pi}{\lambda}\right)^2 \left(n_{co}^2 - n_{\text{eff}}^2\right) \tag{5.3}$$

$$k_t = \pm\frac{2\pi}{\lambda}\sqrt{n_{co}^2 - n_{\text{eff}}^2}\,. \tag{5.4}$$

As indicated by figure 5.13, an anti-resonance condition $k_t b = \pi(2m+1)/2$ with $m = 0, 1, 2..$ derived by considering the phase jump of a wave reflected at the interface from low- to high-refractive index layers (whereas there is no phase jump at the transition form high- to low-refractive index) can be used to obtain the optimal low-index layer thickness for straight BFs by

$$b = \frac{\pi(2m+1)/2}{k_t}, \quad \text{with } 5.4 \tag{5.5}$$

$$= \frac{\pi(2m+1)/2}{\frac{2\pi}{\lambda}\sqrt{n_{co}^2 - n_{\text{eff}}^2}} \tag{5.6}$$

$$= \frac{\lambda}{4\sqrt{n_b^2 - n_{\text{eff}}^2}}\,. \tag{5.7}$$

The minus sign in 5.4 is discarded in 5.7 because only positive values of the thickness b are physically possible. Equation 5.7 has a very simple form, but it depends on the effective refractive index of the mode n_{eff} which itself depends on all structural parameters of the fiber.

However, one can design an initial structure with parameters given by equation 2.88 and calculate the effective index of the desired mode with the help of the FEM simulation. With this effective index one can calculate an improved layer thickness b using equation 5.7. This equation can then be used repeatedly until the layer thicknesses and the effective index converge to stable values.

Using this approach the optimum values can be reached in a few iterative steps as shown in table 5.2. Here, the iteration was started with a guessed value for the effective refractive index which is supposed to be smaller but close to the refractive index of the core (e.g., $n_{\text{eff}}^0 = 1.44999$). This leads to a thickness of the low-index layer b given by equation 5.7. Together with the thickness of the high-index layer a, given by equation 2.87, the structure is defined and used to calculate the modes

with the help of the FEM simulation. The effective index from the simulation result n_{eff}^1 is used to recalculate b and the geometry in the FEM simulation is adapted accordingly. A new effective index n_{eff}^2 is calculated with the FEM and used to obtain a new value for b with 5.7. At the 3rd optimization step the calculated losses are already close to the minimal losses and the layer thickness b is close to the value obtained by the FEM simulations which used a simple variation of the layer thickness to find the optimal parameters.

Step	b	Re(n_{eff})	Im(n_{eff})	Loss [dB/km]
0	—	1.449990000	—	—
1	49.673588600	1.449612580	2.030749E-08	1035.78
2	7.981096590	1.449630348	3.737904E-11	1.90651
3	8.170637660	1.449630561	3.718923E-11	1.89683
4	8.172993460	1.449630564	3.718875E-11	1.89680
5	8.173022740	1.449630564	3.718874E-11	1.89680

Table 5.2: Optimization of the layer thickness of a BF by the derived optimization routine.

For the considered Bragg fiber the optimum thickness of the low-index layer decreases the losses by one order of magnitude compared to the conventional design given by equation 2.88.

Even more interesting is the change of the characteristics of the bending losses with the thickness of the low-index layer. A comparative analysis of three similar fiber structures is shown in figure 5.14. One fiber has a low-index layer with a thickness equal to the optimum value (green dots), one has a low-index layer with a thickness equal to the core radius, as suggested by equation 2.88 (red dots), and one possesses a lower value of $b = 4\,\mu\text{m}$ (blue dots) for which the propagation losses of the straight fiber is the same as for the fiber with $b = r_{\text{co}} = 12.5\,\mu\text{m}$ (green dots).

The fiber with the highest value of b, designed according to equation 2.88, is very sensitive to bending. Even a very large bending radius of $R = 0.5\,\text{m}$ results in losses which are nineteen times higher than the losses of the straight fiber. If only 4 high-index layers are used, the design with the largest value of b is not suitable for flexible beam delivery systems.

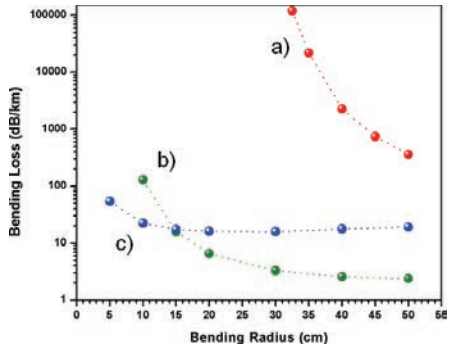

Figure 5.14: Simulated bending losses of three BF which only differ in the thickness b of the low-index layers (a) red: $b = r_{\mathrm{co}} = 12.5\,\mu\mathrm{m}$, b) green: $b = 8.25\,\mu\mathrm{m}$, c) blue: $b = 4\,\mu\mathrm{m}, r_{co} = 25\,\mu\mathrm{m}$, $n_{\mathrm{co}} = n_b = 1.45$, $n_a = 1.47$).

The bending loss curves of the other two simulated fibers cross at a bending radius of $R \approx 0.15\,\mathrm{m}$. For lower bending radii the structure with $b = 4\,\mu\mathrm{m}$, which shows only a very low influence to bends, exhibits lower losses.

However, depending on the application one might choose the design with the intermediate thickness of the low-index layer with $b = 8.25\,\mu\mathrm{m}$ because of the lower confinement losses of the straight fiber. The calculated curves prove that there is a trade-off between the confinement losses and the sensitivity to bending within the optimal design space.

The high bending sensitivity of the fiber with $b = r_{\mathrm{co}} = 12.5\,\mu\mathrm{m}$ can be explained by figure 5.15b). As can be seen, a considerable part of the corresponding fundamental mode simulated here for a bending radius of $R = 0.2\,\mathrm{m}$ is shifted into the cladding layers which causes the high losses. Whereas for the structure with $b = 4\,\mu\mathrm{m}$, the mode is well confined within the center of the fiber (figure 5.15a)).

Another interesting feature of BFs with a low layer thickness b is that the deformation of the intensity pattern of the fundamental mode due to fiber bends is comparably weak. Figure 5.16 shows a comparison of the simulated intensity distributions of the fundamental modes of a step index fiber (NA=0.07) and a BF with $b = 4\,\mu\mathrm{m}$ when they are both bent with $R = 0.03\,\mathrm{m}$. Both fibers have the same core diameter of $25\,\mu\mathrm{m}$. Despite the strong bend, the modes are well confined inside the core, but

the mode of the step index fiber is deformed much more and its mode field area is strongly decreased.
If the layer thickness b is larger, for instance, $b = r_{co} = 12.5\,\mu m$ as in 5.15b) the calculated mode field area might even increase when the fiber is bent because the intensity distribution is shifted partly into the cladding rings. Reducing the layer thickness avoids this decrease of the beam quality as can be seen by the comparison in figure 5.15a).

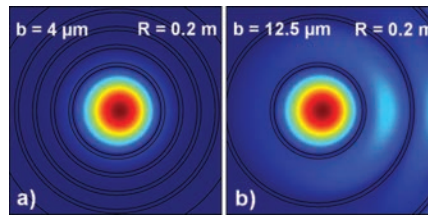

Figure 5.15: Calculated electric field distribution of the fundamental mode at a bending radius of $R = 0.2\text{m}$ for two BFs with $b = 4\,\mu m$ a) and $b = r_{co} = 12.5\,\mu m$ respectively b).

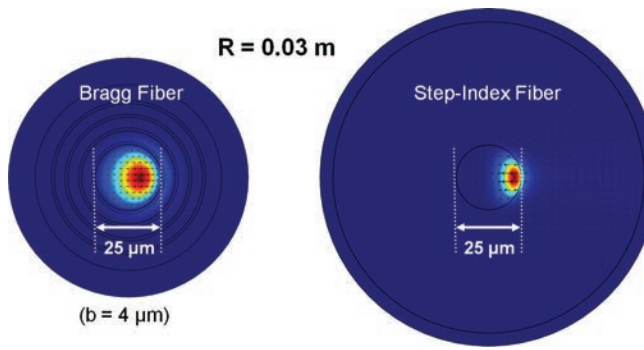

Figure 5.16: Comparison of the bend-induced field deformation ($R = 0.03\text{m}$) of the FM of a BF with a small layer thickness of $b = 4\,\mu m$ and a step index fiber (NA = 0.07) with the same core diameter.

Besides the bending sensitivity, it is interesting to know how the layer thickness affects the usable wavelength range which can be delivered by the BF. To investigate this, the wavelength is varied and the confinement losses of all discussed structures are calculated. Figure 5.17 compares the bandwidth of the three fibers.
The lowest usable wavelengths are very similar for $b = 8.25\,\mu m$ and $b = 4\,\mu m$. The losses increase significantly at about $\lambda = 0.6\,\mu m$. For $b = 12.5\,\mu m$ the short wavelength limit is shifted by 50 nm to higher wavelengths compared to the two other fibers. The long wavelength limit is less sharp. For $b = 12.5\,\mu m$ it is also shifted by 50 nm to higher wavelengths compared to the fiber with $b = 4\,\mu m$ resulting in the same bandwidth for $b = 4\,\mu m$ and $b = 12.5\,\mu m$. The optimized structure with $b = 8.25\,\mu m$ has a higher long wavelength limit as the other two and therefore a broader bandwidth. Deviations from the optimized layer thickness lead to a reduced bandwidth.

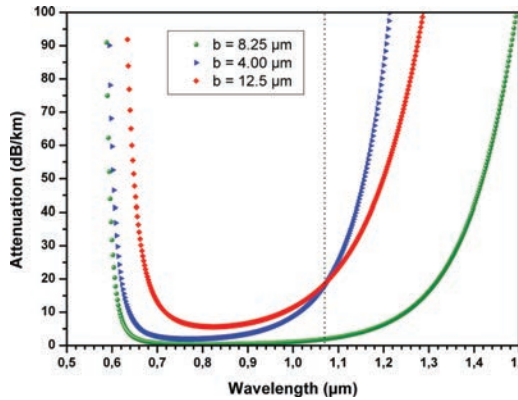

Figure 5.17: Comparison of the calculated bandwidth of the three BFs with different low-index layer thicknesses b.

5.2.3 Experimental Investigations of Bragg Fibers

The aforementioned iterative procedure was used to optimize a Bragg Fiber with a core diameter of 50 µm. The *Fiber Optics Research Institute* (FORC) in Moscow, a leading facility for the production of BFs, produced the preform using the MCVD method. With this preform the FORC produced a fiber with a diameter of 125 µm (BF125), which was used for the characterization of the refractive index profile using a commercial refractometer, and two fibers close to the nominal parameters with diameters of 180 µm (BF180) and 200 µm (BF200).
The MCVD-produced fibers tend to have a index jump in the center. Figure 5.18 shows a scan of the refractive index of BF125 in two orthogonal directions measured by the FORC. The scan was rescaled to resemble that of BF180 (from the same preform). The y-scan shows a peak of the refractive index in the center of the fiber which could influence the mode structure.

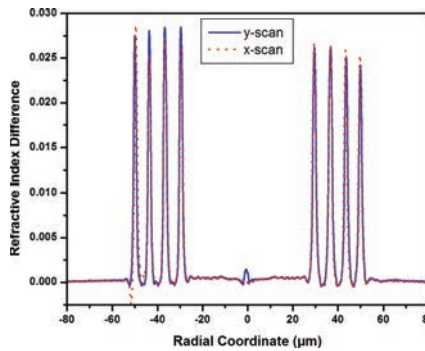

Figure 5.18: Refractive index profile of the produced BF relative to the cladding refractive index measured at two orthogonal directions.

Indeed, the measurement results of all three fibers revealed some problems. The losses were much higher than expected, and the measured beam propagation factors were between $M^2 = 2 - 3$ (except for very short pieces of fiber). The measured NF was more ring-shaped than Gaussian. It turned out, that the M^2-factors depend on the fiber length indicating that the mode composition changes during the propagation of the laser light. A quasi-Gaussian beam is transformed to HOMs.

Since these modes are lossy, as intended for asymptotically SM fibers, the measured attenuation of the fiber is much higher than expected. Figure 5.19 shows the NF and FF patterns obtained after one of the BFs for two different lengths. The FF was measured using the MM lens setting of the NF-FF-measurement setup (see chapter 4.2.2). For a short fiber length of $l = 1\,\mathrm{m}$ the near- and far-fields are almost Gaussian, but for $l = 10\,\mathrm{m}$ the NF looks ring-shaped similar to a LP_{11} mode. It seems, that the identified refractive index peak in the center of the fiber efficiently couples the fundamental mode to HOMs. Compared to other HOMs the LP_{11} mode is fairly well guided in this large-core fiber. Hence, the output of a long fiber is close to a LP_{11} mode.

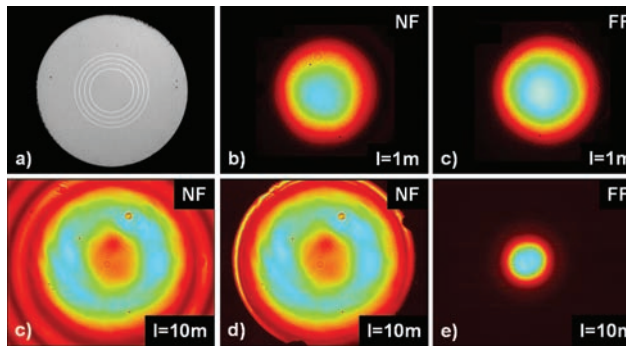

Figure 5.19: Photograph of the end face of a BF taken through a microscope a). The four high-index layers are slightly brighter than the undoped fiber parts. Measured near- and far-field patterns after a fiber of $l = 1\,\mathrm{m}$ length (first row) and a longer fiber of about 10 m length (second row). The high-index rings are visible in c) because some light was captured by index-guiding. These rings were cut with the help of a NF aperture in d).

To reduce the influence of this index disturbance in the center, the remaining preform was used to draw fibers with smaller core diameters. Although the cladding layers are becoming thinner as well, stretching the structure to a core diameter of about $25\,\mu\mathrm{m}$ results in a fiber structure which is still interesting and useful according to the simulations. Because the resulting fibers would be too thin for handling, the preform was overlaid with a second cladding of pure silica.

Three slightly different fibers with diameters of 226, 238 and 250 µm, referred to as BF226, BF238, and BF250, were drawn. The experimental results obtained with these fibers were similar to the initial fibers BF180 and BF200 with larger cores. The beam quality again decreased with the propagation length. Table 5.3 shows a comparison of the obtained M^2-factors after 1 and 10 m of fiber showing the stronger influence of HOMs for longer fiber lengths again.

Fiber	α [dB/km]	dx / dy [µm]	M_x^2 / M_y^2	l [m]
BF238	—	25.4 / 26.3	1.17 / 1.09	1
BF238	—	25.3 / 25.9	1.56 / 1.46	10
BF250	—	25.8 / 26.0	1.18 / 1.14	1
BF250	—	25.8 / 26.4	1.55 / 1.45	10

Table 5.3: Results of the characterization of BF238 and BF250 drawn from the same preform.

Beam propagation factors of approximately 1.5 were obtained with fibers of 10 m length. These values are lower as those of BF180 and BF200 with $M^2 \approx 2-3$. Apparently, the stretching of the fiber reduced the coupling to the HOMs, but it was not sufficient to ensure stable propagation of the fundamental mode whit $M^2 \approx 1.1$ as calculated by the Kirchhoff integral (2.85) with the help of the simulated NF pattern. As a result, the bending sensitivity depends on the fiber length as well because the mode composition is changing and every mode has its own bending sensitivity. Hence, the results shown in the figures 5.20 and 5.21 are only qualitative.
However, the measured losses are lower than 0.1 dB/m at a bending radius of $R = 0.1$ m for all BFs. The fiber properties are robust against bends. For the characterization of the BF250 only a very short fiber ($l = 1$ m) was used to ensure a Gaussian-like fundamental mode beam. As can been seen from the blue circles in figure 5.21, this resulted in extremely low bending losses as expected from the analyses of BFs with thin microstructured layers shown in the previous section.

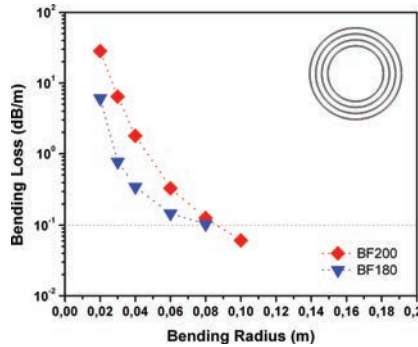

Figure 5.20: Measured bending losses of BF180 (blue triangles) and BF200 (red diamonds).

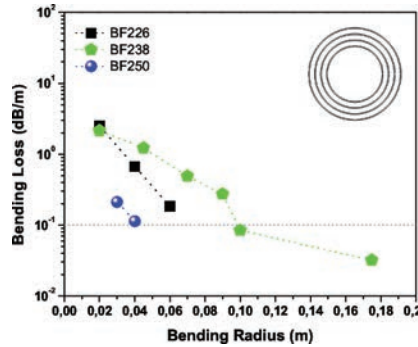

Figure 5.21: Measured bending losses of BF226 (black quadrates), BF238 (green pentagons), and BF250 (blue circles).

5.3 Leakage Channel Fibers

The LCFs considered in this chapter only consist of pure silica glass. Light is guided in the center of the fiber due to air holes surrounding the core of the fiber as described in chapter 2.6.4.

5.3.1 Influence of Basic Parameters

As depicted in figure 5.22a) the basic geometrical parameters are the core radius r_{co}, the cladding radius r_{cl}, the hole diameter d, and the center-to-center distance of the holes, called pitch Λ.
A higher number of smaller holes or a lower number with larger diameter could be used for fibers with the same core size. Depending on the ratio Λ/d, these fibers may have the same MFA and the same leakage losses. At first, LCFs with the same core radius but a different number of holes in the microstructured region were simulated to investigate the influence of the number of holes. LCFs with similar properties of the straight fibers could be obtained by varying the ratio Λ/d. These fibers were then compared with regard to the bending sensitivity and the loss ratio between the fundamental mode and the subsequent higher-order mode.

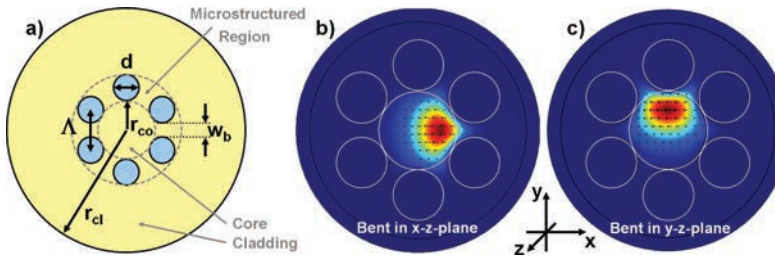

Figure 5.22: a) Scheme of a LCF. The intensity distribution of the fundamental mode is deformed and shifted due to a bent in the x-z-plane b) and a bent in the y-z-plane respectively c).

The simulations (not shown) suggested that the loss ratio decreases if more holes are used. Hence, a small number of holes is preferred because a high loss ratio is

desired to efficiently guide the fundamental mode and to prevent mode mixing as described in chapter 2.4. On the other hand, if the number of holes is decreased, the mode shape becomes more asymmetric and the bending losses increasingly depend on the direction of the bend with respect to the position of the holes. The modes inside the fiber core become deformed and shifted due to bends of the fiber. If the field is shifted toward a hole the losses are lower compared to the situation where the mode is shifted in direction of a bridge. As a consequence a LCF design with 5 holes, as shown in figure 5.23, was chosen for further investigations.

5.3.2 LCF with 5 Holes

Simulations were used to optimize a LCF with 5 holes in such a way that the losses of the fundamental mode of the straight fiber are in the oder of the attenuation of the material (about 1 dB/km) and below $\alpha_R = 0.1\,\mathrm{dB/m}$ at a bending radius of $R = 0.2\,\mathrm{m}$. Furthermore, the loss ratio of fundamental and higher-oder modes should be higher than 10 ($\alpha_{\mathrm{diff}} = \frac{\alpha_{\mathrm{FM}}}{\alpha_{\mathrm{HOM}}} > 10$) for all bending radii larger than 0.2 m. These conditions limited the core radius to values of $r_{co} \leq 15\,\mu\mathrm{m}$.

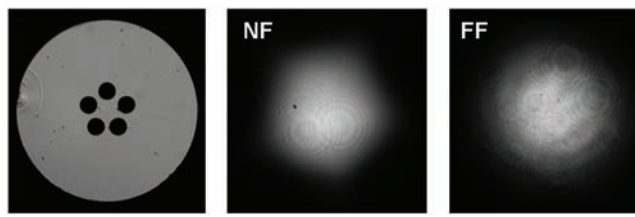

Figure 5.23: End face of an LCF with 5 holes and the corresponding near- and far-field images.

According to the optimized design, a fiber preform produced by *Heraeus Quarzglas* was drawn to a fiber at the IFSW. The produced fiber turned out to have smaller air holes than desired ($d_{\mathrm{produced}} < d_{\mathrm{design}}$).
Larger air holes, better corresponding to the design value of $d = 26\,\mu\mathrm{m}$, were then produced by reducing the furnace temperature in a 2nd production run. However, this resulted in a reduced core radius of about 14.3 µm which is slightly smaller than the target value of 15 µm. Based on these experiences the preforms for further

LCFs were ordered with a hole size 10% larger than the designed to avoid problems accociated with low drawing temperatures. A microscope photograph of the end face of this fiber as well as the measured NF and FF images are presented in figure 5.23. The NF pattern shows that the arrangement of the five holes results in a pentagon-shaped intensity pattern. From this pattern an effective mode area of $A_{\text{eff}} = 383\,\mu\text{m}^2$ was derived which is about 10% lower than the expectation for the original design with $A_{\text{eff}} = 425\,\mu\text{m}^2$. Together with the corresponding FF picture, a beam propagation factor of $M_x^2 = M_y^2 = 1.1$ was determined.
Similar values were obtained by further measurements of the beam caustic. The good M^2-value and the fact that the NF pattern remained stable when the fiber was bent shows that this fiber behaves as a regular SM fiber. Even for intentionally bad coupling conditions and a fiber length of only 3 meters, HOMs were not observed after the fiber. Hence, the losses of the HOMs and therefore the loss ratio between fundamental mode and HOMs were higher than expected. This can be explained by the smaller mode field area due to the reduced core size of the actual fiber when compared to the initial design. The smaller core leads to a lower amout of HOMs which additionally experience higher losses.
The attenuation of this fiber was measured using the cutback method. A value of $\alpha = 51\,\text{dB/km}$ was obtained with a 35.5 m long fiber. This very high value might be explained by a contamination with small dust particles disposed at the fiber end faces. Although, the measurements were done carefully on a clean optical table below an air flow filter, the pollution arose during the measurements. This can be explained if the production process is considered. During the drawing the glass is heated to nearly 2000°C and so is the air inside the holes. The fiber is rapidly cooled to room temperature when leaving the furnace. This temperature drop leads to a partial vacuum inside the air holes. Because the holes of the fiber are tiny the pressure compensation needs a long time. This results in a faint air flow which takes dust particles onto the fiber end faces and into the fiber. The particles darkened the fiber end faces which was observed with a microscope. Hence, the high attenuation of the fiber was attributed to this effect. Therefore, the measurements were repeated directly after a new piece of fiber was produced.
As expected, the measured attenuation of 22 dB/km of the new fiber (with $l = 29\,\text{m}$) is considerably lower as for the previous characterized fiber with $\alpha = 51\,\text{dB/km}$. The influence of the dust was eliminated, but the attenuation is still about 10 times

higher than expected from the simulation. This could later be attributed to a chemical reaction during the drawing process which is discussed in section 5.3.6.

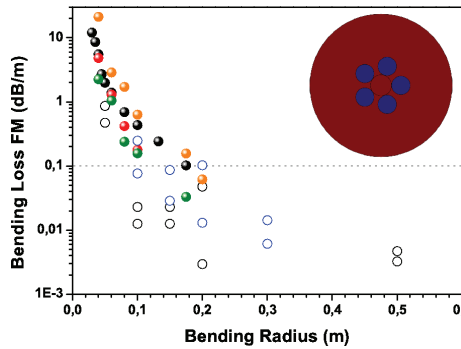

Figure 5.24: Different measurements of the bending losses (filled circles) are compared to the simulation results (open circles).

Besides the investigation of the delivered beam quality and the fiber attenuation, the bending sensitivity was also investigated. Because the fiber structure is not rotationally symmetric the bending losses depend on the orientation of the fiber. In the simulations the two extreme cases for the bends were calculated; one which shifts the mode directly to a hole and another which shifts the mode precisely between two holes. But within the measurements it is difficult to define a distinct plane for the fiber bend. Furthermore, the high contrast of the refractive index between air and silica leads to a polarization dependence of the losses. The simulation calculates eigenmodes which are fully polarized, but the measurement is done with non-polarized light. Even if polarized light would be used, the polarization dependent losses could still not be determined experimentally because the fiber does not conserve the polarization state.

Hence, a direct attribution of simulations and measurements is not possible. Therefore, the worst case scenario of the fiber bending losses was considered in the design phase to make sure that the losses are below a limit of 0.2 dB/m at $R = 0.1\,\mathrm{m}$. To take into account the different planes in which the fiber could be bent experimentally, the fiber was removed, turned, and inserted in the measurement setup repeatedly.

The measured (filled circles) and the simulated results of the bending losses (open circles) and are shown in figure 5.24. The calculated values which correspond to fully polarized modes and the extreme cases concerning the direction of the bend are scattered over a large range of losses at a certain bending radius R. The measurements revealed slightly higher losses but there is a general agreement between simulations and measurements. Based on this results further efforts were made to reduce the attenuation and to increase the mode field area while keeping the bending sensitivity low.

5.3.3 Influence of the Number of Microstructured Layers

One possibility to improve the concept might be the use of several layers of holes. Experiments on LCFs with one layer of holes are reported in [41, 42] where it was also stated that by using several layers, the loss ratio can be increased [42] which indicates that the mode field area could be increased as well.
At the time of this work no detailed experimental results on LCFs with several microstructured layers were available and no information on the their bending behavior could be found in literature. Hence, a basic analysis was performed.
First, a structure similar to the discussed LCF with one microstructured layer is extended by another layer with holes of the same size. This does not increase the loss ratio, on the contrary, the loss ratio decreases as do the overall losses ($\alpha_{\mathrm{FM}}^{1\mathrm{layer}}/\alpha_{\mathrm{HOMs}}^{1\mathrm{layer}} < \alpha_{\mathrm{FM}}^{2\mathrm{layer}}/\alpha_{\mathrm{HOMs}}^{2\mathrm{layer}}$). More holes make the index guiding more efficient. To compensate for this, the hole size has to be decreased and the positions of the holes have to be adjusted as well to keep the core size equal. To make an meaningful comparison, the hole size was decreased until the fundamental mode of the two-layer structure had the same (straight fiber) losses as the fundamental mode of the single-layer structure with the same core size. Then the loss ratio and the bending behavior of these fibers were calculated to investigate which benefits could be achieved by introducing more microstructured layers.
A series of simulations for two structures with similar mode field area and similar losses of the fundamental mode but with 6 (one layer) and 18 (two layers) holes were performed. It turned out that the loss ratio of the fundamental LP_{01} mode and the LP_{11} mode are 3 orders of magnitude larger for the structure with 18 holes. This means that the mode field area could indeed be increased considerably by decreasing the hole size and introducing a second layer of holes. The attenuation is increased

with decreased core size, but this can is compensated by the second microstructured layer. However, the simulations also showed that the resulting 18-hole structure is more sensitive to bending than the simple one-layer structure. Because the hole size d is decreased, while the core size is kept constant, the bridge width w_b for the two-layer structure is increased $w_b^{2\text{layer}} > w_b^{1\text{layer}}$ (LCF scheme in figure 5.22). This leads to higher bending losses which apparently cannot be compensated with a second layer of air holes. As the bending losses strongly depend on the bridge width w_b, hence, the two layer structure is more sensitive to bending.

To investigate this finding in more detail, three fibers with equal hole and core sizes but different numbers of microstructured layers are considered in the following. The holes are arranged in a hexagonal crystal lattice. The structures with one and two layers can be derived from the structure with three layers by removing the outer layer(s). The corresponding calculated results of the bending losses are shown in figure 5.25.

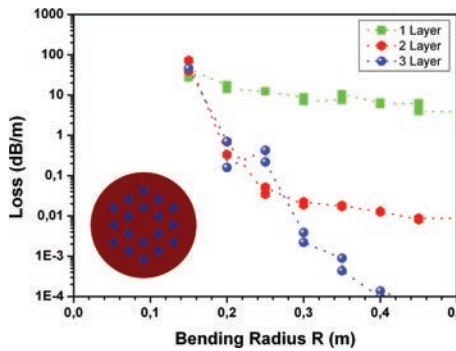

Figure 5.25: Comparison of the bending sensitivity of 3 LCF structures with identical parameters but different numbers of layers of holes in the microstructured region.

Naturally the fiber with the highest number of layers (highest number of holes) exhibits the lowest losses (if the fibers are kept straight) because the hole size d is the same for all the fibers. However, if the fibers are bent, their losses converge with decreasing bending radius R.

This means that increasing the number of layers did not improve the bending sen-

sitivity it simply reduced the confinement losses of the straight fiber. Therefore, it can be concluded that if the fiber design is limited by the loss ratio, increasing the number of layers will improve the design space. But if the design is limited due to the bending losses, increasing the number of layers is not sufficient to substantially reduce these losses at low bending radii.

5.3.4 Optimization of the Microstructured Layers

Another freedom of design for a LCF with several mircostructured layers is to use different hole sizes in different layers. Further FEM simulations showed that this possibility can be used to reduce the bending sensitivity of such structures. As an example, a LCF with an inner layer made of 6 holes with a diameter of 12.0 µm and an outer layer made of 12 holes with a diameter of 14.6 µm is considered in the following. The 18 holes of this chirped LCF are positioned as a hexagonal lattice as shown by the inset in figure 5.26. The fiber is referred to as CLCF18.
The mode field area of the fundamental mode was calculated to be 708 μm^2 at a wavelength of 1080 nm according to equation 2.41. The CLCF18 is compared to a LCF with the same number of holes at the same positions, but with an equal intermediate hole size of $(d = 12.0\,\mu m + 14.6\,\mu m)/2 = 13.3\,\mu m$ for all holes. This fiber is referred to as LCF18. The area of the fundamental mode of the LCF18 was calculated to be 647 μm^2 at 1080 nm. Compared to the CLCF18 the inner holes of the LCF18 are larger, but their center positions are the same which results in a smaller core size. Therefore, the calculated mode field area of the fundamental mode of the LCF18 is about 9 % smaller than the corresponding value for the CLCF18. Hence, one could expect that the LCF18 has a lower bending sensitivity than the CLCF18. However, the simulated bending losses shown in figure 5.26 reveal that the losses of the fundamental mode of the CLCF18 (indicated by the black circles) are lower than those of the fundamental mode of the LCF18. Since the bending sensitivity is reduced and the mode field area is increased in case of the chirped structure, it can be concluded that introducing different hole sizes, increasing from the inner to the outer layer, improved the LCF design.
A minor drawback of the CLCF18 is that the losses of the straight fiber are slightly increased, but the magnitude is still lower than the material absorption. Hence, this disadvantage can be neglected in real world applications. Another special feature of the CLCF18 design is the extremely large loss difference between the fundamental

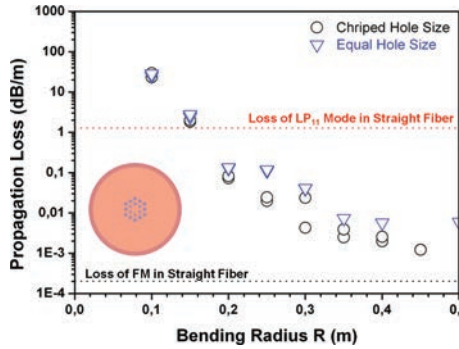

Figure 5.26: Comparison of the bending losses of the LCF18 with equal hole size (triangles) to the CLCF18 with a chirped hole size (circles).

LP_{01} mode and the LP_{11} mode as indicated by the dashed lines in figure 5.26. The propagation loss of the fundamental mode is about 0.2 dB/km (material absorption is not considered) for the straight fiber (black dashed line), whereas the loss of the LP_{11} mode is > 1 dB/m (red dashed line). Despite the large core or large mode field area respectively, the structure is asymptotically SM with a very high loss ratio. This was achieved by specific cladding resonances as explained in the following section.

5.3.5 Optimization of the Cladding Diameter Using Cladding Resonances

Another approach to further improve the described LCF makes use of a resonant coupling to cladding modes [62]. In conventional step index fibers, the core-guided modes have a larger effective refractive index than the cladding modes because the core modes are propagating in a region with higher refractive index.
In case of the LCFs, the core and the cladding consist of the same material. Therefore, the effective refractive indices of core and cladding modes may be similar. The real part of the effective index of the core modes mainly depends on the core size which is usually fixed by some constraints (maximized area at certain bending, loss ratio, mode spacing,..). The real part of the effective index of the cladding modes depends on the cladding diameter which can, to a large extent, be chosen arbitrarily.

Hence, the cladding diameter can be optimized to match a cladding mode to the LP_{11} mode which will enhance its losses. If the losses of the LP_{11} mode are increased, the loss ratio as well as the loss difference is increased which improves the design according to the discussion in chapter 2.4. On the other hand, one should make sure that no cladding mode is in resonance with the desired fundamental mode.
Figure 5.27 shows the calculated losses of the LP_{11} mode of the CLCF18 for different cladding diameters. Three peaks are visible in the range of 370 to 405 µm indicating that three different cladding modes become resonant with the LP_{11} mode depending on the diameter of the cladding.

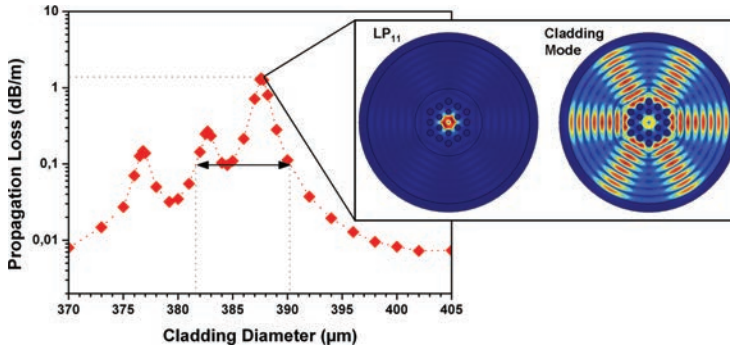

Figure 5.27: Losses of the LP_{11} mode for different cladding diameters of the CLCF18. By changing the diameter of the cladding and keeping all other parameters (hole size, separation, and arrangement) constant, three resonances with increased losses are obtained. The strongest coupling to cladding modes is achieved at a diameter of 387.58 µm. The inset shows the field distributions of the LP_{11} mode and the cladding mode in resonance at this cladding diameter.

The highest losses obtained at a cladding diameter of 387.58 µm are more than two orders of magnitude higher than out of resonance which shows the considerable influence of these cladding resonances on the losses. The overlap of several resonances creates a broad region of increased losses in this particular design. Losses of more than 0.1 dB/m can be achieved within a resonance of about 8.5 µm width which relaxes the production tolerances.

The inset of figure 5.27 shows the LP_{11} and a cladding mode for a cladding diameter of 387.58 µm. At this diameter a cladding mode is in resonance with the LP_{11} mode. The calculated difference of the effective mode indices is only

$$\Delta n_{\text{eff}} = 1.449125493 - 1.449125433 = 6.0 \cdot 10^{-8} \tag{5.8}$$

which satisfies the phase matching condition 2.73 even in the absence of perturbations. Concerning the loss matching condition 2.80 the coupling constant and the difference of the losses of the two modes have to be considered. The coupling constant can be derived using overlap integrals. The simulations show that the LP_{11} extends into the area of the cladding, whereas a part of the cladding mode extends into the core area. But even without a detailed investigation of the coupling constant (κ) it is safe to assume that 2.80 is not fulfilled because the losses of the cladding mode are much higher than the losses of the LP_{11} mode.

The attenuation of the cladding mode depends on the fiber coating. Since a high-index polymer is used the losses of the cladding mode are many orders of magnitude higher than the losses of the LP_{11} mode. According to chapter 2.4 a complete coupling can only occure if the loss matching condition is not fulfilled. However, the LP_{11} mode is strongly affected by the cladding resonance. This can be explained by two factors. First, the two modes are very precisely at the phase matching point because the structure is designed that way and second, the losses of the cladding mode are significantly higher than the losses LP_{11} mode which leads to an considerable effective loss of the LP_{11} mode even in case of incomplete coupling.

If the losses of the LP_{11} mode are increased, the coupling of the free space beam to the fiber modes becomes much more convenient because only the delivered power has to be maximized without considering the beam quality. Furthermore, a (complete) coupling between the fundamental mode and the LP_{11} mode becomes less likely according to the loss matching condition (2.80). In contrast to the case of an incomplete coupling with a cladding mode, as described above, the incomplete coupling between two core modes would not lead to a comparably high influence on these modes because their losses are low compared to the losses of a cladding mode. Hence, this effect can be used to make the propagation of the fundamental mode in LCF more stable against distortions. The requirement for the matching of the real parts of the effective refractive indices of core and cladding modes is that the refractive index of the core material is the same as the refractive index of the cladding. For the use of the cladding resonances it was therefore not important that the CLCF18

exhibits two mircostructured layers with chirped holes.
Usually, it is advantageous that a fiber can be used at different wavelengths. Therefore, the wavelength dependence of the resonant mode coupling is analyzed. Figure 5.28 shows the results of a wavelength dependent loss calculation for the LP_{11} mode using the ideal cladding diameter of 387.58 µm.

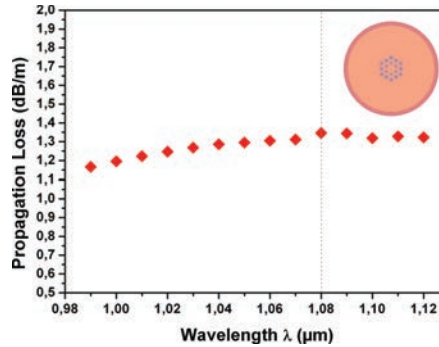

Figure 5.28: Wavelength dependence of the resonant mode coupling at a cladding diameter of 387.58 µm of the CLCF18. The graph shows the calculated losses of the LP_{11} mode at different wavelengths.

The highest losses occur at a wavelength of 1080 nm, showing that the different calculations are consistent because the structure has been optimized for this wavelength. Deviations from this wavelength reduce the losses, but the losses vary only weakly with the wavelength. This means, that the mode coupling effect can be used over a broad spectral bandwidth. The material dispersion, which is included in the calculations by the Sellmeier equation (3.23), has no influence on the cladding resonances because the materials of the core and the cladding are the same. Hence, only the dispersion of the waveguide itself has an influence.

5.3.6 Experimental Investigation of a Chirped LCF

After the design phase, the optimized CLCF18 was produced and experimentally investigated as described in the following. The fiber preform, ordered from *Heraeus Quarzglas*, had hole diameters which were increased by 10% compared to the design

to take into account the systematic production error mentioned in section 5.3.2. The fiber was drawn from the preform with a controlled pressure of a nitrogen (N_2) atmosphere inside the holes at the IFSW. Different drawing speeds and furnace temperatures were applied to achieve a fiber structure close to the designed values. This was tested with a microscope on small fiber samples taken during the drawing process. Figure 5.29 shows the comparison of the structural design and one of the manufactured fiber. The symmetry of the produced fiber is as good as expected. The holes are round and uniform and their sizes are close (white lines) to the design values, but the overall core region and therefore the core size of the produced fiber is smaller which leads to a smaller mode field area.
With the help of the broadband ASE source, the NF and FF intensity distributions were measured after the fiber. A mode field area of $A_{\text{eff}} = 3/2(d_{mean}/2)^2 \cdot \sqrt{3} = 434.44\,\mu\text{m}^2$ was calculated from the NF distribution. This value is considerably smaller than the expected value of $708\,\mu\text{m}^2$ from the fiber design. The beam propagation factor calculated from the measured near- and far-field distributions is $M^2 \approx 1.1$.

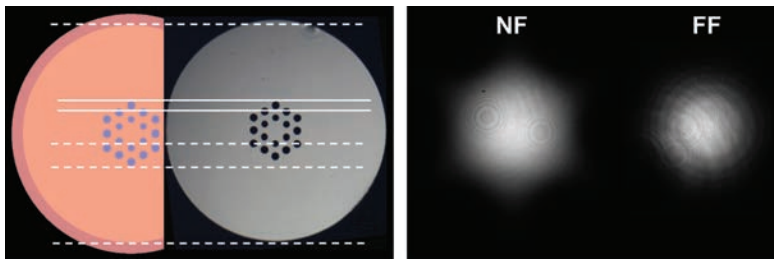

Figure 5.29: CLCF18 end face microscope picture, scaled according to the measured outer diameter and compared to the design. White lines are reference guides to the eyes (LHS). Measured NF and FF distribution (RHS).

A cutback measurement of a long piece of the first produced CLCF18 revealed an extremely high attenuation of about 120 dB/km. Since the cleaning process was already improved and pollution by dust particles was carefully avoided, other possible impurities were investigated to explain the unexpected high attenuation. It turned out that the clean nitrogen, used to stabilize the holes during the drawing

process, itself reacts with silicon monoxide SiO and a low content of carbon C or carbon oxide CO impurities and creates silicon nitride (Si_3N_4) at temperatures between 1400-1500°C [63].
Higher temperatures lead to silicon carbide (SiC). The C impurities probably arise from the cleaning of the rods of the preform with alcohol. At a wavelength of 1 µm Si_3N_4 has a refractive index of 1.99 and is highly absorbing. Hence, the strong attenuation of the CLCF18 as well as of the attenuation of the LCF5 (see previous section) can be explained by the presence of Si_3N_4. Using oxygen instead of nitrogen during the drawing process should prevent this reaction.
Based on this result, new fibers were drawn to the same outer diameter at slightly different drawing temperatures which resulted in slightly different sizes of the holes. The results of the characterization of fibers drawn at four different temperatures are summarized in table 5.4. All fibers showed a very good beam quality, as measured with the Spiricon Beam Analyzer and a low attenuation of about 6 dB/km which is only 5% of the attenuation of the first CLCF18. Filling the holes with oxygen instead of nitrogen strongly reduced the attenuation.
However, it should be mentioned that a strong "frozen-in" stress, as a result of the rapid cooling of the glass during the drawing process, makes the fiber with its 18 air holes brittle at positions where the coating quality is poor. In particular, the fiber drawn at $T = 1875$°C turned out to be very fragile.

CLCF18 drawing T [°C]	α [dB/km]	dx / dy [µm]	M_x^2 / M_y^2	l [m]
1869	—	25.4 / 26.3	1.07 / 1.14	3.2
1871	6.1	25.3 / 25.9	1.05 / 1.11	32.5
1873	5.9	25.8 / 26.0	1.06 / 1.08	132.9
1875	4.8	25.8 / 26.4	1.06 / 1.07	36.5

Table 5.4: Experimental results of the characterization of the CLCF18 drawn to the same outer diameter at different production temperatures.

The bending losses of all four CLCF18 were measured. The losses obtained according to equation 4.1 are shown in figure 5.30. The values for the fibers drawn at four different temperatures are denoted by filled symbols and the expected behavior simulated according to the design is indicated by open circles. As can be seen, the measured losses are considerably lower than the results of the simulation. The

CLCF18 was designed to have losses of 0.1 dB/m at a bending radius of $R = 0.2$ m. The discrepancy between the measured and the simulated losses is especially high for lower bending radii which can be explained by the fact that the core size of the produced fiber and therefore the effective mode field area A_{eff} is considerably smaller than designed. This makes the fiber less sensitive to bending. Not only the MFA, also the pitch Λ and hence the Λ/d-ratio are smaller because the core area is smaller, but the hole sizes are as designed. Therefore, the produced fibers are supposed to be considerably less sensitive to bending than predicted by the design.
The fibers drawn at 1869, 1871, and 1875°C show a very similar behavior. The influence of the minor temperature shifts on the hole size is rather small, but the fiber drawn at 1873°C behaves differently. At bending radii between 0.1 - 0.2 m its bending losses are increased compared to the other fibers. Repeated measurements led to similar results. The reason for this discrepancy between the LCF drawn at 1873°C and the other fibers remains unclear and will be the subject of further investigations.

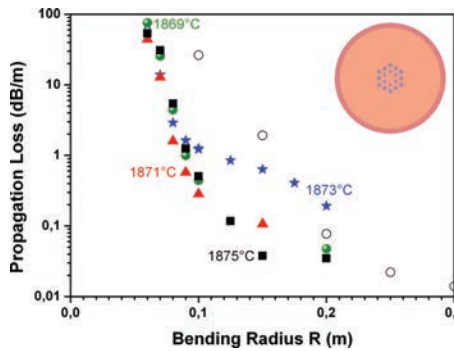

Figure 5.30: Measured bending losses of the CLCF18 produced at different drawing temperatures. The open circles represent the calculated losses according to the CLCF18 design.

5.3.7 Optimized Asymptotically 2-Mode LCF

LCFs can be made in a way that several modes are guided efficiently over a certain distance. This results in a more robust structure and offers the possibility to use larger core diameters in comparison with the asymptotically SM LCFs. Such fibers could be interesting as beam delivery systems for high-power fiber lasers because high-power fiber lasers with a good beam quality tend to have a fraction of power in the LP_{11} mode, whereas most of the power is in the fundamental mode. It would be useful to transport both modes with a passive beam delivery fiber.
As few modes as necessary should be guided by such a fiber to maintain a good beam quality. Hence, a LCF which guides only the LP_{01} and the LP_{11} mode efficiently is desired. The design considerations of such a structure are different from those of asymptotically SM LCF. The loss ratio of the two modes should be small, but the third mode and HOMs are supposed to have high losses. An interaction between the cladding resonances and the LP_{01} mode is therefore unwanted. Phase-matching (2.73) of the two core-guided modes should be avoided to prevent an energy exchange between them which restricts the core size.
The result of the design process was a simple structure with 6 air holes with a diameter of 35.4 µm and a core diameter of 51.8 µm. The structure of the produced fiber agrees very well with the design as can be seen from figure 5.31.

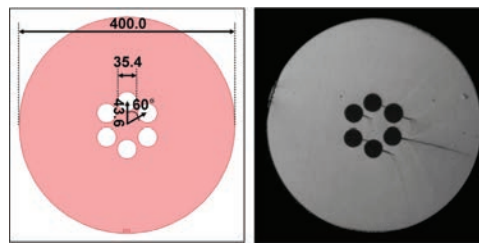

Figure 5.31: Design of the fiber (left) and a microscope photograph of the end face of the produced LCF (right). The fiber with a core diameter of 51.8 µm efficiently guides LP_{01} and LP_{11} modes.

The calculated fundamental mode of the structure has a mode field area of 1187 μm^2 at $\lambda = 1080$ nm which is higher than possible for an asymptotically SM fiber with a similar bending sensitivity. The bending losses of the fiber are reported in figure

5.32. The straight fiber is expected to guide LP_{01} and LP_{11} modes with similar losses as indicated by the black solid line (LP_{01}) and the red dotted line (LP_{11}). The fiber was designed in such a way that the LP_{11} mode, which is 4-times polarization degenerate, has bending losses which are lower than 0.1 dB/m at a radius of $R = 0.2$ m (red open rectangles). The calculated losses of the 2-times polarization degenerate fundamental mode are lower as indicated by the black open circles. Positive R values specify bends in the x-z-plane and negative values specify bends in the y-z-plane.

The low influence of the bend direction can be explained by the small ratio between pitch and hole diameter ratio of $\Lambda/d = 1.23$ of this fiber which leads to a narrow bridge width of $w_b = \Lambda - d = 8.1$. The direction of the bend with respect to the hole structure is unknown for the measured data (black closed symbols) and only marked on the positive side. A Gaussian beam was coupled into the fiber (collimation f = 8.0 mm, focusing f = 45 mm) and a beam propagation factor of $M^2 = 1.48$ was measured after the fiber. This M^2 value suggests that both modes (LP_{01} and LP_{11}) are excited inside the fiber.

Hence, the measured losses are supposed to be in between the calculated losses of the LP_{01} and the LP_{11} modes. But the measured losses are higher than expected from these simulations despite the fact that the produced fiber agrees well to the design. A possible explanation could be that because the structure is not asymptotically SM, the pitch to hole diameter ratio is small. As a result, surface scattering due to the roughness of the glass-hole-interfaces becomes a more important factor than in case of asymptotically SM LCF for which the dominant loss channel is the leakage due to the glass bridges (larger pitch to hole diameter ratio). The surface scattering cannot be included within the FEM simulations. This might explain why the simulations are underestimating the bending losses of this fiber. The attenuation of the fiber was measured with the cutback method at a high bending radius of about 1 m and was found to be less than 17.5 dB/km.

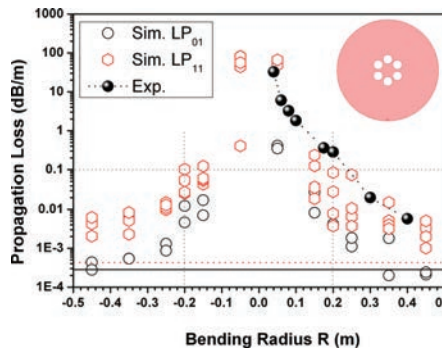

Figure 5.32: Bending losses of a LCF suitable to deliver the 2-times polarization degenerate fundamental LP_{01} mode and the 4-times degenerate LP_{11} mode. The open symbols correspond to the simulated results. Positive R values specify bends in the x-z-plane and negative values specify bends in the y-z-plane. For the measured results, the direction of the bend in reference to the hole structure is unknown and marked only on the positive side (black filled symbols).

5.3.8 Extended Leakage Channel Fiber Concept

During the investigation of leakage channel fibers it was noticed that this concept can be extended if a further parameter is considered. In addition to the bridge width w_b, a bridge length l_b can be introduced as shown in figure 5.33. Simple holes which are stabilized by pressure during the drawing process and therefore of round shape are not suitable as low-index inclusions in this case. The production of such fibers will therefore be problematic.
Nevertheless such an extended LCF is interesting because the losses can be adjusted by changing the new parameter l_b. Hence, the loss ratio can be increased by utilizing a high ratio of Λ/d which leads to unwanted high losses for the fundamental mode. But these losses can now be balanced by increasing the bridge length l_b. According to the FEM simulations, this can be adjusted in such a way that the LP_{11} mode is not core-guided while the LP_{01} mode experiences low losses even for very large cores. Hence, SM fibers with extremely large cores with diameters of more than 50 µm seem feasible.

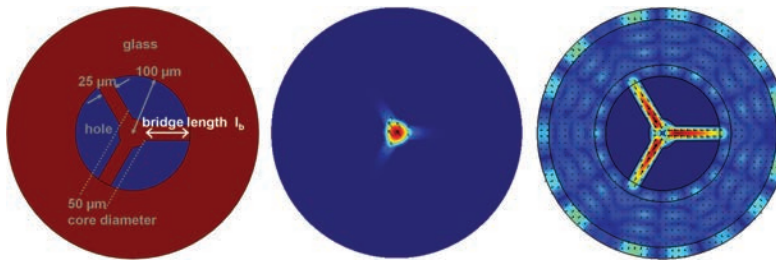

Figure 5.33: Scheme of an extended LCF concept. The losses of the fundamental mode can be adjusted by the bridge length l_b. The geometrical parameters of such an investigated fiber are indicated in gray. The calculated LP_{01} and TM_{01} modes corresponding to this parameters are shown.

The drawback of such a structure is a very high sensitivity to bends because of the large bridge width w_b necessary to prevent the guiding of HOMs. The bending losses cannot be compensated by the bridge length l_b, this can only be achieved for the losses of the straight fiber. Therefore, such fibers will not be of interest for flexible beam delivery, but the mode field areas of fiber lasers and amplifiers in a rod-type

configuration could be enhanced by such special LCFs which would enable a further power scaling of diffraction-limited laser sources.

Further simulations showed an unusual feature of this special type of LCF. Because of its 3-fold symmetry the LP_{21} mode does not exist and a LP_{31} mode is core-guided although the LP_{11} is not as can be seen form the pictures in 5.33 and 5.34. Furthermore, the LP_{01} mode is easily disturbed when the fiber with a core diameter of 100 µm is bent ($R = 0.1$) and a LP_{11}-like mode becomes the lowest eigenmode as shown in figure 5.34.

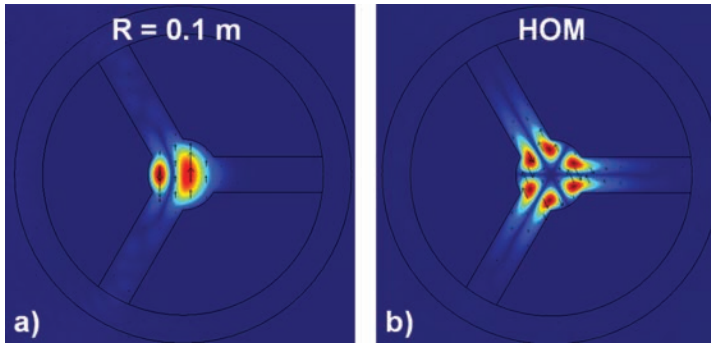

Figure 5.34: Lowest-order eigenmodes of the extended LCF concept (with geometrical parameters shown in figure 5.33) if the fiber is bent with $R = 0.1$m a). Because of the symmetry, the structure possesses a weakly core-guided LP_{31} mode b) but no LP_{21} mode.

Chapter 6

Fundamental Mode Transport in Multimode Fibers

As discussed in the previous chapters, imperfections of the glass, the geometry, or distortions such as fiber bends, stress, as well as nonlinear effects at high intensities, will influence the eigenmodes and lead to mode coupling and hence energy transfer between them.

As shown in chapter 2.4, a phase matching condition (2.73) has to be fulfilled to allow mode coupling. Any disturbance along the fiber can effectively couple two modes only if it has a significant spatial Fourier component which matches the propagation constants of the two modes.

If the difference $\Delta\beta_{12} = |\beta_1 - \beta_2|$ is large enough, the usual disturbances like geometry changes, fluctuations of the refractive index, or fiber bends are changing too slowly to cause an efficient mode coupling. This means, that the difference (of the real parts) of the propagation constants or equivalently the difference of the effective refractive indices

$$\Delta n_{\text{eff}} = |n_{\text{ef}1^1} - n_{\text{eff}^2}| \ , \tag{6.1}$$

which specifies the *mode spacing* between the modes, defines how likely they will exchange energy due to a perturbation.

Therefore, one can conclude that it could be sufficient to use fibers with a high mode spacing instead of (asymptotically) SM fibers to transport a SM beam in a MM fiber. For all kinds of fiber structures investigated and presented in this work the mode spacing decreases with increasing core size which prevents the use of arbitrarily large cores. However, a specific minimum value for Δn_{eff} is a less critical requirement than

demanding an (asymptotically) SM large mode area fiber. The question is how large the Δn_{eff} has to be in order to avoid mode coupling and thereby maintain the beam quality during the beam transport. The limit of a scaling of the fiber core size and hence the effective mode area of the fundamental mode depends on the minimal acceptable Δn_{eff}.
From the birefringence of commercially available polarization maintaining fibers it can be deduced that with $\Delta n_{\text{eff}} \approx 5 \times 10^{-4}$ polarization mode coupling is efficiently suppressed. Furthermore, J.M. Fini and S. Ramachandran stated [55] that the mode coupling can usually be neglected if

$$\Delta n_{\text{eff}} > 1 \times 10^{-4} \tag{6.2}$$

which is used as a reference value in the following sections.

6.1 Fundamental Mode Transport in Multimode Step Index Fibers

Step index fibers are the natural choice for MM fibers because of their low attenuation. Commercially available passive fibers with core diameters between 20 and 30 µm and NAs between 0.06 and 0.08, often referred to as large mode area (LMA) fibers (see chapter 2.6.1), support only a few modes. For the following investigations, such a fiber with 30 µm core diameter and a NA of 0.06 was purchased from the company Nufern (LMA-GDF-30/400). The fiber has a cladding diameter of 400 µm which gives mechanical strength to the fiber and reduces micro bending. The attenuation is specified to be $\alpha = 1.4\,\text{dB/km}$.
Simulations performed with COMSOL Multiphysics showed that this fiber supports 16 core-guided modes including polarization degeneracy. In comparison to the (asymptotically) SM fibers described so far, the coupling of a free space Gaussian beam to the fiber is more critical because HOMs are easily excited. Therefore, it was very important to optimize the coupling conditions to excite only the fundamental mode. This was achieved by measuring the beam propagation factors for different coupling conditions after a 10 m long fiber. The alignment was optimized for different collimation and focusing optics which led to the M^2 values shown in figure 6.1. When using a collimation package (*Thorlabs*) with a focal length of 8 mm, the best results were obtained with a focusing lens with 30 mm focal length

as indicated by the rectangles. A lower beam propagation factor of $M^2 \approx 1.12$ was obtained with a collimation package with a focal length of 15 mm in combination with a focusing lens with $f = 50$ m. This shows that a high beam quality could be maintained during the propagation inside the 10 m long fiber.
To improve the manageability and the reproducibility of the critical coupling conditions, the alignment of the free space beam to the fiber was automated using computer controlled axes as described in chapter 4.2.1 during the course of these measurements.

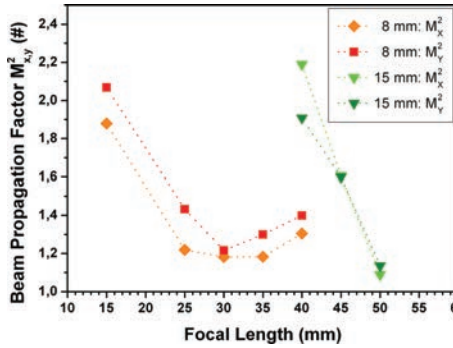

Figure 6.1: Beam propagation factor M^2 measured after the LMA-GDF-30/400. For each measurement different optics were used to couple the laser beam into the fiber. Two different lens combinations with $f = 15$ mm (triangles) and $f = 8$ mm (rectangles) were used to collimate the free space beam resulting in beam diameters of about 1.5 mm and 2.9 mm respectively before the beam was focused into the fiber with different lenses with $f = 15..50$ mm.

The power measured after the LMA-GDF-30/400 was 86.3% of the power from the laser source ($P_{out} = 0.863 \cdot P_{laser}$). A theoretical limit for the transmition efficiency was estimated by taking into account the reflection losses at the fiber-air (glass-air) interfaces and the losses resulting form the mode matching of laser beam, transfomed via the coupling optics, and the calculated fundamental mode of the fiber.
Assuming a perfect Gaussian laser beam and perfect alignment conditions as well as the correct knowledge of all fiber properties and parameters of the optics, a maximum power transmission efficiency of 92.5% was derived using an ABCD-matrix

formalism [26] and overlap integrals. Comparing this ideal limit to the measured 86.3% shows that the experimentally achieved transmission efficency, using the automated coupling setup, is remarkably high.

After the optimization of the coupling conditions the stability of the delivered beam quality was tested. This was done by comparing the beam propagation factors measured after the fiber was kept straight with the ones measured after a strongly bent fiber. Table 6.1 lists the measured M^2-factors for an experimental situation in which the 10 m long fiber is placed on the optical table with a large radius ("straight") and in case a part of the fiber was bent into one loop with a radius of only $R = 0.04\,\mathrm{m}$. The measurements were performed in a row with no realignment. This means the M^2 was first derived at maximum bending radius, then the fiber was bent and the M^2 was measured again followed by a measurement at maximum radius, and finally the fiber was bent and measured again.

Fiber	M_x^2	M_y^2	M_{mean}^2
"straight"	1.19	1.13	1.16
bent 1 (R = 0.04 m)	1.16	1.10	1.13
"straight"	1.21	1.15	1.18
bent 2 (R = 0.04 m)	1.17	1.17	1.17

Table 6.1: Beam propagation factor M^2 obtained by several beam caustic measurements of a beam delivered by the LMA-GDF-30/400.

Even at such a tight bending radius of 0.04 m, only a very small change of the M^2 could be observed. The M^2-factor did not degrade (increase) when the fiber was bent. On the contrary, even a small decrease of the M^2 was measured at $R = 0.04\,\mathrm{m}$. This can be explained by a small amount of power already propagating in HOMs before the fiber was bent which is most likely because even at perfect alignment conditions the coupling of the free space beam to the fiber is accompanied by a small mode mismatch (as explained above). The excited HOMs are significantly stronger attenuated by fiber bends than the fundamental mode which is the reason for the lower M^2 value if the fiber is sharply bent.

In addition to the M^2 value, the NF pattern was observed with the help of a CCD camera while the fiber was bent or moved. The movement and bending did not lead to a change in the NF for bending radii larger than 0.1 m. The NF pattern

remained Gaussian. Even for very small bending radii (0.03-0.08 m) only the transmitted power decreased. A systematic investigation of the bending losses is shown in figure 6.2. No additional losses to the fiber attenuation were observed at bending radii $R > 0.1\,\mathrm{m}$. The results of two different simulations are indicated, one which takes into account the elasto-optical correction (equation 3.22) (blue circles) and one which does not (black circles). The measured losses (black filled symbols) converge to the results of the simulations only if the elasto-optical correction is included. For the simulations of the specialty fibers presented in the previous chapters an elasto-optical correction was not necessary to achieve an agreement between simulations and measurements.

The LMA-GDF-30/400 as well as the other investigated LMA fibers showed low attenuations and virtually no bending losses in the region important for industrial material processing which is usually $R > 0.2\,\mathrm{m}$. The influence of the fiber length

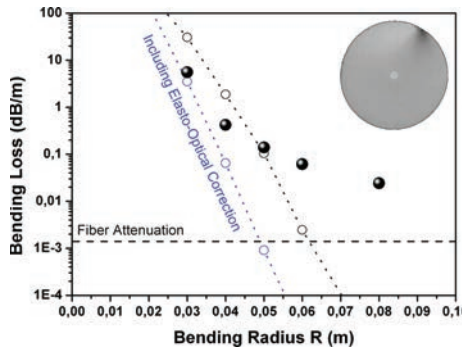

Figure 6.2: Measured (filled circles) and calculated (open circles) bending losses of the LMA-GDF-30/400.

of different LMA fibers on the delivered beam quality was investigated by several cutback measurements. The measurements revealed no change of the beam propagation factor M^2 over the available fiber lengths from 3 m to 20 m. From these investigations it can be concluded, that LMA step index fibers are good candidates for the delivery of 1kW continuous-wave diffraction-limited laser beams.

6.1.1 Investigation of the Bend-Induced Deformation of the Modes

In the course of the investigations of Bragg fibers, it was already mentioned that the bend-induced deformation of the modes in LMA step index fibers is comparably strong (section 5.2.2). If LMA step index fibers are considered for the delivery of high-power SM beams this should be examined in more detail.
The fundamental mode of commercially available LMA step index fibers is well confined unless the fiber is strongly bent as described in the previous section. But the simulations showed as well that the mode is deformed and the mode field area is reduced inside the bent sections of the fiber. According to 2.54 and 2.57 this decreases the threshold of the nonlinear scattering effects (see chapter 2.2.3).
To investigate this effect experimentally, a special fiber holder, on which the fiber can be placed with a constant curvature, was used to make the modes in bent fiber sections visible. This holder was introduced into the NF-FF-setup (chapter 4.2.2) to measure the NF. The fiber had to be precisely aligned to the fiber holder to ensure that a constant bend is applied until to the very end of the fiber. The fiber had to terminate precisely with the holder and the holder had to be aligned to the optical axis of the measurement setup to make the fiber end face perpendicular to this axis. The measured intensity pattern was then compared to the simulation results.
Figure 5.16 shows the calculated intensity distribution of the fundamental mode of a straight and a bent LMA-GDF-30/400 and the corresponding measured results. A normal v-groove holder, which keeps the fiber straight, and the special holder which applies a curvature of $R = 0.05\,\mathrm{m}$ was used. The color scheme from the simulation with COMSOL is different from the color scheme used by the software of the measurement setup, but the qualitative agreement between simulation and measurement is evident. The calculation of the effective mode area according to (2.41) gives a value of $485.4\,\mu\mathrm{m}^2$ for the straight fiber which is reduced to $386.3\,\mu\mathrm{m}^2$ if the fiber is bent with a radius of $R = 0.05\,\mathrm{m}$. This corresponds to a reduction of the MFA of 20.4% which can be problematic if the fiber is spooled. If the mode field area is reduced by 20%, the threshold for SBS and SRS is reduced by 20% as well according to equations 2.54 and 2.57.
A more detailed analysis of the intensity patterns showed that in case of the simulations the mode field diameter along the x-axis is reduced by 11.5% at $R = 0.05\,\mathrm{m}$.

This is higher than suggested by the measured results leading to a reduction of 6.8%. Along the y-axis, the simulations revealed a small reduction of the mode field diameter of about 4%, whereas the experimental results suggested a small increase. A possible reason for this difference might be the presence of a fraction of power in HOMs in case of the experiment. The HOMs reach further into the cladding leading to increased mode field areas compared to the simulations which considered all the power to be in the fundamental mode only. Another aspect already described in

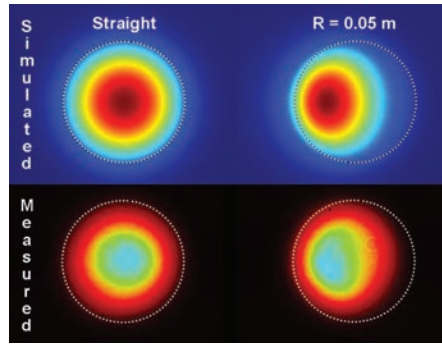

Figure 6.3: Bend-induced deformation of the fundamental mode of the LMA-GDF-30/400 if the fiber is bent with R = 0.05 m. The comparison between simulation and experiment shows a good agreement (color schemes are different for the simulation and experimental results).

chapter 4.1.2 becomes evident from figure 6.3. Because of the bend-induced change of the shape of the mode, it is important that the bends are applied in a way which makes the transition from straight fiber parts to the required bending radii smooth in order to avoid losses caused by the mismatch of the eigenmodes between straight and bent fiber parts.

Strong bending radii as considered in this section are often applied on active fibers, which are wound up on water cooled mandrels, but they can be avoided in passive beam delivery systems for material processing. If the bending radii are limited to values above 0.2 m, the reduction of the threshold of the nonlinear effects can be neglected for the fibers considered so far.

6.1.2 Investigation of the Mode Spacing

After the promising results of the detailed investigation of the low-NA LMA fibers, a high-NA MM fiber (referred to as SIF50/480) with an even larger core of 50 µm in diameter was examined. This fiber is commonly used for beam delivery in the field of material processing in combination with high-brilliance MM lasers with $M^2 \approx 6$. Its cladding diameter is 480 µm. The V-number of the fiber is $V = 32.9$ at a wavelength of 1050 nm resulting in more than 500 core-guided modes according to equation 2.42. However, according to FEM simulations the difference between the effective index of the LP_{01} and the LP_{11} mode is $\Delta n_{\text{eff}} = 1.46693 - 1.46682 = 1.1 \cdot 10^{-4}$ which would be sufficient for robust LP_{01}-mode propagation according to the criterion 6.2.

As for the low-NA LMA fibers, the experiments showed no decrease of the beam quality over several meters of propagation. The NF distribution was robust against fiber bends, but the measured beam propagation factors were between $M^2 = 1.3 - 1.5$. These higher values can be attributed to an excitation of more than just the fundamental mode when the beam was coupled to the fiber. Compared to the measurements with the low-NA fibers with smaller cores the free space to fiber coupling is even more critical because of the lower mode spacing and the high number of core guided modes. But it is likely that this can be improved with better coupling optics and improved alignment conditions in the future.

After these experimental investigations of fibers with core diameters up to 50 µm, the limit for SM beam transport in MM step index fibers according to the condition (6.2) was investigated with the help of simulations. By changing the core diameter and using different NAs several step index fibers were simulated in order to calculate the difference of the effective refractive indices of the corresponding fundamental modes and the HOMs. The calculated modes have been sorted and numbered according to their effective refractive indices for the representation of the Δn_{eff} in figure 6.4. The fundamental mode, as the mode with the highest refractive index, is denoted by #1, the LP_{11} by #2, and so forth.

The resulting nonuniform staircase-like pattern shows that the index differences of subsequent modes in step index fibers are irregular. The difference of the effective refractive index between LP_{01}, LP_{11} and LP_{02} are higher than the average mode spacing which is advantageous for the transport of laser beams containing only LP_{01} and/or LP_{11} modes.

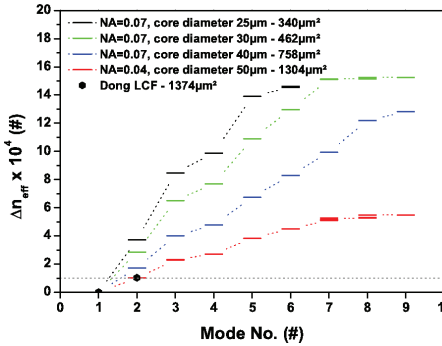

Figure 6.4: Difference of the effective refractive index Δn_{eff} between the calculated HOMs and the fundamental mode of different step index fibers. In addition, the simulation results for a LCF according to the parameters of [41] are indicated by black pentagons.

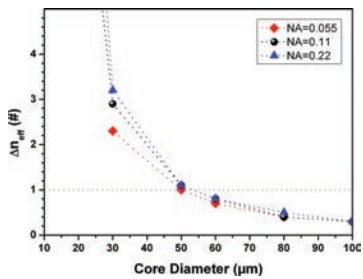

Figure 6.5: Calculated mode spacing Δn_{eff} of the LP_{01} and LP_{11} modes depending on the core diameter for three different NAs.

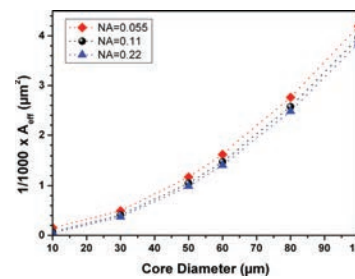

Figure 6.6: Calculated effective mode area A_{eff} depending on the core diameter for three different NAs.

If only the transport of the fundamental mode is desired, one can focus on the mode spacing Δn_{eff} between the LP_{01} and the LP_{11} mode. Figure 6.5 shows this mode spacing calculated for different core diameters of three fibers with numerical apertures of NA = 0.55 (red rectangles), NA = 0.11 (green circles), and NA = 0.22 (blue triangles). At a core diameter of about 50 µm, a Δn_{eff} of $1 \cdot 10^{-4}$ is reached for all three fibers. Larger cores lead to mode spacings which are too low according to condition (6.2). A higher NA results in a stronger confinement of the modes and therefore slightly smaller effective mode areas (A_{eff}) as shown in figure 6.6. As a consequence, the Δn_{eff} at a certain core diameter is larger for higher NA fibers as can be seen in figure 6.5.

6.1.3 High-Power Test of a Low-NA SIF

Because of the high transmission efficiency and the high beam quality experimentally achieved with the low-NA fiber with a core diameter of 30 µm presented in section 6.1 (LMA-GDF-30/400) a high-power beam delivery test was performed with a similar fiber produced at the IFSW. To increase the available power for this experiments, the fiber laser oscillator of the setup described in chapter 5.1.2.3 was improved by two amplifier stages. A passive step index fiber and a tapered fiber region were drawn from the same preform (supplied by *CeramOptec GmbH*) at the IFSW [64]. The approximately 500 mm long tapered fiber region was used to match the core diameter of the laser system with 20 µm to the core diameter of the passive transport fiber with 30 µm. The passive fiber had a cladding-to-core diameter ratio of 20 and a numerical aperture of 0.056. A M^2 value of 1.35 was measured after the beam delivery fiber of 100 m length at a transmitted power of 800 W [65].
The onset of Stimulated Raman Scattering (see chapter 2.2.3.3) was observed at output powers above 780 W indicated by a the spectral line at a Stokes-shifted (2.56) wavelength of 1140 nm as shown in figure 6.7. By comparing the measured M^2 value of only the laser source with the M^2 value obtained after the whole system, it can be concluded, that the passive transport fiber including splices and the tapered region deteriorated the M^2 value by less than 0.1. Further cutback measurements showed that less than 5% of the power is lost within the 100 m of transport fiber demonstrating the high efficiency of this beam delivery system.

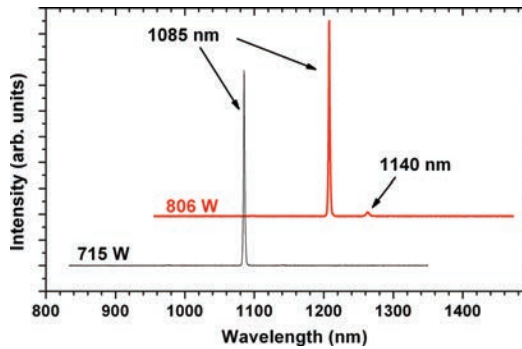

Figure 6.7: Spectral intensities after a passive beam delivery fiber (r_{co} = 15 µm, NA= 0.056) of 100 m length. At high output powers the onset of SRS, indicated by an small peak at 1140 nm, is observed.

6.2 Fundamental Mode Transport in a Multimode Multicore Fiber

LCF and photonic bandgap fibers are used because of their (asymptotic) SM behavior and it would not make much sense to consider such fibers in a MM regime. Multicore fibers on the other hand can efficiently be made MM because the light is guided by TIR. Therefore, it was investigated if MM multicore fibers can be used for SM beam delivery and how they perform in comparison to step index fibers.
A multicore fiber consisting of 7 Ge-doped cores with a diameter of 7 µm and a center-to-center distance of $\Lambda = 9\,\mu m$ was manufactured by the IPHT in Jena. The 7 cores are surrounded by pure silica glass, resulting in a numerical aperture of NA = 0.085 for each core. A picture of the fiber end face is shown as an inset in figure 6.9. The fiber guides a set of 14 supermodes (including polarization degeneracy). The approach was to excite the fundamental LP_{01}-like in-phase supermode and to investigate the mode mixing during the propagation in order to learn if such a structure can be used for high-brilliance SM beam transport.
First, the mode structure of this fiber was investigated theoretically. The mode with the highest effective refractive index is the in-phase supermode with 2 degenerate linear polarization states and a bell-shaped intensity distribution as shown in figure 6.8. The next type of modes are ring-shaped with axially symmetric (azimuthal, radial) and hybrid polarization followed by 4 ring-shaped modes of more complex polarization states. The 11th and 12th mode are linearly polarized modes with a π phase shift between the center core and the 6 surrounding cores (LP_{02}-like). Due to the 6-fold rotational symmetry of the fiber structure, LP_{2n}-like modes with 4-fold symmetry do not appear and the highest guided modes are LP_{31}-like modes.
Experimentally, the coupling of a free space Gaussian beam was optimized to couple preferably into the fundamental in-phase supermode with an effective mode area of $346\,\mu m^2$ at a wavelength of 1.05 µm. The theoretical overlap of this mode with a Gaussian distribution was calculated to be 92.55%. Even under perfect conditions $1-0.9255^2 = 14.35\%$ of the power is not coupled to the fundamental supermode and possibly coupled to HOMs. Therefore, it was first investigated how to achieve the best possible beam quality. Different collimation and coupling optics were used to optimize the coupling into the in-phase supermode. The emission of the ASE source was coupled to the fiber with an efficiency of 85% with the help of a collimation

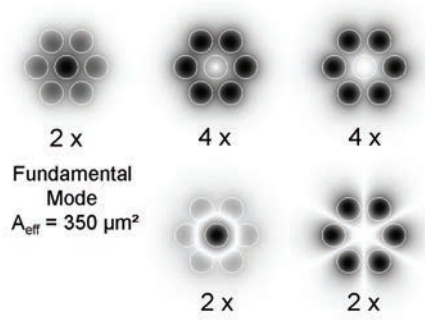

Figure 6.8: Simulated optical intensity of the supermodes of a 7-core fiber. The numbers indicate the polarization degeneracy.

package with $f = 8\,\text{mm}$ and a focusing lens with $f = 30\,\text{mm}$. The measured shape of the NF intensity distribution shown in figure 6.9 is close to one of the simulated in-phase supermode shown in figure 6.8.

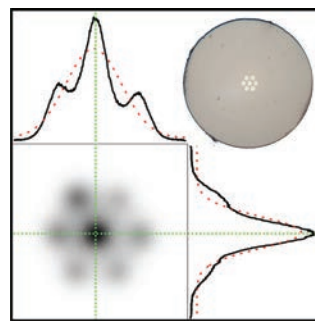

Figure 6.9: Measured NF intensity of the 7-core fiber. An image of the fiber end face is shown as an inset.

But the intensity in the 6 cores surrounding the central one is not distributed in a completely uniform way. However, the intensity in the central core is considerably higher then the intensity in the 6 surrounding cores as expected for the in-phase

supermode. The intensity distributions (black lines) along the two principal axes (green dotted lines) are superimposed with Gaussian fits (red dotted lines). Due to the segmentation of the core region and the comparably high NA of the individual cores the NF pattern considerably deviates form a Gaussian distribution.
The intensity in the different cores can be changed by changing the coupling conditions. For instance, it was possible to achieve a mode composition which results in a nearly equal intensity distribution over all 7 cores (see figure 6.11) simply by changing the position of the fiber end with respect to the focal point of the focusing lens (z-axis). Several measurements of the beam caustic were performed under different coupling conditions. If the transmitted power was maximized, beam propagation factors between $M^2 = 1.2$ and 1.4 were extracted from these experiments.
Figure 6.10 shows that the obtained M^2-values along the two main axes are different form each other as can be expected from the NF distribution. One of the axes intersects 3 cores, whereas the other intersects only the central core. As can be seen, the measured M^2-values were virtually independent of fiber bends which shows that bend-induced mode mixing in this fiber is negligible.
To obtain a theoretical M^2-value the FF distribution was calculated from the NF distribution obtained by the simulation with the help of the Kirchhoff integral (2.85). The diameters of these near- and far-field distributions were determined according to the 2nd moments method (2.84) from which a value for the M^2 of the in-phase supermode was calculated according to equation 2.83. As explained in chapter 5.1.2.1 the calculation is done for a finite domain. If the calculated region of the FF is chosen in a way that more than 99% of the power within the NF is captured within the calculated FF (less than 1% of the power is cut by the area used for the calculation of the FF) the theoretical M^2-values obtained along the main axes are 1.36 and 1.29. Comparing these values to the measured ones shows that the measured M^2-values are lower than the theoretical values. This is probably because the diffraction pattern of the measured FF was cut by the measurement setup (propably by the 1" optics/holders) and more than 1% of power was lost in the experiment. A situation similar to the one of the characterization of the 19-core fiber described in 5.1.2.1.
After the coupling conditions were optimized to maximize the intensity of the in-phase supermode, the power losses due to fiber bends were investigated. Figure 6.12 shows the measured bending losses of the 7-core fiber (filled symbols). Bending losses could not be observed for radii larger than 0.1 m.

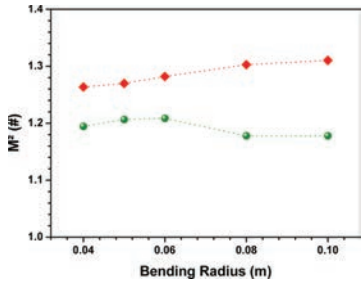

Figure 6.10: The M^2-factors determined in the two main axes after the 7-core fiber are largely independent of the bending radius R.

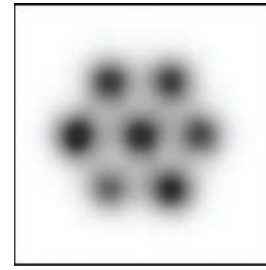

Figure 6.11: Mode mixture which leads to a nearly even intensity distribution in all 7 cores.

Strong bends down to $R = 0.04\,\mathrm{m}$ did result in bending losses, but they did not have a noticeable effect on the beam quality. A degradation of the beam quality during the propagation in fiber samples with lengths from 1 to 12 m was also not observed. Hence, the supermode is very well guided. The attenuation of the fiber was estimated to be 5 dB/km using the cutback method described in chapter 4.2.4.

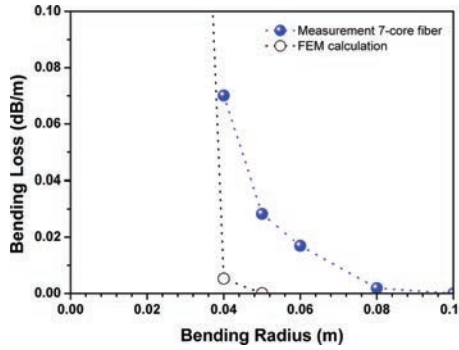

Figure 6.12: Measured (filled symbols) and calculated (open circles) bending-induced losses of the 7-core fiber.

6.2.1 Comparison of a 25/280 Low-NA SIF to the 7-Core Fiber

The characterization of the 7-core fiber revealed that the fundamental supermode propagates with low losses, and the beam quality is stable even if the fiber is moved or bent. These results are similar to those obtained for the SM transport in MM step index fibers. To investigate if there is a conceptional advantage of one of the fiber species in this context, appropriate fibers have to be found to make a meaningful comparison.

In case of the step index fibers a slightly smaller version of the 30/400 low-NA fiber (described in 6.1) with 25 µm core diameter is chosen because this fiber denoted as LMA-25/280 exhibits the same number of core-guided modes as the 7-core fiber. Furthermore, the mode field area of the fundamental (super)mode is the same for both fibers. Hence, the two fibers are ideally suited for a comparison.

The coupling of the free space beam into the fibers is again optimized to excite mainly the fundamental mode. Since their mode field areas are equal, the same coupling optics were used for both fibers. Using the ASE source, the beam propagation factors M^2 and the bending losses of both fibers were measured within the same measurement run. The obtained M^2 values were about 1.3 for both fibers.

The results of the measurements of the bending losses are compared in figure 6.13. The bending losses of both fibers are negligible for radii larger than $R = 0.1\,\mathrm{m}$. For radii below $R = 0.1\,\mathrm{m}$, their bending loss characteristics are very similar. Only for the lowest measured bending radii at $R = 0.03\,\mathrm{m}$ the values differ considerably, but because of the stiffness of the fibers it was difficult to measure very sharp bends and the reproducibility of this measurement point was lower. Therefore, the results at $R = 0.03\,\mathrm{m}$ have a higher uncertainty. Except for these values the bending losses of the 7-core fiber (blue pentagons) are similar to the losses of the LMA-25/280 (orange circles).

From the mode field areas, the M^2 values, and the bending losses it can be concluded that both fibers behave alike. In particular, an advantage of the multicore concept for the transport of SM beams with MM fibers was not observed. The theoretical overlap between the in-phase supermode of the 7-core fiber with a Gaussian distribution is about 92.55% and therefore lower as the overlap of a Gaussian distribution with the fundamental mode of the step index fiber which can be close to 100%.

In addition, the 7-core fiber is more difficult to produce and will in general have a higher attenuation due to the higher amount of interfaces. Hence, the step index fiber would be preferred as a delivery fiber for a Gaussian beam.
However, the measurements showed that both concepts can be used for an efficient transport of SM beams as long as the mode spacing (6.1) is high enough.

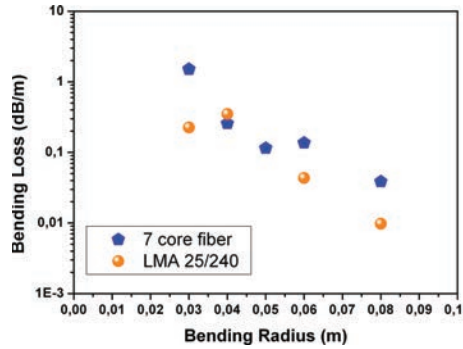

Figure 6.13: Comparison of the bending sensitivity of the 7-core fiber and a low-NA step index fiber (LMA-25/280). The fundamental modes of both fibers have the same mode field areas.

Chapter 7

Cylindrical Vector Modes in Fibers

Up to now, mainly the properties of the bell-shaped fundamental mode in (asymptotically) SM fibers and MM fibers were investigated. Only a few remarks on the polarization were made because the fibers discussed so far did not maintain the polarization of the light. Within this chapter cylindrical vector modes which are modes with spatially varying polarization and cylindrically symmetric intensity distribution are considered. The possible benefits of radially (TM_{0X}) and azimuthally (TE_{0X}) polarized modes are explained and the first experiments with such modes and step index fibers are reported.
Due to the limited time, this topic could not be investigated in full detail but it is described under which circumstances radial or azimuthal polarization states can be preserved during propagation in passive fibers and specialty fiber designs to transport such modes are proposed which could be the basis for further investigations in this field.

7.1 Advantages of Radially and Azimuthally Polarized Modes

In some applications it is advantageous to use HOMs with a ring-shaped intensity distribution and special polarization properties. Radial (TM_{01}) and azimuthal (TE_{01}) polarization states are interesting because the absorption coefficient depends on the polarization. Hence, metal processing can greatly benefit from such polarization states [14].
In particular, the lowest-order radial and azimuthal polarization states TM_{01} and

TE_{01} are promising because of their high focusability (low M^2 of about 2). These modes are not only investigated for their special polarization characteristics, their intensity distribution is of interest as well as described in the following. Figure 7.1 shows the intensity profile of a Gaussian beam in comparison with a ring shaped intensity distribution of an axially symmetric polarized beam (in this case cylindrically but azimuthally or radially could be used as well). According to second moments method (2.84) both have a beam diameter of 200 µm. As can be seen, the gradient of the intensity is steeper for the ring-shaped intensity distribution. Since a certain threshold intensity is needed to melt the processed material the ring-shaped intensity distribution is advantageous because less material which is not molten will be heated unnecessarily by the laser.

The calculated angle-dependent Fresnel absorption on a hot iron plate is shown in figure 7.2. The absorptivity strongly depends on the polarization for high angles of incidence (close to the normal incidence).

Weber *et al.* [15] demonstrated an increase of the cutting efficiency of up to 36 % and an increase of the maximum cutting speed of 37.5 % when processing stainless steel with a thickness of 2 mm with a radially polarized CO_2 laser. Furthermore, they observed a reduced spatter behavior for deep welds and an significant influence on the drilling efficiency using a solid-state laser with 1 µm wavelength and a radially polarized beam.

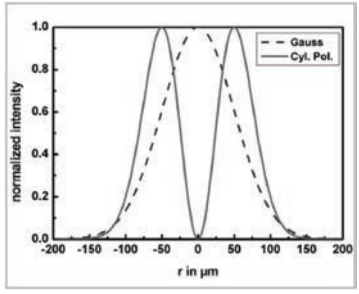

Figure 7.1: Intensity distributions of a Gaussian beam (dotted line) and a cylindrically polarized beam (solid line) [15].

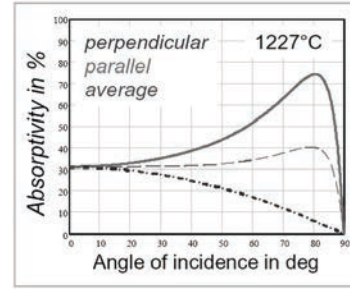

Figure 7.2: Fresnel absorptivity calculated for hot iron for parallel (p) and perpendicular (s) polarization [15].

To investigate the behavior of radially or azimuthally polarized modes in optical fibers experimentally, a special laser source is needed but most (commercially) available laser sources are either SM with a close to diffraction-limited (Gaussian) beam or MM with a flat-top beam profile. A linearly polarized beam can be transformed using segmented $\lambda/2-$wave plates [66] to obtain a beam that is mostly radially or azimuthally polarized. However, such vector modes can be generated directly by using special intra-cavity polarization shaping elements which is especially interesting for high-power lasers. Such elements were characterized, selected, and used to built the first radially polarized thin-disk laser [67] to investigate the possibility of using fibers for delivery of such modes as described in the following. Further informations about the polarizing elements (grating mirrors) and the special thin-disk laser are available in appendix 8.1.

7.2 Transport of a Radially Polarized Mode in a Step Index Fiber

As demonstrated in chapter 6, the fundamental mode may be well preserved within a MM fiber if the mode is properly launched and the difference of the effective refractive indices between the fundamental mode and the successive modes is sufficiently high. But the polarization state is not preserved in standard fibers and the measurements showed that the degree of polarization after the fiber strongly depends on the movement and the bending of the fiber. A birefringence as caused by strain is needed in order to make a fiber polarization maintaining.
A cylindrical strain distribution can be expected within cylindrically symmetric step index fibers due to the core-cladding interface [68]. Such a strain distribution will not lead to the preservation of linearly polarized light but it could maintain a mode with cylindrically symmetric polarization. To address this thought, a radially polarized mode was carefully injected into a LMA fiber (Nufern 25/400) with a core diameter of 25 µm and a NA of 0.07 and characterized with the NF-FF-measurement setup. Figure 7.3 shows the measured near- and far-field distributions of the laser beam after propagating for 10 m inside the fiber. Special care was taken to avoid strong bends of the fiber. The ring-shaped distribution is still visible but the intensity over the ring is not uniform. As for the NF, the intensity in the center of the FF vanishes.

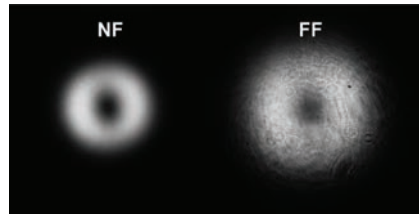

Figure 7.3: Near- and far-field intensity distributions after a 10 m long fiber with 25 µm core diameter and a NA of 0.07 if a radially polarized TM_{01} mode was coupled to the fiber.

A polarizer was introduced into the setup to analyze the polarization. Figure 7.4 shows the resulting NF distributions for three different analyzer settings. From the different intensities it can be concluded that the polarization is not purely radial. A polarimeter (see false color plot) was used to further investigate the local polarization on the ring. The fiber has been moved between the measurement with the analyzer in the NF-FF-measurement setup and the measurement with the polarimeter which influenced the polarization. The polarization ellipses show that the polarization state is far from being pure. A radial tendency is visible at positions where the intensity is high but in the lower intensity parts the local polarization is rather azimuthal than radial.

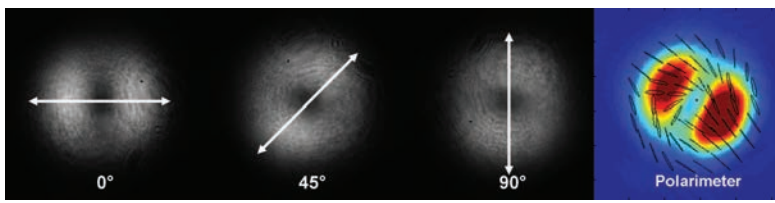

Figure 7.4: Distributions of the NF intensity at different analyzer settings are shown together with a false color plot obtained with a polarimeter to measure the local polarization. The measurements were performed after a step index fiber of 10 m length ($r_{co} = 12.5\,\mu m$, NA = 0.07) to which a radially polarized mode was coupled.

The symmetric ring-shaped intensity distribution of the eigenmode of the straight fiber is altered during propagation inside a fiber bend. The corresponding modes are LP_{11}-like as described in chapter 3.2.2.2 and shown by the simulation results in figure 3.5. The experiments showed that the transport of a radially polarized TM_{01} mode within the fiber results in a mixture of the four degenerated HE_{21} (2x), TE_{01}, TM_{01} modes which leads to a deformation of the intensity distribution. This is different to the case of a beam transport of a fundamental mode where the interaction of the two degenerated orthogonally polarized Gaussian-like modes led only to depolarization while the intensity distribution did not change. Here, the intensity distribution is altered as well.

7.3 Specialty Fibers for Radially and Azimuthally Polarized Light

In order to benefit from radially or azimuthally polarized laser beams on the workpiece specialty fibers, which preserve such polarization states, are needed. The degeneracy between the different polarization states has to be lifted by introducing a *radial-azimuthal birefringence*. The symmetry of the fibers combined with different materials used for the core and the cladding or a changing doping concentration (especially in gradient index fibers) will introduce a birefringence in virtually every fiber. However, as the previous results showed, this birefringence is not strong enough to ensure the preservation of the polarization. As a result, one has to increase the birefringence intentionally.

Within this work, special fiber structures with rad.-az. birefringence were developed and simulated with the FEM software. The "Plain-Stress" module of COMSOL Multiphysics was therefore combined with the "Hybrid-Mode Waves" module of the RF (radio frequency) package. With the knowledge of the stress-optical coefficients, the thermal expansion coefficients, and the Poisson's ratio, the influence of a temperature change on the stress distribution can be derived by applying the Young's modulus. For instance, if different materials are implemented in the fiber, such as stress rods made of diboron trioxide B_2O_3, a stress distribution can be calculated for a given temperature change. This distribution can then be used as input for the eigenmode calculation.

The main problem of such an approach is that the stress distribution in real fibers

is not a result of a temperature change from a temperature T_1 to a temperature T_2 but rather of the cooling of the liquid glass during the fiber drawing process. The liquid glass becomes solid, and a stress distribution is "frozen" inside the fiber. This stress distribution depends on the different material parameters, such as the softening and melting temperatures, the temperature distribution inside the glass, and basically all parameters of the drawing process. To make quantitative predictions, the materials and the drawing process would have to be examined in detail which is outside the scope of this work. In order to perform theoretical investigations of different fiber structures, it was therefore decided to mimic the stress elements by air holes with a certain pressure. It is well known that a pressure in the order of 1000 bar can be achieved in glass capillaries with micron sized holes without braking them. With this model it is possible to calculate the stress distribution of different configurations by introducing a reasonable amount of pressure.

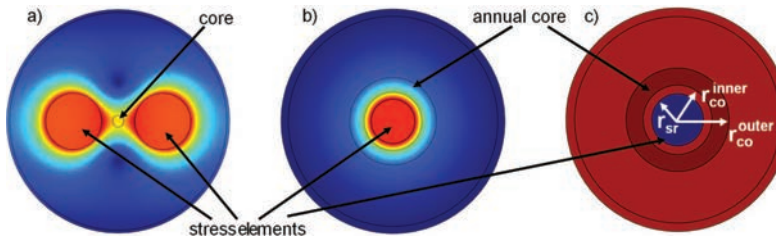

Figure 7.5: Calculated stress distribution (Tresca stress) of a Panda-type fiber a) and a fiber with a ring-shaped core and a central stress element b). A scheme of the structure with the central stress element is shown in c).

Figure 7.5 shows the calculated stress distribution of two kinds of fibers in false color plots. The first distribution a) results of the calculations of a polarization maintaining (PM) Panda-type fiber. Such fibers are commercially available to preserve a linear polarization for SM (or few modes of low order) beam transport. The simulation results for this type of fiber were in good agreement with the available measurement data. The second structure b) exhibits a central stress element. The high refractive index core is a ring around this element separated by a thin low-index cladding. In both cases the stress elements are approximated within the simulation by holes filled with air with a pressure of 1000 bar.

As can be seen, a fairly homogeneous distribution over the area of the core can be achieved in Panda-type fibers with large stress elements and a comparably small core. Linearly polarized light properly injected to one of the main polarization axis of the fiber maintains its state of polarization with different phase delays between the slow and the fast axis. The phase delay $\Delta\phi$

$$\Delta\phi = (\beta_v - \beta_h) \cdot L = \Delta\beta \cdot L \tag{7.1}$$

is proportional to the length of propagation L and the difference of the propagation constants of the two orthogonally polarized modes (β_h, β_v).
The phase relation is restored after integer multiples of a certain distance called polarization beat length L_b

$$L_b = \frac{\lambda}{\Delta n_{\text{eff}}} \,. \tag{7.2}$$

With this relation the difference of the effective refractive indices can be obtained by measuring the beat length of the fiber. In commercially available polarization maintaining (PM) fibers, the beat length is a few millimeters. For $L_b = 2\,\text{mm}$ and $\lambda = 1\,\mu\text{m}$, the effective index difference becomes $\Delta n_{\text{eff}} = 5 \cdot 10^{-4}$ (e.g., Corning PM980). This difference prevents polarization mixing between the slow and the fast axes, so that the polarization is preserved if the light is properly launched.
The situation is equivalent to the mode mixing in MM fibers discussed in chapter 6. A difference of the effective refractive indices between the modes in the order of 10^{-4} was sufficient to preserve the beam quality of the fundamental mode. It is straight forward to postulate similar requirements for the cases of azimuthally or radially PM fibers. However, this situation is more complex. To propagate such modes the fiber has to be multimode because in any realistic case the fundamental fiber mode is linearly polarized (even when the fiber core has the shape of a ring).
To maintain the TE_{01} or the TM_{01} mode, the mode mixing with the fundamental mode HE_{11} and the HOMs has to be avoided. Furthermore, crosstalk between the polarization states has to be prevented. Unlike in the case of linear polarization there are not two but four possible polarization states: azimuthal (TE_{01}), radial (TM_{01}) and two modes with hybrid polarization (HE_{21}). Without rad.-az. birefringence the four polarization states are (near-) degenerated. The tiny difference of n_{eff}, resulting from the reflection differences at the core-cladding-interface of different polarization states, is usually negligible. However, in presence of rad.-az. birefringence the (near-) degeneracy is broken and the effective refractive indices of the two modes

with hybrid polarization are usually in between the n_{eff} of the radially and the azimuthally polarized modes. Therefore, the constraints for the robust transport of a TE_{01} mode in an optical fiber can be summarized as:

- $n_{\text{eff}}(\text{HE}_{11}) - n_{\text{eff}}(\text{TE}_{01}) > \Delta n_{\text{min}}$ (Condition 1)
- $|n_{\text{eff}}(\text{TE}_{01}) - n_{\text{eff}}(HE_{21})| > \Delta n_{\text{min}}$ (Condition 2)
- $|n_{\text{eff}}(\text{TE}_{01}) - n_{\text{eff}}(\text{HOMs})| > \Delta n_{\text{min}}$ (Condition 3)

with $\Delta n_{\text{min}} \approx 1.0 \cdot 10^{-4}$. By changing the arguments from TE_{01} to TM_{01} one obtains the conditions for the transport of the lowest-order radially polarized mode.

7.3.1 Using a Central Stress Rod

The simplest way to introduce a rad.-az. birefringence is shown in figure 7.5c). Only one stress rod is used in the center of the fiber surrounded by a high-index core which can be separated from the stress rod by a thin low-index cladding to avoid losses introduced by the higher absorption of the stress rod. The ring-shaped core is enclosed by low-index cladding to confine the light and to give mechanical strength to the fiber.
A series of simulations were performed with different sizes of the stress rod (emulated by an air hole with 1000 bar pressure) and different thicknesses of the core. The simulations showed that in this kind of fiber the fundamental mode is a linearly polarized ring-shaped mode. While it is straight-forward to reach to the first two conditions mentioned above by limiting the core area, it is rather difficult to fulfill the third condition. The reason is that, unlike in the Panda-type case, the stress profile is strongly inhomogeneous over the core area. The strength of the birefringence is rapidly decreasing with the distance from the stress element. The presence of the hybrids modes (HE_{21}) leads to additional complications because of their lower sensitivity to the rad-az birefringence.
Therefore, the ring-shaped core has to be close to the stress rod, the inner cladding has to be thin, and a large NA is required to separate the light from the stress element. In further simulations the thickness of the layer separating the core from the stress rod ($r_{co}^{inner} - r_{sr}$) was fixed to 1 µm and the NA to 0.22 while the radius of the stress rod r_{sr} and the thickness of the core region (r_{co}^{outer}) were changed.

The simulations showed that if the core region is made thin but with a high diameter to maximize both, the core area and the effective rad.-az. birefringence, the third condition is still problematic. Thin ring-shaped cores lead to a high number of modes with simple ring-shaped intensity distributions but complex polarization configurations. The difference of the effective mode indices of the TE_{01} or TM_{01} to those of these HOMs is therefore critical. According to the simulations the application of this kind of structure is limited to mode field areas below $150\,\mu m^2$ due to condition 3.
Using a ring-shaped stress element around a circular core (opposite configuration) does not lead to a rad.-az. birefringence inside the core because all forces cancel each other. As a result, there seems to be no configuration (with several stress rods, or combinations of stress rings and stress rods) which leads to a more homogeneous az.-rad.-stress distribution over the core region.

7.3.2 Using a Special Doping Variation in the Core

Another approach for the introduction of a rad.-az. birefringence without the use of stress elements could be the change of the doping concentration over the core area. In gradient index fibers the doping concentration changes gradually and causes rad.-az. birefringence. Because of the symmetry of the problem the rad.-az. birefringence has to vanish in the center of the fiber. The maximum birefringence appears at the core-cladding interface, and in parabolic profile fibers the birefringence increases parabolically from the center to this interface [68]. The fiber production process is usually optimized to minimize this birefringence.
In case of step index fibers, the rad.-az. birefringence introduced by the core-cladding interface decays rapidly with increasing distance to this interface. However, one could try to maximize the birefringence by using different dopants in a way that the resulting refractive index distribution is still flat ($n_{co}(r) = n_{co}$) but the gradient of the birefringence (decrease from the core-cladding interface to center of the core) is reduced; thereby enhancing the influence of the birefringence on the mode structure. In this case the birefringence is related to the nanoscale doping concentrations. Light with a wavelength of about $1\,\mu m$, propagating inside the fiber core, will experience a smooth variation. Therefore, the birefringence can be implemented directly in the permittivity tensor ϵ.

In a cylindrical coordinate system the permittivity including a rad.-az. birefringence can be written as a diagonal tensor

$$\hat{\epsilon}^{cy} = \begin{pmatrix} \epsilon_{rad} & 0 & 0 \\ 0 & \epsilon_{az} & 0 \\ 0 & 0 & \epsilon_z \end{pmatrix} . \tag{7.3}$$

This tensor has to be transformed to the Cartesian system of the FEM-simulation by

$$\hat{\epsilon} = \hat{R}\hat{\epsilon}^{cy}\hat{R}^{-1} . \tag{7.4}$$

With the transformation matrix $\hat{R}$ shown in 3.19 the permittivity in the Cartesian basis can be written as

$$\hat{\epsilon}^{r\phi} = \begin{pmatrix} \cos(\phi)^2\epsilon_{rad} + \sin(\phi)^2\epsilon_{az} & \sin(\phi)\cos(\phi)(\epsilon_{rad} - \epsilon_{az}) & 0 \\ \sin(\phi)\cos(\phi)(\epsilon_{rad} - \epsilon_{az}) & \sin(\phi)^2\epsilon_{rad} + \cos(\phi)^2\epsilon_{az} & 0 \\ 0 & 0 & \epsilon_z \end{pmatrix} .$$

This expression was implemented in the geometrical subdomains of the fiber in the FEM-simulation. With this approach, step index and parabolic profile fibers were investigated theoretically. In both cases a birefringence increasing parabolically from zero in the center to a fixed maximum of $\eta = 5 \cdot 10^{-4}$ (which is close to the to point when the fiber would become fragile) at the core-cladding interface was assumed.
A suitable expression for ϵ_{rad} is therefore

$$\epsilon_{rad}(r_{\text{core}}) = (n_{\text{core}} + \frac{\eta}{r_{\text{core}}^2} \cdot r^2) \cdot \sqrt{(1 + 2r \cdot cos(\phi)/R)}^2 \tag{7.5}$$

where r and ϕ are the polar coordinates and η ($= 5 \cdot 10^{-4}$) is the maximum birefringence at the core-cladding interface.
It was not investigated how such a birefringence could be achieved experimentally. The goal was to investigate if such an approach could work in principle by assuming an idealized fiber with a reasonable amount of rad.-az. birefringence.
The results of the simulations showed that with these special conditions it is possible to achieve radially PM fibers with core diameters up to 30 µm at a fixed NA of 0.22. The calculated effective index differences between the ring-modes are $n_{\text{eff}}(\text{HE}_{21}) - n_{\text{eff}}(\text{TM}_{01}) = 1.0 \cdot 10^{-4}$ and $n_{\text{eff}}(\text{TE}_{01}) - n_{\text{eff}}(\text{TM}_{01}) = 1.8 \cdot 10^{-4}$ at a core diameter of 30 µm. The index differences between these modes and the fundamental mode are considerably higher ($> 2.0 \cdot 10^{-4}$) in this case. The same is

true for the index differences to the subsequent HOMs. The effective mode area for the TM_{01}-mode is about $500\,\mu m^2$ which would be sufficient for the delivery of a radially polarized continuous-wave beam with a power of 1 kW. Figure 7.6 shows the calculated intensity distributions of the TE_{01} and the TM_{01} mode. If the rad.-az. birefringence is included into the simulations, the bent fiber exhibits radially and azimuthally polarized eigenmodes. Their intensity distribution gets slightly deformed by the bend but the distribution is still ring-shaped and their polarization is maintained. Without birefringence the corresponding eigenmodes of the bent fiber are linearly polarized LP_{11} modes. TE_{01} and TM_{01} modes are not present. Therefore, a properly injected TE_{01} or TM_{01} mode can only be preserved in a flexible fiber if a sufficient rad.-az. birefringence is present.

But there is another possibility to separate TE_{01} and TM_{01} modes without the need for strain or birefringent optical media which is explained in the following.

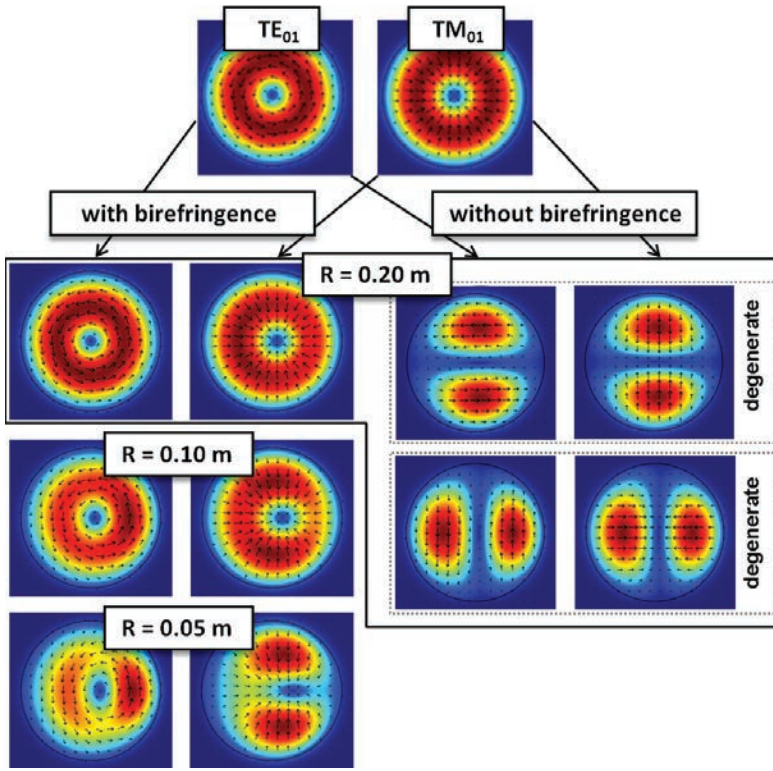

Figure 7.6: Calculated intensity distributions of the TM_{01} and TE_{01} modes and their modifications if the fiber is bent with a radius R. In presence of radial-azimuthal birefringence (here max. $5 \cdot 10^{-4}$ at the core-cladding interface) the modes are maintained which is not the case without birefringence.

7.3.3 Using High Refractive Index Steps

A third approach to maintain radially and azimuthally polarized modes in flexible fibers is based on geometrical considerations and the fact that the Fresnell equations [17] are polarization dependent which leads to different effective mode indices for the TE_{01} and the TM_{01} mode. This effect can usually be neglected (see weakly guiding approximation (2.40)) in step index fibers because the difference is very small.

However, if the refractive index difference between core and cladding becomes larger, this effect may be important. Since the goal is to propagate a ring-shaped mode, a ring-shaped core can be used. It has the advantage of an inner and an other interface which provides the possibility to maximize the polarization dependence.
This intuitive method proves correct by a more theoretical approach given by Ramachandran *et al.* [69]. If the modes are calculated analytically with the help of the weakly guiding approximation (2.40), vector corrections [18]

$$\delta\beta_{\mathrm{TE}_{01}} = 0 \,, \tag{7.6}$$

$$\delta\beta_{\mathrm{TM}_{01}} = -2(\delta_1 + \delta_2) \,, \tag{7.7}$$

$$\delta\beta_{\mathrm{HE}_{21}} = \delta_2 + \delta_1 \,, \tag{7.8}$$

with

$$\delta_1 = \frac{\Delta n_{\max}}{2r_{\mathrm{core}}^2\beta} \int rE(r) \cdot \frac{\partial E(r)}{\partial r} \cdot \frac{\partial(\Delta n(r)/\Delta n_{\max})}{\partial r} dr \tag{7.9}$$

$$\delta_2 = \frac{\Delta n_{\max}}{2r_{\mathrm{core}}^2\beta} \int E^2(r) \cdot \frac{\partial(\Delta n(r)/\Delta n_{\max})}{\partial r} dr \tag{7.10}$$

can be used to account for the polarization error. Here $E(r)$ is the electric field of the scalar mode, $\Delta n(r)$ is the refractive index profile relative to an infinite cladding, and $\Delta n_{\max}$ is the maximum value of this function, typically the index of the core [18]. As shown by the different expressions, high values of δ_1 and δ_2 lead to larger polarization corrections to the propagation constant β and therefore to a larger separation of the different polarization states. Hence, a fiber which guides high fields ($E(r)$) and high field gradients ($\delta E(r)/\delta r$) at index steps will have a high separation of the effective mode indices of the TE_{01}, TM_{01} the HE_{21} modes. This implies that a waveguide which resembles the mode itself, here an annular core, is more suitable for maximizing the Δn_{eff} [69].
Simulations of fibers consisting of a central air hole (without pressure) surrounded by a high-index ring as a fiber core and a (low-index) pure silica cladding were performed. A fiber with a relatively small NA of 0.06 between the core and the other cladding resulted in the largest mode field area while closely matching the three conditions postulated for radially and azimuthally PM fibers.
Figure 7.7 shows the refractive index profile of this fiber. The resulting mode field area of the TE_{01} mode is about $280\,\mu\mathrm{m}^2$ at $1\,\mu\mathrm{m}$ wavelength. Simulations with higher NA or even two glass-air interfaces (i.e. with only an annular core) resulted

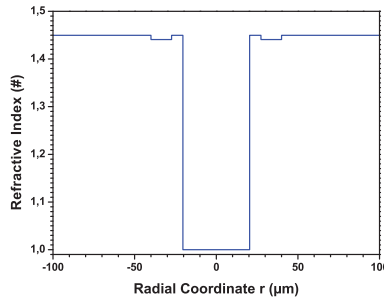

Figure 7.7: Refractive index profile of a fiber with central bore and a ring-shaped high-index region for TE_{01} mode preservation.

in lower areas. But the time for this kind of simulations was limited and further simulations might lead to optimized structures with even higher mode field areas. In summary, three different fiber concepts for radial and azimuthal polarization maintaining fibers were proposed. By parametric simulations a maximum mode field area of almost $150\,\mu m^2$ was obtained by a fiber with annular core and a central stress rod. A mode field area of about $500\,\mu m^2$ was achieved by the nanoscopic approach which assumed an ideal doping variation in the fiber core resulting in a flat refractive index distribution with a parabollically increasing rad.-az. birefringence. The third, geometrical approach, which used the dependence of the reflection on the polarization, led to a mode field area of about about $280\,\mu m^2$. All these values are considerably higher than the published result of [69] who demonstrated rad./az. polarization maintaining beam delivery experimentally.

Chapter 8

Summary

Various simulations and experiments were performed in order to reduce the nonlinearities in passive optical fibers for flexible laser beam delivery as well as in fiber lasers and amplifiers. Different fiber concepts were examined in view of large mode field areas for high brightness laser beams. The goal was to preserve an excellent beam quality and achieve a low bending sensitivity.

For theoretical investigations and for the design of suitable fiber structures, sophisticated methods were applied in order to use commercially available FEM software. By considering eigenmodes in fibers with piecewise constant curvature, the simulated models were reduced to two spatial dimensions reducing the numerical effort and making FEM simulations with sub-wavelength mesh elements possible. By introducing an artificial perfectly matched layer, the power losses of specialty fibers could be accurately calculated. Bending losses were simulated with the help of an equivalent refractive index model, and coordinate transformations were used to benefit from the symmetry of the fibers.

Specialty fibers produced at the IFSW as well as specialty fibers from commercial fiber suppliers were made to meet the custom specifications resulting from the optimization of the fiber parameters. Experiments to characterize the bending losses, the attenuation, and the beam quality of these fibers were performed. In order to improve the repeatability of the experiments, the coupling of a free space laser beam into the fiber was optimized by using automated computer-controlled high precision axes.

With the help of these measurements, it was demonstrated for the first time that several individual single-mode cores can be combined to a passive large mode area

fiber offering an excellent single-mode beam quality. Measurements of a multicore fiber (MCF) with 19 cores exhibited an $A_{\text{eff}} = 465\,\mu\text{m}^2$ and an beam propagation factor M^2 of about 1.03. This extremely low M^2 value could be explained by a small loss of power in the far-field which was cut by the used optics. Theoretical investigations showed that a far-field area containing 99.6% of the power of the corresponding near-field area results in a theoretical M^2 value which is consistent with the experimental value of 1.03.

The bending sensitivity of the 19-core fiber was close to the limit required for practical applications which required a careful handling of the fiber to avoid sharp bends. However, by restricting the bending radii and with the help of a tapered bridge fiber, a high-power test with 356 W (limited by the available laser source) was successfully conducted showing the high-power capabilities of this fiber. The rather strong bending sensitivity shows an analogy to step index fibers with a very low numerical aperture. Further investigations of a few-mode 7-core fiber and a step index fiber with an equivalent mode structure showed that such multicore and step index fibers behave in a similar way.

In conclusion, it can be stated that multicore fibers do not generally offer fundamental advantages over their step index counterparts. However, the multicore approach facilitates the manufacturing of large mode area single-mode fibers which are not reliably achievable with the state-of-the-art step index fibers. The segmentation of the core led to several cores with higher NA, which are easier to produce and less sensitive to fluctuations of the refractive index.

Furthermore, photonic bandgap fibers were investigated. The concept of asymptotically single-mode guiding was used to design and optimize large mode area Bragg fibers (BF). Simulations were successfully implemented and theoretical considerations led to an iterative optimization algorithm and an improved understanding of the influence of the cladding layers thicknesses on the optical properties of the fiber structure. However, the experimental results revealed some challenges. The produced BFs showed a decreasing beam quality with increasing fiber length in contrast to the expected asymptotic behavior. Power was constantly converted to lossy higher-order modes. Therefore, the overall transmission efficiency became low. This fact was attributed to a fluctuation of the refractive index in the center of the core. However, for short fibers (about 1-3 m) an extremely robust fundamental mode beam transport could be achieved. The optimized BFs were virtually free of bending losses

and showed a lower bend-induced mode field deformation when compared to step index fibers.

Another type of fiber which uses loss management, the leakage channel fiber (LCF) concept, was also examined. At first, a simple structure with 5 holes as cladding was designed. The fiber was produced at the IFSW and measurements revealed an effective mode area of $A_{\text{eff}} = 383\,\mu\text{m}^2$ and a beam propagation factor of $M_x^2 = M_y^2 = 1.1$. Due to production issues, the obtained attenuation of 22 dB/km was about 10 times higher than expected, but the attenuation of such LCFs was decreased with an improved production process. Further investigations showed the influence of additional cladding layers on the performance of LCFs. If the design is limited due to the bending sensitivity, increasing the number of layers is not sufficient to substantially reduce the losses for bends below a critical radius. However, by varying the hole sizes, from smaller holes in the inner microstructured layer to larger holes in a second layer, advantages in terms of bending sensitivity and differential losses could be achieved, leading to the possibility to further increase the effective mode area.

Additionally, the use of cladding resonances was investigated. By carefully designing the fiber diameter, the subsequent higher-order modes to the fundamental mode could be resonantly coupled to cladding modes. This approach, combined with a double layer microstructure with different hole sizes, led to a fiber design with 18 holes and a fundamental mode effective area of $708\,\mu\text{m}^2$. The produced fiber had a smaller core resulting in a smaller mode field area. A high beam quality with a beam propagation factor of $M^2 = 1.1$ was measured after the produced fiber and the attenuation determined by a cutback measurement was only 6 dB/km.

Since present high-power fiber amplifiers usually show a minor LP_{11} mode content, resulting in a beam propagation factor of about $M^2 \approx 1.2$, a LCF which efficiently guides the LP_{01} and the LP_{11} modes was designed to transport the whole power. The resulting fiber with a simple 6-hole cladding (LCF6) possesses a fundamental mode with a mode field area of $A_{\text{eff}} = 1187\,\mu\text{m}^2$. The beam propagation factor after the fiber was measured to be $M^2 = 1.48$.

Besides the comprehensive studies of (asymptotically) single-mode fibers, the possibility of the transport of a fundamental mode beam in multimode fibers was investigated. Based on the assumption that a large effective refractive index difference Δn_{eff} in the order of 10^{-4} would prevent mode coupling, and therefore allow fundamental mode beam transport, several step index fibers and a 7-core multicore fiber

were tested. In particular, a fiber with a core diameter of 30 µm and a NA of 0.06 (LMA-GDF-30/400) was intensively studied. When a Gaussian beam was carefully injected with suitable coupling optics, a high beam quality could be maintained. A beam propagation factor $M^2 \approx 1.12$ was obtained after 10 m of fiber even when the fiber was strongly bent or moved. Cutback measurements showed that the beam propagation factor did not change noticeably with the fiber length.

The NA of the fiber turned out to be high enough to prevent noticeable bending losses for bends with $R > 0.1$ m, but a bend-induced mode field reduction and deformation could be simulated and even measured by means of a fiber holder which was especially customized for this purpose. A similar fiber with a slightly lower NA of 0.056 was used for a high-power beam delivery test. A power of 800 W could be delivered over a 100 m long fiber. A M^2 of 1.35 was measured at this output power. Further calculations indicated that even a 50 µm core diameter would lead to a sufficient mode spacing for robust fundamental mode beam transport. Therefore, a fiber with 50 µm core diameter, and an ever higher NA, resulting in a V-parameter of 32.9 (at 1050 nm) which indicates 541 core-guided modes, was tested. As for the other large mode area fibers, the experiments showed no decrease in beam quality over several meters of fiber. The beam leaving the fiber was robust against fiber bends, but the measured beam propagation factors were between $M^2 = 1.3 - 1.5$. This was attributed to a more difficult excitation of only the fundamental mode and in consequence a higher-order mode content. This problem can be overcome by improving the coupling of the free space beam to the fiber.

Furthermore, the radially and azimuthally polarized modes were investigated. It turned out that neither the polarization nor the intensity distribution of axially symmetric vector beams is maintained in passive multimode step index fibers. Introducing a radial-azimuthal birefringence is obviously necessary for the preservation of such modes. In accordance with the case of fundamental mode beam delivery with multimode fibers, requirements for the use of radially and azimuthally polarized modes were proposed and the simulations were extended to calculate a stress-induced birefringence.

Three different fiber concepts for maintaining radially and azimuthally polarized modes were suggested. By parametric simulations a maximum mode field area of almost 150 µm^2 was obtained by a fiber with annular core and a central stress rod. A mode field area of about 500 µm^2 was achieved by a nanoscopic approach which

assumed an ideal doping variation in the fiber core resulting in a flat refractive index distribution with a parabolically increasing radial-azimuthal birefringence. The third approach used the dependence of the reflection on the polarization and led to a mode field area of about about 280 μm^2. These mode field areas are considerably higher than the values reported for radially and azimuthally polarization maintaining fibers in literature so far.

8.1 Outlook

It was demonstrated that the proposed high quality step index fibers, with a low attenuation and a high homogeneity over the whole fiber length, enable fundamental mode beam delivery in multimode fibers if the effective refractive index difference between the fundamental mode and higher-order modes is sufficiently high. Therefore, for lasers available now and in the near future, step index fibers are suitable for most applications. However, the core size can only be increased to a certain limit because the mode spacing is reduced with increasing core size. Consequently, the output power of single-mode lasers may increase to levels which cannot be managed by step index fibers.

The author believes that specialty fibers like MCFs and BFs will not play a major role in the context of beam delivery for material processing. But such fibers have their advantages as well. For special applications, where the stability of the beam quality is critical, but not the bending sensitivity, such as rod-type fiber lasers, optical sensing devices, or direct laser drilling, MCFs could be used because they offer the possibility to produce large mode area single-mode fibers. Or they could be used inside a laser cavity as mode filters. An active step index multimode fiber and a mode-matched piece of single-mode multicore fiber between two fiber Bragg gratings may be used to achieve a fully monolithic high-power fiber laser system with excellent beam quality. Bragg fibers on the other hand offer the possibility of an extremely low sensitivity to fiber bends and will have their special tasks as well. Special Bragg fibers for CO_2 lasers are already used for surgical applications. Applying the Bragg fibers discussed within this work to solid-state lasers with a wavelength of about 1 µm, these could be used for endoscopic or dental surgery as well.

The leakage channel fiber concept seems to be most promising because of its simplicity and its potential to couple core modes resonantly to cladding modes. The possibility to use loss management to prevent the coupling between core-guided modes is a further advantage of such fibers which is not yet well-known or used. Such structures may be used for active fibers with very high mode field areas as well, possibly combined with passive beam delivery LCFs, which will offer an alternative to present step index fibers.

After the improvement of the output power and the beam quality of industrial lasers in the past years, the creation of special modes is an active field of research today. The preliminary investigations of fibers for radially and azimuthally polarized modes are expected to be the subject of further investigations at the IFSW.

Appendix

A.1 Intra-Cavity Generation of Radial and Azimuthal Vector Beams

To directly generate axially symmetric vector beams, a laser resonator has to be optimized to the ring-shaped mode and it has to be polarization selective to favor either the TE_{01} or the TM_{01} mode. Within this work, a special microstructured end mirror was used to set up the first radial polarized thin disk laser. The polarizing effect is based on an intra-cavity reflectivity difference between the two orthogonal polarization states which is induced by a waveguide coupling mechanism between the incident free space beam and one (or two neighboring) leaky waveguide mode(s) in the multilayer mirror. In the case of axially symmetric polarization states, the required local reflectivity difference for TE-polarized and TM-polarized incident radiation is locally introduced by a circular grating.

A.1.1 Principles of the Polarizing Grating Mirrors

It is known that the coupling of free space radiation to waveguide modes caused by a grating is polarization selective since the phase matching condition, also called resonance condition [70], can only be satisfied for one polarization at a time and at a given angle of incidence and wavelength. This coupling condition is expressed by the following relation

$$n_{\text{eff}} = \sin\phi \pm m\frac{\lambda}{\Lambda} \tag{A.1}$$

where n_{eff} is the effective refractive index of the coupled mode (same as in the case for the guided modes of a fiber) which is depending on the polarization and the opto-geometrical parameters of the waveguide, ϕ is the coupling angle of incidence, m is the diffraction order, λ is the wavelength of the incident beam, and Λ is the

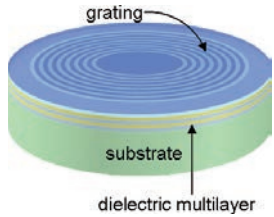

Figure A.1: Scheme of a microstructured mirror used for the generation of radial or azimuthal polarized modes.

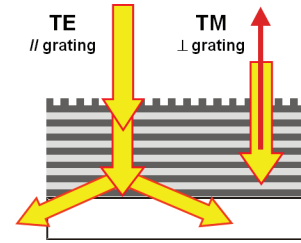

Figure A.2: Principle of the microstructured multilayer mirror which introduces a reflectivity difference for TE and TM polarized beams.

period of the sub-wavelength grating. The groove depth D of the grating does not affect the coupling condition but the coupling strength and therefore the reflectivity difference. Hence, using this mechanism to couple the incident free space beam to leaky waveguide modes of the dielectric multilayer mirror can lead to the desired polarization discrimination. In fact, this coupling is accompanied by a power leakage through the $\pm$ 1st diffraction order into the substrate as depicted in figure A.2. Consequently, by a proper design of the geometrical parameters (layer thicknesses, grating groove depth, and period) an intra-cavity reflectivity difference between the two orthogonal polarization states can be achieved at the wavelength of the laser [71, 67] to polarize it. In figure A.2 the TE polarization is filtered but the concept can be applied to TM polarization as well. Using a fully dielectric structure has the advantage that the element is suitable for high-power applications.

A.1.2 Characterization of the Polarizing Grating Mirrors

For the spectroscopic characterization of the fabricated structures, a reflectivity measurement setup, shown in figure A.3, was built according to the DIN EN ISO 13697 with a slight modification for its use under normal incidence [72]. A tunable laser diode (1000-1050 nm wave-length range) was used as a source. The collimated laser beam is cleaned using a single-mode polarization maintaining fiber in combination with a polarizing beam splitter with an extinction ratio of >10.000:1. An

optical chopper was used to modulate the laser signal. The modulation frequency f_1 provides the reference signal for the first lock-in amplifier (SR830 Stanford Research Systems). A 50/50 beam splitter redirects the beam which is alternately reflected from the chopper mirror and the sample under test to the integrating sphere. The frequency modulation f_2 of the chopper mirror provides the reference signal for the second lock-in amplifier (SR830 Stanford Research Systems). This differential measurement scheme, which uses a fast alternation between the reference signal reflected from the chopper mirror and the "unknown" signal reflected by the sample, reduces the sensitivity to intensity fluctuations of the laser beam. The detection of the signal was accomplished using a large area Si-photodiode (Hamamatsu S2386-8K) coupled to an integrating sphere.

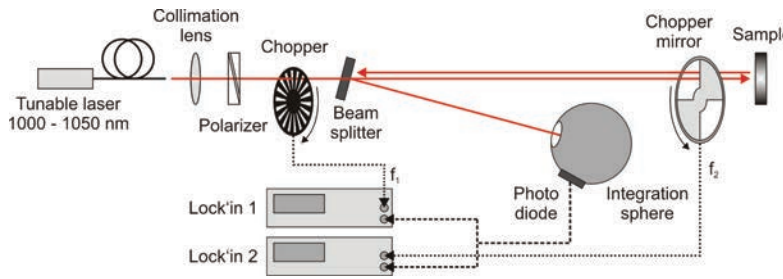

Figure A.3: Spectroscopic characterization setup built according to DIN EN ISO 13697 with modifications for its use under normal incidence.

Typical measurement results of TE (corresponding to the azimuthal polarization for the circular grating) and TM (corresponding to the radial polarization for the circular grating) reflection coefficients are shown in figure A.4. As expected, a decrease of the reflection coefficient for TE-polarization occurs around the central wavelength of the Yb:YAG disk laser. At 1030 nm, the reflection coefficients for the TE (azimuthal) and TM (radial) polarizations were measured to be $90 \pm 0.2\%$ and $99.8 \pm 0.2\%$ respectively. This is in good agreement with the modeling results (shown in figure A.4) and demonstrates the high reliability of this polarizing scheme. The slight deviation of the spectra can be attributed to the fabrication tolerances of the grating and the multilayer parameters.

An optimized design of such gratings could be achieved by etching in the fused silica

substrate rather than in the top layer. The geometry of the grating is then repeated in each single layer of the dielectric multilayer coating of the mirror.

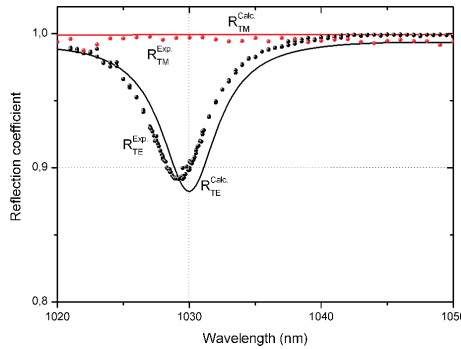

Figure A.4: Measured and calculated reflection coefficients of a grating with a period of 930 nm and of a nominal groove depth of 15 nm combined with a standard 29 quarter-wave layer dielectric mirror.

The potential advantages of this solution over the previously described design with the grating on top are the simple fabrication, especially in the case of SiO_2 substrate (standard etching process), lower scattering losses, and significantly broader fabrication tolerances. Figure A.5 shows that, with the new concept, even a reduction of the groove depth by 50% still leads to a more than 4 times broader bandwidth within the required reflectivity difference (i.e., $\approx 2\%$) for usage in thin disk lasers. In these examples, the calculated reflectivity for radial (TM) polarization of the lasing is not affected by the presence of the grating and still exceeds 99.9%. This broad spectrum significantly improves the fabrication tolerances which were found to be critical in the previous work with the old mirror design.

Figure A.6 shows a scanning electron microscope (SEM) image of the cross-section of a linear multilayer polarizing grating mirror where the good and conformal reproduction of the grating can be seen. Taking advantage of the multiple corrugation interfaces, caused by the grating etched into the mirror substrate, the coupling efficiency is enhanced. Since the polarizing mechanism is based on this coupling mechanism, power leakage into the substrate becomes more efficient. The amplitude of the effect is significantly larger than in the case with the grating applied to

the top layer only.

Since the polarizing mirrors are developed to be integrated in high-power laser systems where heating of the element is an issue, the spectral behavior of one fabricated linear polarizing grating mirror was analyzed at high temperatures. A leaky mode grating mirror (multiple-corrugated design) with a grating period of 930 nm and a grating depth of about 25-30 nm was heated using a Peltier element at the back side of the substrate.

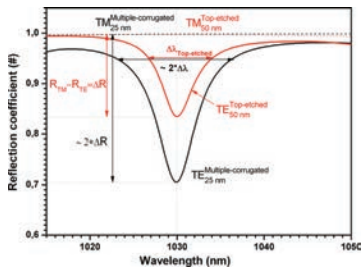

Figure A.5: Comparison of the calculated reflection coefficients for a top-etched and a multiple-corrugated structures with 50 nm and 25 nm grating depth respectively.

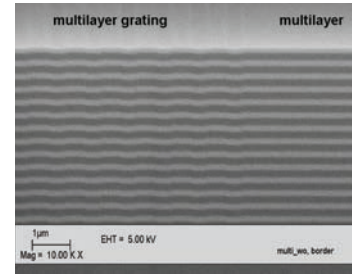

Figure A.6: SEM micrography of a multilayer mirror with a multiple-corrugated grating.

Figure A.7 shows the obtained results at temperatures of 21 and 134°C (respectively 21 and 126°C) for TE polarization (respectively TM polarization). The position of the dip indicating the polarizing effect is affected only slightly. A shift to longer wavelengths of about 8 pm/K was observed, proving the high stability of the present mirror design. Such a small shift can be explained by the compensation between the thermal expansion coefficients and the temperature dependence of the refractive indices of Ta_2O_5 and SiO_2 [73]. On the other hand, the reflection coefficient of TM-polarization is not affected when increasing the temperature of the sample up to 126°C. The functionality of the polarizing grating mirror element will not be affected even at the high temperatures associated with high-power laser systems.

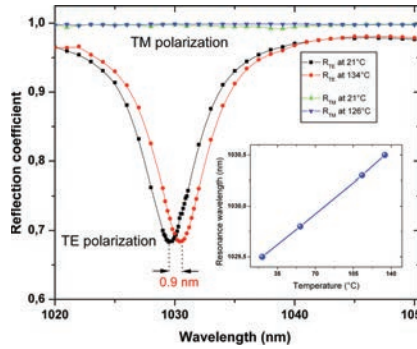

Figure A.7: Temperature dependence of the spectral response of the multiple-corrugated polarizing grating mirror. The inset shows the wavelength dip position depending on the temperature.

A.1.3 Intra-Cavity Radial Polarized Thin Disk Lasers

After the confirmation of the properties of the polarizing grating mirrors such a device, consisting of a grating with $\Lambda = 920\,\text{nm}$, a groove depth of 25 nm etched in the fused silica substrate, and 29 alternating Ta_2O_5 / SiO_2 layers (multiple-corrugated design) was introduced as the end-mirror of a V-shaped thin disk laser cavity (see scheme in figure A.8) [67]. In addition to the element the 421 mm long resonator, designed to operate in the TEM_{01}^* mode regime (corresponding to a TM_{01} mode in the fiber), comprises a 150 µm Yb:YAG disk and a 3% transmission output coupler. The radial polarization of the generated beam was confirmed by recording the intensity distribution through a linear polarizer used at different orientations. 10 W of radially polarized radiation was generated in a clean doughnut mode, as shown by the intensity distribution of the beam without polarizer in figure A.10 and the corresponding intensity distributions after the polarizer.

In comparison with the operation with an unstructured HR mirror, the output power obtained in radial polarization was $10\% - 15\%$ lower. Taking into account the 3% output coupling, this can be well explained by the reflectivity of the grating mirror which was about half a percent lower than the reflectivity of the unstructured HR mirror.

However, this was the first demonstration of a radially polarized Yb:YAG thin disk

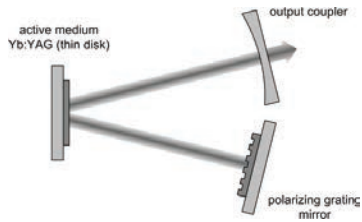

Figure A.8: Scheme of the V-shaped Yb:YAG thin disk laser resonator used for the generation of radially polarized light.

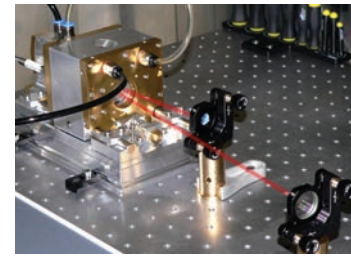

Figure A.9: Lab picture of the first radially polarized Yb:YAG thin disk laser.

laser. A lab picture of the device is shown in figure A.9. A new production method using a "Scanning Beam Interference Lithography" (SBIL) system [74], which works in polar coordinates, and the precise control of the complete process parameters during the production of the structures improved the quality of the gratings and allowed higher values of the reflection coefficients in comparison to the grating mirror used in the first laser. A fiber-coupled pump diode with 525 W maximum power at 940 nm and a 3.6 mm pump spot diameter was used together with a 215 µm thick Yb:YAG thin-disk (the curvature of the disk was measured to be $\approx$ 4 m at room temperature) and a plain output coupler with 4% transmission. The TEM^{*}_{01}-mode operation with $M^2 \approx 2$ was obtained by matching the diameter of the desired mode on the disk to the pump spot diameter, and by optimizing its length at full power which resulted in a 1.35 m long V-shaped resonator design.

A radially polarized doughnut-like mode (measured $M^2 \approx 2.3$ at full pump power) with up to 275 W power and an excellent optical-to-optical efficiency of 52.5% was generated with the polarizing mirror. Figure A.11 shows the intensity distribution of the beam and the degree of radial polarization measured by a 2D-polarimeter [75], revealing a high purity of more than $(98.5 \pm 0.5)\%$ of the radial polarization.

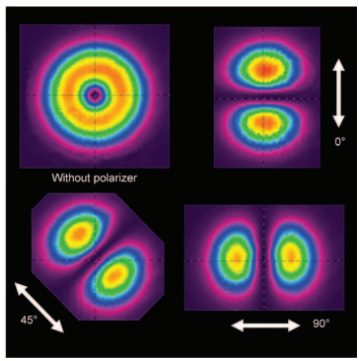

Figure A.10: Measured intensity distribution of the 10 W radially polarized laser beam with and without a linear polarizer at different orientations.

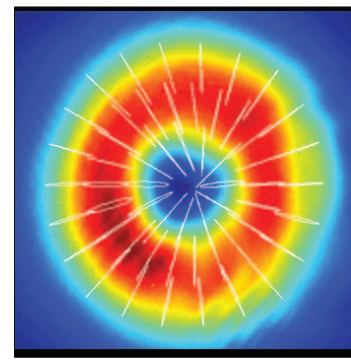

Figure A.11: Measured cross-section of the intensity and polarization distribution of a radially polarized thin disk laser with $P_{out} = 275\,\mathrm{W}$ [74].

Bibliography

[1] T. H. Maiman, "Stimulated Optical Radiation in Ruby," *Nature*, vol. 187, no. 4736, pp. 493–494, 1960.

[2] M. Douglas, "Theodore Maiman, 79, Dies; Demonstrated First Laser," *The New York Times*, 2007.

[3] K. C. Kao and G. A. Hockham, "Dielectric-fibre surface waveguide for optical frequencies," *Proc IEE*, vol. 113, pp. 1151–1158, 1966.

[4] W. Gambling, "The rise and rise of optical fibers," *IEEE Journal of Selected Topics in Quantum Electronics*, vol. 6, no. 6, pp. 1084–1093, 2000.

[5] F. P. Kapron, D. B. Keck, and R. D. Maurer, "Radiation losses in glass optical waveguides," *Conference on Trunk Telecommunications by Guided Waves*, vol. 17, no. 10, pp. 423–425, 1970.

[6] W. French, J. MacChesney, P. O'Connor, and G. Tasker, "Optical wave guides with very low losses," *Bell System Technical Journal*, vol. 53, no. 5, pp. 951–54, 1974.

[7] R. J. Mears, L. Reekie, I. M. Jauncey, and D. N. Payne, "Low-noise erbium-doped fibre amplifier operating at 1.54 μm," *Electronics Letters*, vol. 23, no. 19, p. 1026, 1987.

[8] C. Patel, "Selective Excitation Through Vibrational Energy Transfer and Optical Maser Action in $N_2 - CO_2$," *Physical Review Letters*, vol. 13, pp. 617–619, Nov. 1964.

[9] A. Giesen, A. Voss, and K. Wittig, "Scalable concept for diode-pumped high-power solid-state lasers," *Physics B: Lasers and*, vol. 372, pp. 365–372, 1994.

[10] H. Zellmer, A. Tünnermann, H. Welling, and V. Reichel, "Double-Clad Fiber Laser with 30 W Output Power - OSA Trends in Optics and Photonics Series," *Optical Amplifiers and Their Applications*, vol. 16, p. FAW18, July 1997.

[11] K. Contag, M. Larionov, and A. Giesen, "A 1-kW CW thin disc laser," *Selected Topics in Quantum Electronics, IEEE*, vol. 6, no. 4, pp. 650–657, 2000.

[12] Y. Jeong, J. K. Sahu, D. N. Payne, and J. Nilsson, "Ytterbium-doped large-core fiber laser with 1.36 kW continuous-wave output power," *Optics Express*, vol. 12, p. 6088, Dec. 2004.

[13] R. Stolen, "Nonlinearity in fiber transmission," *Proceedings of the IEEE*, vol. 68, no. 10, pp. 1232–1236, 1980.

[14] V. G. Niziev and A. V. Nesterov, "Influence of beam polarization on laser cutting efficiency," *Journal of Physics D: Applied Physics*, vol. 32, pp. 1455–1461, July 1999.

[15] R. Weber, A. Michalowski, M. Abdou-Ahmed, V. Onuseit, V. Rominger, M. Kraus, and T. Graf, "Effects of Radial and Tangential Polarization in Laser Material Processing," *Physics Procedia*, vol. 12, pp. 21–30, Jan. 2011.

[16] F. Mitschke, *Glasfasern: Physik und Technologie*. Spektrum Akademischer Verlag, 2005.

[17] W. Demtroeder, *Experimentalphysik 2: Elektrizität und Optik*. Springer Verlag, 2nd ed., 1999.

[18] A. W. Snyder and J. Love, *Optical Waveguide Theory (Science Paperbacks, 190)*. Springer, 1983.

[19] J. Senior, *Optical Fiber Communications: Principles and Practice*. Prentice Hall, 1992.

[20] J. Limpert, A. Liem, H. Zellmer, and A. Tunnermann, "500 W continuous-wave fibre laser with excellent beam quality," *Electronics Letters*, vol. 39, pp. 645–647, Apr. 2003.

[21] R. Dändliker, "Coupled waves: A powerful concept in modern optics," *Proc. SPIE 3190, Fifth International Topical Meeting on Education and Training in Optics*, 1997.

[22] D. Marcuse, "Steady-State Losses of Optical Fibers and Fiber Resonators," *The Bell System Technical Journal*, vol. 55, no. 10, pp. 1445–1462, 1976.

[23] D. Marcuse, *Theory of dielectric optical waveguides.* Quantum electronics–principles and applications, Academic Press, 1974.

[24] Z. Zhang, Y. Shi, B. Bian, and J. Lu, "Dependence of leaky mode coupling on loss in photonic crystal fiber with hybrid cladding.," *Optics Express*, vol. 16, pp. 1915–22, Feb. 2008.

[25] D. Marcuse, "Coupled power equations for lossy fibers.," *Applied Optics*, vol. 17, pp. 3232–7, Oct. 1978.

[26] T. Graf, *Laser: Grundlagen der Laserstrahlquellen.* Vieweg+Teubner Verlag, 2009.

[27] "Lasers and laser-related equipment - Test methods for laser beam widths, divergence angles and beam propagation ratios - Part 2: General astigmatic beams (ISO 11146-2:2005)," *ISO*, vol. 2005, 2005.

[28] A. E. Siegman, "New developments in laser resonators," *Proceedings of SPIE*, vol. 1224, pp. 2–14, 1990.

[29] W.-P. Huang, "Coupled-mode theory for optical waveguides: an overview," *Journal of the Optical Society of America A*, vol. 11, p. 963, Mar. 1994.

[30] P. Yeh, A. Yariv, and E. Marom, "Theory of Bragg fiber," *Journal of the Optical Society of America*, vol. 68, p. 1196, Sept. 1978.

[31] P. Russell, "Photonic crystal fibers.," *Science (New York, N.Y.)*, vol. 299, pp. 358–62, Jan. 2003.

[32] J. C. Knight, "Photonic crystal fibres.," *Nature*, vol. 424, pp. 847–51, Aug. 2003.

[33] S. Février, R. Jamier, J.-M. Blondy, S. L. Semjonov, M. E. Likhachev, M. M. Bubnov, E. M. Dianov, V. F. Khopin, M. Y. Salganskii, and a. N. Guryanov,

"Low-loss singlemode large mode area all-silica photonic bandgap fiber.," *Optics Express*, vol. 14, pp. 562–9, Jan. 2006.

[34] J. Blondy, B. Dussardier, and G. Monnom, "Very large effective area singlemode photonic bandgap fibre," *Electronics*, vol. 39, no. 17, pp. 1240–1242, 2003.

[35] M. A. Duguay, Y. Kokubun, T. L. Koch, and L. Pfeiffer, "Antiresonant reflecting optical waveguides in SiO2-Si multilayer structures," *Applied Physics Letters*, vol. 49, no. 1, p. 13, 1986.

[36] N. M. Litchinitser, A. K. Abeeluck, C. Headley, and B. J. Eggleton, "Antiresonant reflecting photonic crystal optical waveguides.," *Optics letters*, vol. 27, pp. 1592–4, Sept. 2002.

[37] P. S. Russell, "Photonic-Crystal Fibers," *Journal of Lightwave Technology*, vol. 24, pp. 4729–4749, Dec. 2006.

[38] "Hollow Core Photonic Bandgap Fiber for 1060 nm Range Applications HC-1060-02," *NKT Photonics GmbH*, www.nktphotonics.com.

[39] B. Temelkuran, S. D. Hart, G. Benoit, J. D. Joannopoulos, and Y. Fink, "Wavelength-scalable hollow optical fibres with large photonic bandgaps for CO2 laser transmission.," *Nature*, vol. 420, pp. 650–3, Dec. 2002.

[40] G. Vienne, Y. Xu, C. Jakobsen, H.-J. Deyerl, J. B. Jensen, T. Sorensen, T. P. Hansen, Y. Huang, M. Terrel, R. K. Lee, N. a. Mortensen, J. Broeng, H. Simonsen, A. Bjarklev, and A. Yariv, "Ultra-large bandwidth hollow-core guiding in all-silica Bragg fibers with nano-supports," *Optics Express*, vol. 12, no. 15, p. 3500, 2004.

[41] W. S. Wong, X. Peng, J. M. McLaughlin, and L. Dong, "Breaking the limit of maximum effective area for robust single-mode propagation in optical fibers.," *Optics Letters*, vol. 30, pp. 2855–7, Nov. 2005.

[42] L. Dong, T.-w. Wu, H. McKay, L. Fu, J. Li, and H. Winful, "All-glass large-core leakage channel fibers," *Selected Topics in Quantum Electronics, IEEE*, vol. 15, no. 1, pp. 47–53, 2009.

[43] M. Vogel, M. Abdou-Ahmed, A. Austerschulte, A. . Popp, B. Weichelt, T. Rataj, A. Voss, and T. Graf, "Multicore fibers for high-brilliance laser beam delivery," *Coherent Inc. Friday Seminar*, 2010.

[44] *COMSOL Multiphysics: Electromagnetics Module : User's Guide*. COMSOL, comsol 3.2 ed., 2005.

[45] J. Jin, *The Finite Element Method in Electromagnetics*. Springer Lehrbuch, Wiley-IEEE Press, 2002.

[46] K. Meyberg and P. Vachenauer, *Hoehere Mathematik: Differentialgleichungen, Funktionentheorie, Fourier-Analysis, Variationsrechnung*. Springer-Lehrbuch, Springer, 2006.

[47] J. Berenger, "Three-Dimensional Perfectly Matched Layer for the Absorption of Electromagnetic Waves," *Journal of Computational Physics*, vol. 127, pp. 363–379, Sept. 1996.

[48] S. D. Gedney, "An Anisotropic PML Absorbing Media for the FDTD Simulation of Fields in Lossy and Dispersive Media," *Electromagnetics*, vol. 16, no. 4, pp. 399–415, 1996.

[49] W. C. Chew and W. H. Weedon, "A 3D perfectly matched medium from modified maxwell's equations with stretched coordinates," *Microwave and Optical Technology Letters*, vol. 7, pp. 599–604, Sept. 1994.

[50] P. Viale, "Confinement Loss Computations in Photonic Crystal Fibres using a Novel Perfectly Matched Layer Design," *Proceedings of the COMSOL Multiphysics User's Conference 2005 Paris*, 2005.

[51] D. Marcuse, "Curvature loss formula for optical fibers," *Journal of the Optical Society of America*, vol. 66, p. 216, Mar. 1976.

[52] D. Marcuse, "Influence of curvature on the losses of doubly clad fibers.," *Applied Optics*, vol. 21, pp. 4208–13, Dec. 1982.

[53] D. M. Shyroki, "Exact Equivalent Straight Waveguide Model for Bent and Twisted Waveguides," *IEEE Transactions on Microwave Theory and Techniques*, vol. 56, no. 2, pp. 414–419, 2008.

[54] R. T. Schermer and J. H. Cole, "Improved Bend Loss Formula Verified for Optical Fiber by Simulation and Experiment," *IEEE Journal of Quantum Electronics*, vol. 43, pp. 899–909, Oct. 2007.

[55] J. M. Fini, "Intuitive modeling of bend distortion in large-mode-area fibers.," *Optics Letters*, vol. 32, pp. 1632–4, June 2007.

[56] I. H. Malitson, "Interspecimen Comparison of the Refractive Index of Fused Silica," *Journal of the Optical Society of America*, vol. 55, p. 1205, Oct. 1965.

[57] Y. Min, *To calculate PBG-guided mode in a periodic-cladding Bragg fiber*. Matlab code, 2006.

[58] C. Freitag, "Diplomarbeit: Automatisierung der Freistrahl-Faserkopplung zur Charakterisierung von Spezialfasern," 2011.

[59] T. Rataj, "Nichtlineare Effekte in optischen Wellenleitern," *IFSW Mitarbeitervortrag*, Nov. 2009.

[60] M. M. Vogel, M. Abdou-ahmed, A. Voss, and T. Graf, "Very-large-mode-area, single-mode multicore fiber," *Optics Letters*, vol. 34, no. 18, pp. 2876–2878, 2009.

[61] M. M. Vogel, T. Rataj, A. Austerschulte, A. Popp, M. Abdou-Ahmed, T. Liebig, A. Voss, and T. Graf, "Multicore fibers for high-brilliance laser beam delivery," vol. 49, pp. 772104–772104–11, 2010.

[62] H. Mckay, A. Marcinkevicius, B. Thomas, and M. Fermann, "Extending Effective Area of Fundamental Mode in Optical Fibers," *Journal of Lightwave Technology*, vol. 27, pp. 1565–1570, June 2009.

[63] R. Metselaar, *The production of nitrides and oxonitrides by carbothermal reduction nitridation*. 2009.

[64] A. Austerschulte, M. Vogel, T. Rataj, J.-P. Negel, A. Voss, and T. Graf, "800 W CW near diffraction limited beam delivery through a 100-m long multi-mode fiber," in *Fiber Lasers IX: Technology, Systems, and Applications*, vol. 8237-47, (San Francisco, California United States), pp. 8237–47, SPIE LASE, 2012.

[65] J.-P. Negel, A. Austerschulte, M. M. Vogel, T. Rataj, A. Voss, M. Abdou-Ahmed, and T. Graf, "Delivery of 800W of nearly diffraction-limited laser power through a 100m long multi-mode fiber," *Laser Physics Letters*, vol. 11, no. 5, p. 055104, 2014.

[66] G. Machavariani, Y. Lumer, I. Moshe, A. Meir, and S. Jackel, "Efficient extra-cavity generation of radially and azimuthally polarized beams.," *Optics Letters*, vol. 32, no. 11, pp. 1468–1470, 2007.

[67] M. A. Ahmed, A. Voss, M. M. Vogel, and T. Graf, "Multilayer polarizing grating mirror used for the generation of radial polarization in Yb:YAG thin-disk lasers.," *Optics letters*, vol. 32, pp. 3272–4, Nov. 2007.

[68] G. W. Scherer, "Stress-induced index profile distortion in optical waveguides: correction.," *Applied Optics*, vol. 19, p. 2656, Aug. 1980.

[69] S. Ramachandran, P. Kristensen, and M. F. Yan, "Generation and propagation of radially polarized beams in optical fibers.," *Optics Letters*, vol. 34, pp. 2525–7, Aug. 2009.

[70] O. Parriaux, V. A. Sychugov, and A. V. Tishchenko, "Coupling gratings as waveguide functional elements," *Pure and Applied Optics*, vol. 5, pp. 453–469, 1996.

[71] M. A. Ahmed, J. Schulz, A. Voss, O. Parriaux, J.-C. Pommier, and T. Graf, "Radially polarized 3 kW beam from a CO2 laser with an intracavity resonant grating mirror.," *Optics letters*, vol. 32, pp. 1824–6, July 2007.

[72] R. M. A. Azzam, "NIRSE: Normal-incidence rotating-sample ellipsometer," *Optics Communications*, vol. 20, no. 3, pp. 405–408, 1977.

[73] A.-K. Chu, "Multilayer dielectric materials of SiOX/Ta2O5/SiO2 for temperature-stable diode lasers," *Materials Chemistry and Physics*, vol. 42, pp. 214–216, Nov. 1995.

[74] M. A. Ahmed, M. Haefner, M. Vogel, C. Pruss, A. Voss, W. Osten, and T. Graf, "High-power radially polarized Yb:YAG thin-disk laser with high efficiency," *Optics Express*, vol. 19, no. 6, p. 5093, 2011.

[75] A. V. Th. Liebig M. Abdou Ahmed and T. Graf, "Novel multi-sensor polarimeter for the characterization of inhomogeneously polarized laser beams," vol. LASE, Photonics West, 2010.

Danksagung

An dieser Stelle möchte ich mich von ganzem Herzen bei all denjenigen bedanken, die mir diese Arbeit ermöglicht und meine wissenschaftlichen Untersuchungen unterstützt haben, oder mir in dieser Zeit beigestanden sind und so zum Erfolg dieser Arbeit beigetragen haben. Besonderer Dank gilt daher:

- Prof. Dr. Graf, der mir die Arbeit am renommierten IFSW mit seinen großen und gut ausgestatteten Labors sowie diese Dissertation erst ermöglicht hat. Sie haben diese Arbeit mit Ihren konstruktiven Anmerkungen und Fragestellungen immer weiter getrieben und verbessert.
- Prof. Dr. Herkommer, der mir mit seiner freundlichen und interessierten Art ein Zweitberichter war, dem ich meine Arbeit gerne näher gebracht habe.
- Dr. Voss, der mich in die Arbeitsgruppe aufgenommen hat und als unerschöpfliche Wissensquelle immer für Fragestellungen und Diskussionen bereit stand.
- Dr. Adbou-Ahmed der mich in die Welt der "sub-wavelength" Gitterwellenleiter eingeführt hat und mir stets mit Rat und Tat zur Seite stand.
- Meinen Studien- und Diplomarbeitern, D. Czurratis, S. Ried, F. Sterns, C. Thiel. und C. Freitag. Danke für Eure tatkräftige Unterstützung.
- Armin Austerschulte, ohne Deinen unermüdlichen Einsatz am Ziehturm hätte ich nicht die Möglichkeit gehabt so viele meiner Ideen auch im Labor testen zu können.
- Der Fasertruppe des IFSW für die konstruktive Zusammenarbeit. Unsere Arbeiten haben sich gegenseitig befruchtet und unseren Spaß hatten wir obendrein.

- Den wissenschaftlichen Mitarbeitern am IFSW. Die interdisziplinäre Zusammensetzung hat stets neue Blickwinkel ermöglicht und außerdem gezeigt wie gut Whisky und Monty Python zusammenpassen.

- Technik, Werkstatt und Verwaltung des IFSWs. Vielen Dank für Eure vielseitige und freundschaftliche Unterstützung.

- Dem Arbeitskreis Astronomie bzw. dem Team der Sternwarte Paffenwald. Eure Freundschaft hat mich während meiner ganzen Zeit an der Universität stets gestärkt. Außerdem hatte ich dank euch die Möglichkeit mich ab und zu meiner alten Passion, der Astronomie und Astrophysik, zu widmen.

- Meinen Freunden in Stuttgart - insbesondere den "alten Stammheimern", dank Euch hatte ich immer auch ein Leben abseits der Akademia - und meinen Freunden in der ganzen Welt.

- Meinen Eltern, die auch nach über 30 Jahren nie aufgehört haben, sich voll und ganz für meine Geschwister und mich einzusetzen. Es gibt keine Möglichkeit Euch gebührenden Dank und Respekt zu erweisen aber diese meine Doktorarbeit möchte ich Euch widmen.

- Meiner Frau Siska, die mir insbesondere in der letzten Phase meiner Dissertation den Rücken frei gehalten hat und immer für mich da ist.

Laser in der Materialbearbeitung

Forschungsberichte des IFSW (Institut für Strahlwerkzeuge)

Herausgegeben von
Prof. Dr.-Ing. habil. Helmut Hügel, Universität Stuttgart
Forschungsberichte des IFSW von 1992 bis 1999 erschienen im Teubner Verlag, Stuttgart

Zoske, Uwe
Modell zur rechnerischen Simulation von Laserresonatoren und Strahlführungssystemen
1992, 186 Seiten, ISBN 3-519-06205-4

Gorriz, Michael
Adaptive Optik und Sensorik im Strahlführungssystem von Laserbearbeitungsanlagen
1992, vergriffen, ISBN 3-519-06206-2

Mohr, Ursula
Geschwindigkeitsbestimmende Strahleigenschaften und Einkoppelmechanismen beim CO_2-Laserschneiden von Metallen
1993, 130 Seiten, ISBN 3-519-06207-0

Rudlaff, Thomas
Arbeiten zur Optimierung des Umwandlungshärtens mit Laserstrahlen
1993, 152 Seiten, ISBN 3-519-06208-9

Borik, Stefan
Einfluß optischer Komponenten auf die Strahlqualität von Hochleistungslasern
1993, 200 Seiten, ISBN 3-519-06209-7

Paul, Rüdiger
Optimierung von HF-Gasentladungen für schnell längsgeströmte CO_2-Laser
1994, 149 Seiten, ISBN 3-519-06210-0

Wahl, Roland
Robotergeführtes Laserstrahlschweißen mit Steuerung der Polarisationsrichtung
1994, 150 Seiten, ISBN 3-519-06211-9

Frederking, Klaus-Dieter
Laserlöten kleiner Kupferbauteile mit geregelter Lotdrahtzufuhr
1994, 139 Seiten, ISBN 3-519-06212-7

Grünewald, Karin M.
Modellierung der Energietransferprozesse in längsgeströmten CO_2-Lasern
1994, 158 Seiten, ISBN 3-519-06213-5

Shen, Jialin
Optimierung von Verfahren der Laseroberflächenbehandlung mit gleichzeitiger Pulverzufuhr
1994, 160 Seiten, ISBN 3-519-06214-3

Arnold, Johannes M.
Abtragen metallischer und keramischer Werkstoffe mit Excimerlasern
1994, 192 Seiten, ISBN 3-519-06215-1

Holzwarth, Achim
Ausbreitung und Dämpfung von Stoßwellen in Excimerlasern
1994, 153 Seiten, ISBN 3-519-06216-X

Dausinger, Friedrich
Strahlwerkzeug Laser: Energieeinkopplung und Prozeßeffektivität
1995, 143 Seiten, ISBN 3-519-06217-8

Meiners, Eckhard
Abtragende Bearbeitung von Keramiken und Metallen mit gepulstem Nd:YAG-Laser als zweistufiger Prozeß
1995, 120 Seiten, ISBN 3-519-06222-4

Beck, Markus
Modellierung des Lasertiefschweißens
1996, 160 Seiten, ISBN 3-519-06218-6

Breining, Klaus
Auslegung und Vermessung von Gasentladungsstrecken für CO_2-Hochleistungslaser
1996, 131 Seiten, ISBN 3-519-06219-4

Griebsch, Jürgen
Grundlagenuntersuchungen zur Qualitätssicherung beim gepulsten Lasertiefschweißen
1996, 133 Seiten, ISBN 3-519-06220-8

Krepulat, Walter
Aerodynamische Fenster für industrielle Hochleistungslaser
1996, 144 Seiten, ISBN 3-519-06221-6

Xiao, Min
Vergleichende Untersuchungen zum Schneiden dünner Bleche mit CO_2- und Nd:YAG-Lasern
1996, 118 Seiten, ISBN 3-519-06223-2

Glumann, Christiane
Verbesserte Prozeßsicherheit und Qualität durch Strahlkombination beim Laserschweißen
1996, 143 Seiten, ISBN 3-519-06224-0

Gross, Herbert
Propagation höhermodiger Laserstrahlung und deren Wechselwirkung mit optischen Systemen
1996, 191 Seiten, ISBN 3-519-06225-9

Rapp, Jürgen
Laserschweißeignung von Aluminiumwerkstoffen für Anwendungen im Leichtbau
1996, 202 Seiten, ISBN 3-519-06226-7

Wittig, Klaus
Theoretische Methoden und experimentelle Verfahren zur Charakterisierung von Hochleistungslaserstrahlung
1996, 198 Seiten, ISBN 3-519-06227-5

Grünenwald, Bernd
Verfahrensoptimierung und Schichtcharakterisierung beim einstufigen Cermet-Beschichten mittels CO_2-Hochleistungslaser
1996, 160 Seiten, ISBN 3-519-06229-1

Lee, Jae-Hoon
Laserverfahren zur strukturierten Metallisierung
1996, 154 Seiten, ISBN 3-519-06232-1

Albinus, Uwe N. W.
Metallisches Beschichten mittels PLD-Verfahren
1996, 144 Seiten, ISBN 3-519-06233-X

Wiedmaier, Matthias
Konstruktive und verfahrenstechnische Entwicklungen zur Komplettbearbeitung in Drehzentren mit integrierten Laserverfahren
1997, 129 Seiten, ISBN 3-519-06228-3

Bloehs, Wolfgang
Laserstrahlhärten mit angepaßten Strahlformungssystemen
1997, 143 Seiten, ISBN 3-519-06230-5

Bea, Martin
Adaptive Optik für die Materialbearbeitung mit CO_2-Laserstrahlung
1997, 143 Seiten, ISBN 3-519-06231-3

Stöhr, Michael
Beeinflussung der Lichtemission bei mikrokanalgekühlten Laserdioden
1997, 147 Seiten, ISBN 3-519-06234-8

Plaß, Wilfried
Zerstörschwellen und Degradation von CO_2-Laseroptiken
1998, 158 Seiten, ISBN 3-519-06235-6

Schaller, Markus K. R.
Lasergestützte Abscheidung dünner Edelmetallschichten zum Heißgaskorrosionsschutz für Molybdän
1998, 163 Seiten, ISBN 3-519-06236-4

Hack, Rüdiger
System- und verfahrentechnischer Vergleich von Nd:YAG- und CO_2-Lasern im Leistungsbereich bis 5 kW
1998, 165 Seiten, ISBN 3-519-06237-2

Krupka, René
Photothermische Charakterisierung optischer Komponenten für Hochleistungslaser
1998, 139 Seiten, ISBN 3-519-06238-0

Pfeiffer, Wolfgang
Fluiddynamische und elektrophysikalisch optimierte Entladungsstrecken für CO_2-Hochleistungslaser
1998, 152 Seiten, ISBN 3-519-06239-9

Volz, Robert
Optimiertes Beschichten von Gußeisen-, Aluminium- und Kupfergrundwerkstoffen mit Lasern
1998, 133 Seiten, ISBN 3-519-06240-2

Bartelt-Berger, Lars
Lasersystem aus kohärent gekoppelten Grundmode-Diodenlasern
1999, 135 Seiten, ISBN 3-519-06241-0

Müller-Hummel, Peter
Entwicklung einer Inprozeßtemperaturmeßvorrichtung zur Optimierung der laserunterstützten Zerspanung
1999, 139 Seiten, ISBN 3-519-06242-9

Rohde, Hansjörg
Qualitätsbestimmende Prozeßparameter beim Einzelpulsbohren mit einem Nd:YAG-Slablaser
1999, 171 Seiten, ISBN 3-519-06243-7

Huonker, Martin
Strahlführung in CO_2-Hochleistungslasersystemen zur Materialbearbeitung
1999, 121 Seiten, ISBN 3-519-06244-5

Callies, Gert
Modellierung von qualitäts- und effektivitätsbestimmenden Mechanismen beim Laserabtragen
1999, 119 Seiten, ISBN 3-519-06245-3

Schubert, Michael E.
Leistungsskalierbares Lasersystem aus fasergekoppelten Singlemode-Diodenlasern
1999, 105 Seiten, ISBN 3-519-06246-1

Kern, Markus
Gas- und magnetofluiddynamische Maßnahmen zur Beeinflussung der Nahtqualität beim Laserstrahlschweißen
1999, 132 Seiten, ISBN 3-519-06247-X

Raiber, Armin
Grundlagen und Prozeßtechnik für das Lasermikrobohren technischer Keramiken
1999, 135 Seiten, ISBN 3-519-06248-8

Laser in der Materialbearbeitung

Forschungsberichte des IFSW (Institut für Strahlwerkzeuge)

Herausgegeben von
Prof. Dr.-Ing. habil. Helmut Hügel, Universität Stuttgart
Forschungsberichte des IFSW ab 2000 erschienen im Herbert Utz Verlag, München

Schittenhelm, Henrik
Diagnostik des laserinduzierten Plasmas beim Abtragen und Schweißen
2000, 141 Seiten, ISBN 3-89675-712-1

Stewen, Christian
Scheibenlaser mit Kilowatt-Dauerstrichleistung
2000, 145 Seiten, ISBN 3-89675-763-6

Schmitz, Christian
Gaselektronische Analysemethoden zur Optimierung von Lasergasentladungen
2000, 107 Seiten, ISBN 3-89675-773-3

Karszewski, Martin
Scheibenlaser höchster Strahlqualität
2000, 132 Seiten, ISBN 3-89675-785-7

Chang, Chin-Lung
Berechnung der Schmelzbadgeometrie beim Laserstrahlschweißen mit Mehrfokustechnik
2000, 141 Seiten, ISBN 3-89675-825-X

Haag, Matthias
Systemtechnische Optimierungen der Strahlqualität von Hochleistungsdiodenlasern
2000, 166 Seiten, ISBN 3-89675-840-3

Bahnmüller, Jochen
Charakterisierung gepulster Laserstrahlung zur Qualitätssteigerung beim Laserbohren
2000, 138 Seiten, ISBN 3-89675-851-9

Schellhorn, Martin Carl Johannes
CO-Hochleistungslaser: Charakteristika und Einsatzmöglichkeiten beim Schweißen
2000, 142 Seiten, ISBN 3-89675-849-7

Angstenberger, Birgit
Fliehkraftunterstütztes Laserbeschichten
2000, 153 Seiten, ISBN 3-89675-861-6

Bachhofer, Andreas
Schneiden und Schweißen von Aluminiumwerkstoffen mit Festkörperlasern für den Karosseriebau
2001, 194 Seiten, ISBN 3-89675-881-0

Breitschwerdt, Sven
Qualitätssicherung beim Laserstrahlschweißen
2001, 150 Seiten, ISBN 3-8316-0032-5

Mochmann, Gunter
Laserkristallisation von Siliziumschichten auf Glas- und Kunststoffsubstraten für die Herstellung verbesserter Dünnschichttransistoren
2001, 170 Seiten, ISBN 3-89675-811-X

Herrmann, Andreas
Fertigungsorientierte Verfahrensentwicklung des Weichlötens mit Diodenlasern
2002, 133 Seiten, ISBN 3-8316-0086-4

Mästle, Rüdiger
Bestimmung der Propagationseigenschaften von Laserstrahlung
2002, 147 Seiten, ISBN 3-8316-0113-5

Voß, Andreas
Der Scheibenlaser: Theoretische Grundlagen des Dauerstrichbetriebs und erste experimentelle Ergebnisse anhand von Yb:YAG
2002, 195 Seiten, ISBN 3-8316-0121-6

Müller, Matthias G.
Prozessüberwachung beim Laserstrahlschweißen durch Auswertung der reflektierten Leistung
2002, 122 Seiten, ISBN 3-8316-0144-5

Abeln, Tobias
Grundlagen und Verfahrenstechnik des reaktiven Laserpräzisionsabtragens von Stahl
2002, 138 Seiten, ISBN 3-8316-0137-2

Erhard, Steffen
Pumpoptiken und Resonatoren für den Scheibenlaser
2002, 184 Seiten, ISBN 3-8316-0173-9

Contag, Karsten
Modellierung und numerische Auslegung des Yb:YAG-Scheibenlasers
2002, 155 Seiten, ISBN 3-8316-0172-0

Krastel, Klaus
Konzepte und Konstruktionen zur laserintegrierten Komplettbearbeitung in Werkzeugmaschinen
2002, 140 Seiten, ISBN 3-8316-0176-3

Staud, Jürgen
Sensitive Werkzeuge für ein neues Montagekonzept in der Mikrosystemtechnik
2002, 122 Seiten, ISBN 3-8316-0175-5

Schinzel, Cornelius M.
Nd:YAG-Laserstrahlschweißen von Aluminiumwerkstoffen für Anwendungen im Automobilbau
2002, 177 Seiten, ISBN 3-8316-0201-8

Sebastian, Michael
Grundlagenuntersuchungen zur Laser-Plasma-CVD Synthese von Diamant und amorphen Kohlenstoffen
2002, 153 Seiten, ISBN 3-8316-0200-X

Lücke, Bernd
Kohärente Kopplung von Vertikalemitter-Arrays
2003, 120 Seiten, ISBN 3-8316-0224-7

Hohenberger, Bernd
Laserstrahlschweißen mit Nd:YAG-Doppelfokustechnik – Steigerung von Prozeßsicherheit, Flexibilität und verfügbarer Strahlleistung
2003, 128 Seiten, ISBN 3-8316-0223-9

Jasper, Knut
Neue Konzepte der Laserstrahlformung und -führung für die Mikrotechnik
2003, 152 Seiten, ISBN 3-8316-0205-0

Heimerdinger, Christoph
Laserstrahlschweißen von Aluminiumlegierungen für die Luftfahrt
2003, 112 Seiten, ISBN 3-8316-0256-5

Christoph Fleig
Evaluierung eines Messverfahrens zur genauen Bestimmung des Reflexionsgrades optischer Komponenten
2003, 150 Seiten, ISBN 3-8316-0274-3

Joachim Radtke
Herstellung von Präzisionsdurchbrüchen in keramischen Werkstoffen mittels repetierender Laserbearbeitung
2003, 150 Seiten, ISBN 3-8316-0285-9

Michael Brandner
Steigerung der Prozesseffizienz beim Löten und Kleben mit Hochleistungsdiodenlasern
2003, 195 Seiten, ISBN 3-8316-0288-3

Reinhard Winkler
Porenbildung beim Laserstrahlschweissen von Aluminium-Druckguss
2004, 153 Seiten, ISBN 3-8316-0313-8

Helmut Kindler
Optische und gerätetechnische Entwicklungen zum Laserstrahlspritzen
2004, 117 Seiten, ISBN 3-8316-0315-4

Andreas Ruf
Modellierung des Perkussionsbohrens von Metallen mit kurz- und ultrakurzgepulsten Lasern
2004, 140 Seiten, ISBN 3-8316-0372-3

Guido Hergenhan
Kohärente Kopplung von Vertikalemittern – Systemkonzept und experimentelle Verifizierung
2004, 115 Seiten, ISBN 3-8316-0376-6

Klaus Goth
Schweißen von Mischverbindungen aus Aluminiumguß- und Knetlegierungen mit CO_2-Laser unter besonderer Berücksichtigung der Nahtart
2004, 143 Seiten, ISBN 3-8316-0427-4

Armin Strauch
Effiziente Lösung des inversen Problems beim Laserstrahlschweißen durch Simulation und Experiment
2004, 169 Seiten, ISBN 3-8316-0425-8

Thomas Wawra
Verfahrensstrategien für Bohrungen hoher Präzision mittels Laserstrahlung
2004, 162 Seiten, ISBN 3-8316-0453-3

Michael Honer
Prozesssicherungsmaßnahmen beim Bohren metallischer Werkstoffe mittels Laserstrahlung
2004, 113 Seiten, ISBN 3-8316-0441-x

Thomas Herzinger
Prozessüberwachung beim Laserbohren von Turbinenschaufeln
2004, 143 Seiten, ISBN 3-8316-0443-6

Reiner Heigl
Herstellung von Randschichten auf Aluminiumgusslegierungen mittels Laserstrahlung
2004, 173 Seiten, ISBN 3-8316-0460-6

Laser in der Materialbearbeitung

Forschungsberichte des IFSW (Institut für Strahlwerkzeuge)

Herausgegeben von
Prof. Dr. phil. nat. habil. Thomas Graf, Universität Stuttgart
Forschungsberichte des IFSW ab 2005 erschienen im Herbert Utz Verlag, München

Thomas Fuhrich
Marangoni-effekt beim Laserstrahltiefschweißen von Stahl
2005, 163 Seiten, ISBN 3-8316-0493-2

Daniel Müller
Pulsenergiestabilität bei regenerativen Kurzpulsverstärkern im Scheibenlaserdesign
2005, 172 Seiten, ISBN 3-8316-0508-4

Jiancun Gao
Neodym-dotierte Quasi-Drei-Niveau-Scheibenlaser: Hohe Ausgangsleistung und Frequenzverdopplung
2005, 148 Seiten, ISBN 3-8316-0521-1

Wolfgang Gref
Laserstrahlschweißen von Aluminiumwerkstoffen mit der Fokusmatrixtechnik
2005, 136 Seiten, ISBN 3-8316-0537-8

Michael Weikert
Oberflächenstrukturieren mit ultrakurzen Laserpulsen
2005, 116 Seiten, ISBN 3-8316-0573-4

Julian Sigel
Lasergenerieren metallischer Bauteile mit variablem Laserstrahldurchmesser in modularen Fertigungssystemen
2006, 132 Seiten, ISBN 3-8316-0572-6

Andreas Ruß
Schweißen mit dem Scheibenlaser-Potentiale der guten Fokussierbarkeit
2006, 142 Seiten, ISBN 3-8316-0580-7

Gabriele Seibold
Absorption technischer Oberflächen in der Lasermaterialbearbeitung
2006, 156 Seiten, ISBN 3-8316-0618-8

Dirk Lindenau
Magnetisch beeinflusstes Laserstrahlschweißen
2007, 180 Seiten, ISBN 978-3-8316-0687-0

Jens Walter
Gesetzmäßigkeiten beim Lasergenerieren als Basis für die Prozesssteuerung und –regelung
2008, 140 Seiten, ISBN 978-3-8316-0770-9

Heiko Ridderbusch
Longitudinal angeregte passiv gütegeschaltete Laserzündkerze
2008, 175 Seiten, ISBN 978-3-8316-0840-9

Markus Leimser
Strömungsinduzierte Einflüsse auf die Nahteigenschaften beim Laserstrahlschweißen von Aluminiumwerkstoffen
2009, 150 Seiten, ISBN 978-3-8316-0854-6

Mikhail Larionov
Kontaktierung und Charakterisierung von Kristallen für Scheibenlaser
2009, 186 Seiten, ISBN 978-3-8316-0855-3

Jürgen Müller-Borhanian
Kamerabasierte In-Prozessüberwachung beim Laserstrahlschweißen
2009, 162 Seiten, ISBN 978-3-8316-0890-4

Andreas Letsch
Charakterisierung allgemein astigmatischer Laserstrahlung mit der Methode der zweiten Momente
2009, 176 Seiten, ISBN 978-3-8316-0896-6

Thomas Kübler
Modellierung und Simulation des Halbleiterscheibenlasers
2009, 152 Seiten, ISBN 978-3-8316-0918-5

Günter Ambrosy
Nutzung elektromagnetischer Volumenkräfte beim Laserstrahlschweißen
2009, 170 Seiten, ISBN 978-3-8316-0925-3

Agnes Ott
Oberflächenmodifikation von Aluminiumlegierungen mit Laserstrahlung: Prozessverständnis und Schichtcharakterisierung
2010, 226 Seiten, ISBN 978-3-8316-0959-8

Detlef Breitling
Gasphaseneinflüsse beim Abtragen und Bohren mit ultrakurz gepulster Laserstrahlung
2010, 200 Seiten, ISBN 978-3-8316-0960-4

Dmitrij Walter
Online-Qualitätssicherung beim Bohren mittels ultrakurz gepulster Laserstrahlung
2010, 156 Seiten, ISBN 978-3-8316-0968-0

Jan-Philipp Weberpals
Nutzen und Grenzen guter Fokussierbarkeit beim Laserstrahlschweißen
2010, 154 Seiten, ISBN 978-3-8316-0995-6

Angelika Beyertt
Yb:KYW regenerativer Verstärker für ultrakurze Pulse
2010, 166 Seiten, ISBN 978-3-8316-4002-7

Christian Stolzenburg
Hochrepetierende Kurzpuls-Scheibenlaser im infraroten und grünen Spektralbereich
2011, 184 Seiten, ISBN 978-3-8316-4041-6

Svent-Simon Beyertt
Quantenfilm-Pumpen zur Leistungsskalierung von Halbleiter-Scheibenlasern
2011, 130 Seiten, ISBN 978-3-8316-4051-5

Sonja Kittel
Verzugsarmes Laserstrahlschweißen an axialsymmetrischen Bauteilen
2011, 162 Seiten, ISBN 978-3-8316-4088-1

Andrey Andreev
Schweißen mit dem Scheibenlaser im Getriebebau – Prozessmerkmale und Anlagenkonzepte
2011, 140 Seiten, ISBN 978-3-8316-4103-1

Christian Föhl
Einsatz ultrakurz gepulster Laserstrahlung zum Präzisionsbohren von Metallen
2011, 156 Seiten, ISBN 978-3-8316-4120-8

Andreas Josef Birnesser
Prozessregelung beim Laserstrahlschweißen
2011, 150 Seiten, ISBN 978-3-8316-4133-8

Christoph Neugebauer
Thermisch aktive optische Bauelemente für den resonatorinternen Einsatz beim Scheibenlaser
2012, 220 Seiten, ISBN 978-3-8316-4178-9

Andreas Dauner
Fluidmechanische Maßnahmen zur Reduzierung von Schmelzablagerungen beim Hochgeschwindigkeitslaserbohren
2012, 150 Seiten, ISBN 978-3-8316-4194-9

Axel Heß
Vorteile und Herausforderungen beim Laserstrahlschweißen mit Strahlquellen höchster Fokussierbarkeit
2012, 164 Seiten, ISBN 978-3-8316-4198-7

Christian Gehrke
Überwachung der Struktureigenschaften beim Oberflächenstrukturieren mit ultrakurzen Laserpulsen
2013, 164 Seiten, ISBN 978-3-8316-4271-7

David Schindhelm
In-Prozess Qualitätssicherung für das Laserstrahlschneiden von Metallen
2013, 164 Seiten, ISBN 978-3-8316-4345-5

Moritz Vogel
Speciality Fibers for High Brightness Laser Beam Delivery
2014, 200 Seiten, ISBN 978-3-8316-4382-0